UNIVERSIDAD POLITÉCNICA DE MADRID
Escuela Técnica Superior de Ingeniería Aeronaútica y del Espacio

Ascent phase thermal study of stratospheric balloon-borne payloads

DOCTORAL THESIS

Submitted for the degree of Doctor by:

Alejandro José Fernández Soler
Máster Universitario en Sistemas Espaciales

Madrid, 2024


UNIVERSIDAD POLITÉCNICA DE MADRID
Escuela Técnica Superior de Ingeniería Aeronaútica y del Espacio

Doctoral Degree in Doctorado en Ingeniería Aeroespacial

Ascent phase thermal study of stratospheric balloon-borne payloads

DOCTORAL THESIS

Submitted for the degree of Doctor by:

Alejandro José Fernández Soler
Máster Universitario en Sistemas Espaciales

Under the supervision of:
Dr. Isabel Pérez Grande

Madrid, 2024

Title: Ascent phase thermal study of stratospheric balloon-borne payloads

Author: Alejandro José Fernández Soler

Doctoral Programme: Doctorado en Ingeniería Aeroespacial

Thesis Supervision:

Dra. Isabel Pérez Grande, Doctora en Ingeniería Aeronáutica, Universidad Politécnica de Madrid (Supervisor)

External Reviewers:

Thesis Defense Committee:

Thesis Defense Date:

Agradecimientos

En primer lugar, agradecer a mis padres y a mi hermana todo el buen trabajo que han hecho conmigo, por apoyarme en mis decisiones, porque sin duda sin ellos no podría haber llegado tan lejos.

Ángela, muchas gracias por ser tan compresiva con mis agobios, por entenderme, por apoyarme en los malos momentos, especialmente al final de este camino.

Mis compañeros del IDR, por esos ratos de café tan necesarios. En especial a David por el trabajo mano a mano durante estos años, a Juan, por esas charlas tan productivas, y a María José por tu gran ayuda con la siempre complicada burocracia.

Ángel, muchas gracias por tus ideas, tus comentarios, y sobre todo, por tu disponibilidad, siempre con la puerta abierta para nosotros.

Por último y no menos importante, al IDR, en especial a Isabel, por darme la oportunidad de empezar en este mundo tan fascinante del sector espacial y ayudarme a crecer como profesional.

Abstract

Stratospheric balloons are highly relevant platforms for space missions to achieve scientific objectives. These platforms are becoming increasingly important because they can place payloads at an altitude above almost 99 % of the atmosphere, where the environmental conditions are very similar to those in space, at much lower cost than traditional spacecraft.

From a thermal point of view, due to the combination of relative wind speed and the harsh thermal environment, during the ascent phase of this type of mission, the on-board equipment can reach the lowest temperatures of the entire mission, Therefore, thermal analyses of the ascent phase are essential and their results significantly contribute to the thermal design.

Thermal modelling and analysis of stratospheric balloon instruments usually involves the development of a Geometric Mathematical Model (GMM) and a Thermal Mathematical Model (TMM) using space-specific software such as ESATAN-TMS or THERMICA, based on the Lumped Parameter Method. However, it is not easy to implement convection in this type of software, as experimental correlations from different authors are often used (which can lead to misuse of these correlations, as there may be Rayleigh ranges in which no correlation is valid, or a discontinuity may occur if the correlation used is changed. Furthermore, not all correlations are based on the same definition of dimensionless numbers, which can also lead to misuse). Firstly, it is necessary to quantify both the forced convection on the outer surfaces based on the relative air speed and the air properties at all times during the flight. Secondly, it is necessary to apply free convection heat transfer to the internal surfaces in a parametric way to account for changing environmental conditions. Therefore, a detailed study of the ambient thermal conditions must be carried out to obtain the worst conditions, as needed for the thermal design.

Hence, the work developed in this Doctoral Dissertation is divided into two main parts. In the first part, a new methodology based on local databases to define the thermal environment is proposed. The parameters of the thermal environment have been studied to determine the worst-case thermal environment from a thermal point of view, not only the radiative parameters and the

air temperature, but also the influence of each parameter on the ascent rate and the horizontal relative wind speed, and their subsequent effect on the temperature of the instruments on board the stratospheric balloon. For this study, an aerodynamic model, where all the thermal environment parameters that govern the thermal interactions are based on local databases, was developed to simulate the ascent phase of the balloon. As an example, the study has been applied to the BEXUS programme launches, which take place in a yearly basis (from September to October) from the European Space Center at Esrange (Sweden). An envelope of maximum and minimum ascent rate profiles was obtained and compared with flight data from eight BEXUS mission flights, with a good agreement. Then, the simulations of the thermal behaviour of a single payload based on the worst-case thermal environment results, have shown a maximum difference temperature (of the payload) of more than 10 °C, depending on the choice of the worst thermal case, demonstrating its relevance.

In the second part, the accuracy of the empirical correlations available for modelling convection have proved to be limited (as above commented), as there is no consistency in the literature for the Rayleigh range expected during the flight. To reduce the uncertainty associated with this fact, environmental chamber tests have been performed to obtain new convective correlations that can be applied throughout the balloon mission.

Finally, the proposed methodology has been applied together with the new correlation on real missions such as TASEC-LAB and SUNRISE III, showing a good agreement between flight data and simulations.

Resumen

Los globos estratosféricos son plataformas con una gran relevancia en misiones espaciales para conseguir objetivos científicos. Estas plataformas están adquiriendo cada vez más importancia por su capacidad para situar cargas útiles a una altitud superior a casi el 99 % de la atmósfera (en términos de densidad), donde las condiciones ambientales son muy similares a las espaciales, con unos costes muy inferiores en comparación con los satélites tradicionales.

Desde el punto de vista térmico, debido a la combinación de la velocidad relativa al viento y el entorno térmico adverso, durante la fase de ascenso de este tipo de misiones, los equipos a bordo pueden alcanzar las temperaturas mínimas de toda la misión. Por tanto, el análisis térmico de la fase de ascenso se hace fundamental y sus resultados contribuyen significativamente al diseño térmico.

La modelización y el análisis térmico de los instrumentos a bordo de los globos estratosféricos suele implicar la creación de un Modelo Matemático Geométrico (GMM) y un Modelo Matemático Térmico (TMM), utilizando programas específicos del sector espacial como ESATAN-TMS o THERMICA, basados en el método de elementos concentrados. Sin embargo, la implementación de la convección en este tipo de programas es muy compleja ya que se suelen emplear correlaciones experimentales de diferentes autores (lo que puede provocar errores en el uso de estas correlaciones, puesto que pueden existir rangos de Rayleigh en los que ninguna correlación sea válida, o que al cambiar la correlación usada aparezca una discontinuidad. Además, no todas las correlaciones están basadas en la misma definición para los números adimensionales, por lo que, de nuevo, puede dar lugar a un mal uso de ellas). Por un lado, es necesario cuantificar la convección forzada en las superficies externas, basándose en la velocidad relativa del aire y en las propiedades del aire en todo momento durante el vuelo. Por otro lado, es necesario aplicar la transferencia de calor por convección libre en las superficies internas de forma paramétrica, para tener en cuenta los cambios de las condiciones ambientales. Por lo tanto, debe realizarse un estudio en profundidad de las condiciones térmicas ambientales para obtener las condiciones más desfavorables.

El trabajo desarrollado en esta Tesis Doctoral se divide en dos partes principales. En primer lugar, se propone una nueva metodología basada en bases de datos locales para definir el entorno térmico. Se han estudiado los parámetros del entorno térmico, para definir el peor caso de diseño desde el punto de visto térmico, no sólo los parámetros radiativos y la temperatura del aire sino también la influencia de cada parámetro en la velocidad de ascenso y la velocidad relativa horizontal del viento, así como su posterior impacto en la temperatura de los instrumentos a bordo del globo estratosférico. Para este estudio, se ha desarrollado un modelo aerodinámico para simular la fase de ascenso del globo, en el que todos los parámetros del entorno térmico que gobiernan las interacciones térmicas se han obtenido de bases de datos locales. A modo de ejemplo, se ha particularizado el estudio para los lanzamientos del programa BEXUS, que se efectúan cada año entre los meses de septiembre y octubre desde Esrange (Suecia). Se ha obtenido una envolvente de perfiles de velocidad de ascenso máxima y mínima, que se ha comparado con los datos de vuelo de ocho misiones BEXUS, obteniéndose una buena concordancia. Las simulaciones del comportamiento térmico de una carga de pago simple han mostrado una diferencia de temperatura superior a 10 °C dependiendo de la selección del peor caso térmico, demostrando su impacto.

En segundo lugar, las correlaciones empíricas disponibles en la literatura para modelar la convección han resultado limitantes ya que, para el rango de Rayleigh esperado durante el vuelo, no existe una consistencia entre dichas correlaciones. Para reducir la incertidumbre asociada a este hecho, se han realizado ensayos en cámara ambiental para obtener una nueva correlación convectiva que pueda aplicarse a lo largo de la misión del globo.

Finalmente, se ha aplicado la metodología propuesta junto con la nueva correlación en misiones reales como TASEC-LAB y SUNRISE III, mostrando una buena concordancia entre los datos de vuelo y las simulaciones.

Contents

List of Figures

List of Tables

Nomenclature

A	Balloon top area [m^2]
A	Heat transfer surface area [m^2]
A_B	Surface area showing [m^2]
$A_{B'}$	Balloon effective area [m^2]
$A_{B,C}$	Balloon convective effective area [m^2]
A_{PL}	Plate area [m^2]
A_p	Illuminated projected area [m^2]
$B_{i,j}$	Gebhart factor [-]
C	Heat capacity [$J \cdot K^{-1}$]
C_D	Drag coefficient [-]
D	Drag force vector [N]
E_b	Energy radiated per unit area [$W \cdot m^{-2}$]
F_{BE}	View factor between the Earth and the balloon [-]
F_L	Free lift [-]
G_L	Linear coupling [$W \cdot K^{-1}$]
G_R	Radiative conductor [m^2]
G_S	Solar constant [$W \cdot m^{-2}$]

G_s^{TOA} Solar irradiance at the top of the atmosphere [W · m^{-2}]

G_s Solar irradiance [W · m^{-2}]

I Buoyancy force vector [N]

L_G^F Gore length at float conditions [m]

L_G Gore length [m]

M$_a$ Air molecular mass [kg · mol^{-1}]]

M$_g$ Lifting gas molecular mass [kg · mol^{-1}]]

$\dot{Q}$ Heat flow [W]

$\dot{Q}_B^{IR}$ IR sky heat flow [W]

$\dot{Q}_{out}^{IR}$ IR emitted heat flow[W]

$\dot{Q}_{C,ext}$ External convective heat flow from the film balloon to the air [W]

$\dot{Q}_{C,in}$ Internal convective heat flow from the lifting gas to the balloon film [W]

$\dot{Q}_E$ IR Earth heat flow [W]

$\dot{Q}_S$ Direct solar heat flow [W]

$\dot{Q}_{albedo}$ Albedo heat flow [W]

$\dot{Q}_p$ IR planetary thermal infrared heat flow [W]

$\dot{Q}_{sky}$ IR sky heat flow [W]

R_a Air specific air constant [J · kg^{-1} · K^{-1}]

R_g Lifting gas specific constant [J · kg^{-1} · K^{-1}]

$R_{i,j}$ Radiative exchange constant from node i to node j [W · K^{-4}]

T Temperature [K]

T_B Balloon film temperature [K]

T_E IR Earth equivalent temperature [K]

T_∞ Temperature of the unperturbated fluid [K]

T_{amb} Ambient temperature [K]

T_a Air temperature [K]

T_g Lifting gas temperature [K]

T_{sky} Sky temperature [K]

T_s Surface temperature [K]

ΔT Temperature gradient [K]

Δx Length of path flow [m]

V Balloon volume [m^3]

V_F Balloon voflume at float conditions [m^3]

$\mathbf{W}$ System weight vector [N]

a Albedo coefficient [-]

c_p Specific thermal capacity [$J \cdot kg^{-1} \cdot K^{-1}$]

c_v Specific heat at constant volume [$J \cdot kg^{-1} \cdot K^{-1}$]

d Balloon diameter [m]

$\mathbf{g}$ Gravity acceleration vector [$m \cdot s^{-2}$]

h Convective heat transfer coefficient [$W \cdot m^{-2} \cdot K^{-1}$]

k Thermal conductivity [$W \cdot m^{-1} \cdot K^{-1}$]

$\dot{m}$ Mass flow rate [$kg \cdot s^{-1}$]

m_B Balloon film mass [kg]

m_G Gross mass [kg]

m_{add} Additional mass [kg]

m_b Ballast mass [kg]

m_g Lifting gas mass [kg]

m_p Payload mass [kg]

m_t System mass [kg]

p Pressure [Pa]

$\dot{q}_E$ IR Earth heat flux (OLR) [W · m^{-2}]

$\dot{q}_{albedo}$ Albedo heat flux [W · m^{-2}]

$\dot{q}_{sky}$ IR sky heat flux [W · m^{-2}]

$\mathbf{r}$ Balloon borne position vector [m]

u_0 Upstream fluid velocity [m · s^{-1}]

u_∞ Unperturbated fluid velocity [m · s^{-1}]

$\mathbf{v}$ Balloon relative velocity to the wind speed vector [m · s^{-1}]

$\mathbf{v}_w$ Wind speed vector [m · s^{-1}]

v Balloon relative velocity to the wind speed [m · s^{-1}]

v_z Ascent rate [m · s^{-1}]

Ω Local Hour Angle [rad]

α Solar absorptivity [-]

α_D Thermal diffusivity [m^2/s]

β Volume expansion coefficient [K^{-1}]

γ' Air lapse rate [K · km^{-1}]

γ Adiabatic coefficient [-]

δ Solar declination [rad]

δ_T Thickness of the temperature boundary layer [m]

δ_v Thickness of the velocity boundary layer [m]

ε IR emissivity [-]

θ Solar Zenith Angle (SZA) [rad]

θ_s Angle between the normal to the surface and the solar rays [rad]

$\bar{\lambda_x}$	Parameter global influence coefficient [-]
λ	Latitude [deg]
λ_c	Molecular mean free path [m]
λ_w	Wavelength [m]
λ_x	Parameter influence coefficient [$m \cdot s^{-1}$]
μ	Dynamic viscosity [$kg \cdot s^{-1} \cdot m$]
ν	Kinematic viscosity [m^2/s]
ρ'_{IR}	IR reflectivity [-]
ρ'_S	Solar reflectivity [-]
ρ_a	Air density [$kg \cdot m^{-3}$]
ρ_g	Lifting gas density [$kg \cdot m^{-3}$]
τ_{IR}	IR transmissivity [-]
τ_S	Solar transmissivity [-]
ϕ	Longitude [deg]
Fr	Froude Number [-]
Gr	Grashof Number [-]
Kn	Knudsen Number [-]
Nu	Nusselt Number [-]
Pr	Prandtl Number [-]
Re	Reynolds Number [-]
SZA	Solar Zenith Angle [rad]
LHA	Local Hour Angle [rad]
OLR	Outgoing Longwave Radiation [$W \cdot m^{-2}$]

List of Acronyms

APL Johns Hopkins Applied Physics Laboratory.

BEXUS Balloon Experiments for University Students.

BP Baseplate.

CAD Computer-Aided Design.

CERES Clouds and Earth Radiant Energy System.

CFD Computational Fluid Dynamics.

COC Cold Operational Case.

COTS Commercial Off-The-Shelf.

DLR German Space Agency.

ECMWF European Centre for Medium-Range Weather Forecasts.

ECSS European Cooperation for Space Standardization.

EPS Electrical Power Subsystem.

GACE Grupo de Astronomía y Ciencias del Espacio.

GMM Geometrical Mathematical Model.

GPS Global Positioning System.

HAPS High Altitude Pseudo-Satellites.

HERCCULES Heat-transfer and Environment Radiative and Convective Characterization in a University Laboratory for Experimentation in the Stratosphere.

HOC Hot Operational Case.

HTL Heat Transfer Lab.

IAC Instituto de Astrofísica de Andalucía.

IDR Instituto Universitario de Microgravedad "Ignacio Da Riva".

IMU Inertial Measurement Unit.

INTA Instituto Nacional de Técnica Aerospacial.

IR Infrared.

ISA International Standard Atmosphere.

ISO International Organization for Standardization.

KIS Kiepenheuer-Institut für Sonnenphysik.

LDB Long Duration Balloon.

LOC Launch Operational Case.

LPM Lumped Parameters Method.

LT Local Time.

MORABA Mobile Rocket Base.

MPS Max-Planck-Institut für Sonnensystemforschung.

NAOJ National Astronomical Observatory of Japan.

NASA National Aeronautics and Space Administration.

NED North-East-Down.

NOAA National Oceanic and Atmospheric Administration.

OBC On-board Computer.

OLR Outgoing Longwave Radiation.

REXUS Rocket Experiments for University Students.

RMSE Root Mean Square Error.

SHR Shroud.

SSC Swedish Space Corporation.

SZA Solar Zenith Angle.

TASEC-LAB Thermal Analysis Support and Environment Characterization Laboratory.

TMM Thermal Mathematical Model.

TVT Thermal Vacuum Test.

UV Ultraviolet.

Chapter 1. Introduction

The use of stratospheric balloons as a platform for scientific observations dates back to practically the first balloon flight in 1783 [1]. The Montgolfier brothers successfully tested a hot air balloon in France, reaching an altitude of approximately 2 km [2]. Since then, balloons have been frequently used for scientific research and remains a valuable tool for observations. In 1804, twenty-one years after the inaugural balloon flight, J.L. Gay-Lussac and Biot [3] ascended to an altitude of 4 km in a hot air balloon to measure the Earth's magnetic field at high altitudes. Gay-Lussac repeated the flight later that year, reaching an altitude of 7 km, where he studied the variation in air pressure and temperature with the altitude, and repeated his earlier electromagnetic observations. Ballooning for scientific purposes became more widespread as flight technology advanced. In 1892, Hermite and Besançon launched the first unmanned meteorological research balloons [4], marking a significant milestone, as their dedicated efforts led to the discovery of the stratosphere in 1899.

In 1912, V. F Hess ascended to 5 km, measuring the varying levels of cosmic rays at different altitudes. This research earned Hess the Nobel Prize in 1936 [5]. However, it was not until the 1930s when that balloon flights became even more significant for scientific research due to the development of low-density polyethylene film, enabling balloons to ascend to altitudes of over 30 km or higher. The progression in electronics, which enabled communication over long distances, led to the potential for unmanned, long-duration balloon flights capable of carrying heavier payloads. It was during the 1950s-1960s, when the greatest number of stratospheric balloon launches took place. For instance, in the 1950s, Stratoscope I [6], a solar telescope with a diameter of 30 cm, was launched and was able to capture images of the solar surface without any atmospheric disturbances. In the 1960s, the launch of Stratoscope II [7] (with a 90-cm diameter aperture and a gross mass of 3.6 tons), served as a the basis for design of the Hubble [8]. Then, the race for outer space provokes the ballooning programs to lose relevance, as it is shown in Figure 1.1, where the number of registered stratospheric balloons along the years are presented. It is quite clear the decreasing trend until the 2000s. In recent years, there has been a push to use scientific balloons

specially due to the possibility to use them for studying other atmosphere planets, such as Mars [9].

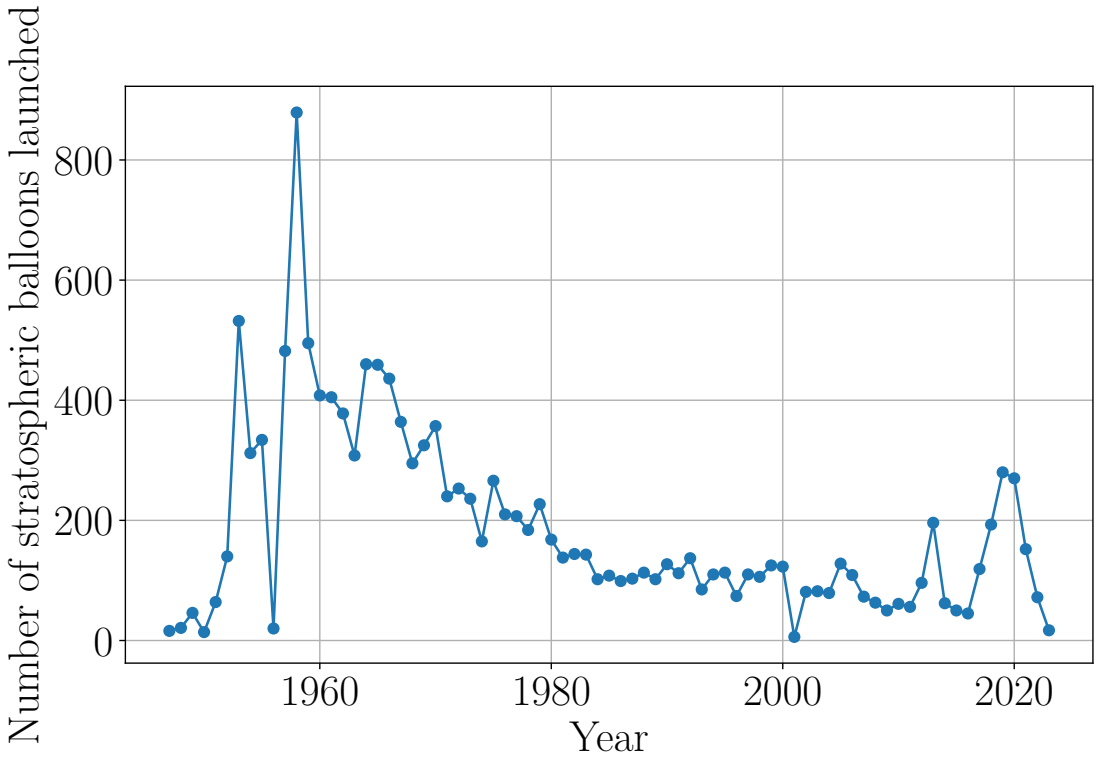

Figure 1.1: Number of registered Stratospheric launches (data obtained from [10]).

1.1 Objectives

On Earth, balloon missions usually consist of six stages [11]. The initial stage is the ground phase where the gondola carrying the payload is connected to the balloon using a crane, and the balloon is inflated. Secondly, the launch, where the balloon is released, taking care of wind direction in order to avoid a possible crash into the launch vehicle. Thirdly, the ascent phase, typically non-operative and lasts for 1-5 hours, depending on the float altitude. Fourthly, the float phase, which is the operational phase, where the actions to reach the scientific goal of the mission take place. Then, the descent, where a parachute is deployed to brake the free fall of the gondola. Finally, the landing and recovery phase, where the payload is recovered.

From a thermal point of view, it is important to analyse the float phase to ensure that the payload fulfils its requirements to achieve the main objective of the flight. However, it is necessary to

analyse the ascent phase as it may experience the lowest temperatures of the mission [12]. During the float phase, the residence time of the balloon over an area is large compared to the characteristic thermal time of the payload components, which allow us to use steady-state analysis for the float phase [13], in contrast to the case of a satellite orbiting the Earth in a low orbit. For instance, a balloon-borne system, following a westward circumpolar trajectory during the local summer, at a typical float altitude of 40 km, has an average speed of approximately of $30\,\mathrm{km}\cdot\mathrm{h}^{-1}$, what results in a view of a local point (of 1° in latitude and longitude) during almost 12 h [13]; and for a satellite at 400 km of altitude, travelling at an average speed of $8\,\mathrm{km}\cdot\mathrm{s}^{-1}$, results the pass over a local point lasts some 5-15 minutes [14]). In any case, during the ascent phase, the steady-state approach is not feasible due to the high variability of the thermal environmental conditions. This fact requires to locally study the thermal environmental conditions [13], [15].

In addition, these flights are temporarily and geographically restricted.

In space, thermal radiation becomes the primary method of heat transfer to the thermal environment due to the vacuum conditions. Similarly, in the stratosphere, the heat dissipated to the environment by convection might also be considered negligible with regard to thermal radiation. However, at the float phase, despite one could expect, the convection is not negligible if the equipment considered is radiatively and conductively isolated from the surroundings. During the ascent phase, the higher pressure in the lower layers of the atmosphere requires not only to consider the effect of forced convection on the external surfaces (due to the relative velocity of the balloon-borne system with regard to the air) [16], but also the effects of the free convection on internal components.

Thermal modelling and analysis of instrumentation on board stratospheric balloons typically involves creating a Geometrical Mathematical Model (GMM) and a Thermal Mathematical Model (TMM) using specific space sector software such as ESATAN-TMS or THERMICA. The conductive problem can be easily solved by assessing the thermal properties of the material used and determining the conductive couplings between its structural elements. The radiative module (using the GMM) allows to obtain the radiative exchange factors through the implementation of numerical methods such as the Monte Carlo Ray tracing algorithm [17]. Then, considering the thermo-optical properties of the surfaces, the absorbed fluxes can be quantified. However, since these softwares are developed for analysing the thermal behaviour of a system in the space environment, the convection heat transfer (in case it is relevant) should be implemented by modelling both the air inside the enclosure and the heat exchange with the surfaces.

In order to include the convection heat transfer into the lumped parameters method [18], experimental correlations from different authors are often used. However, main references in the literature of heat transfer are focused on obtaining the free convection coefficient for laminar and

turbulent regimes. This is useful for the thermal modelling of convection in ground and during the first stages of the ascent phase. However, for later stages, the low pressure level makes the Rayleigh number (the product of the Grashof and Prandtl numbers) to decrease reaching values of Ra$< 10^2$. For these values, the convection heat transfer has not been deeply studied. In addition, existing correlations based on experimental data show significant differences among them that could lead to considerable difference of temperatures in the results of the thermal analysis in some particular cases.

When facing the design of a stratospheric balloon payload, a problem arises when convection is needed in the analysis. On the one hand, forced convection on external surfaces needs to be quantified, based on the relative air speed as well as the air properties at any time during the flight. On the other hand, it is necessary to implement the free convection heat transfer on internal surfaces in a parametric way in order to take into account the environmental condition changes during the ascent phase. Therefore, a deep study of the thermal environmental conditions should be performed to obtain the worst-case conditions.

Furthermore, the complexity of an ascent phase analysis gives rise to a high uncertainty in the results, leading to an oversizing of the thermal control subsystem. These uncertainties can be reduced with both a suitable characterization of the thermal environment and an appropriate implementation of the convection heat transfer. The first one is achieved using real-data observations according to [15], [16]. The second one should be performed through a deep study of the phenomena supported by thermal tests correlations.

Hence, the work developed in this Doctoral Dissertation is divided into two main parts. In the first part, several tests have been carried out to obtain new convective correlations that can be applied throughout the balloon mission. In the second part, the ballooning ascent phase has been deeply studied from a thermal point of view, studying the thermal environment parameters, not only the radiative parameters and the air temperature but also the influence of every parameter on the ascent rate and the horizontal relative wind speed. For this study, it has been developed a dynamic model to simulate the balloon-borne ascent phase.

The definition of the worst-case conditions that allows a robust thermal design for mission with common characteristics, based on the ascent phase thermal analysis, has been combined with the developed correlation and applied to the TASEC-LAB mission (successfully launched in 2021). This experiment was developed at the IDR (Instituto Universitario de Microgravedad "Ignacio Da Riva") and intended to measure convective effects on a heated plate, which was both conductively and radiatively isolated.

Furthermore, to validate the described methodology, it has been used for the thermal modelling

of SUNRISE III [19], [20], a solar telescope launched in 2022 as part of the SUNRISE mission (an international project headed by the Max-Planck-Institut für Sonnensystemforschung (MPS) in collaboration with other European and global institutions), and it has also been implemented in HERCCULES (Heat-transfer and Environment Radiative and Convective Characterisation in a University Laboratory for Experimentation in the Stratosphere) [21], an experiment developed at IDR and a part of the REXUS/BEXUS programme [22]. HERCCULES was successfully flown onboard the BEXUS 32 mission in September 2023.

1.2 Stratospheric ballooning and applications

Stratospheric balloons allows the transport of payloads to altitudes of approximately 40 km or even higher. At these altitudes, 99 % of the mass of the atmosphere is left below, which is of great scientific and technological interest. In this way, stratospheric balloons provide high-altitude scientific platforms for scientific and technological research, more useful than traditional satellites for certain missions. The main advantages of this type of platforms over satellites are as follows [1]:

- Lower cost. Firstly, due to the launch vehicle is a balloon rather than a rocket, the cost of the launch itself is significantly reduced. Secondly, as the design requirements are not as stringent as for satellites (mechanical vibrations and environmental loads are not as severe as for satellites), the design time compared to a satellite is reduced. Then, the cost of a balloon experiment is at least 10 times less than for a small sounding rocket, at least 100 times less than for a large rocket and a small satellite, and at least 1,000 times less than for a large satellite [1].

- Allows to mount large and heavy payloads. Payloads exceeding one ton of mass can be lifted over 30 km. In addition, equipment up to 5 m or more can be mounted unfolded, avoiding the need for a complex in-flight deployment mechanism as would be required for rocket launches.

- Payloads can be recovered and reused. This facilitates the use of these platforms as technology demonstrators.

- Contact with the ground station. Contact with a single ground station may be permanent (except on very long missions, which can reach places far away from the launch site), in contrast to satellites which, due to the large speed of the satellite, contact lasts only 5-15 minutes [14], and therefore may require several control stations placed at different geographical areas.

The zero-pressure and the super-pressure balloons are the two main type of balloons [23]. The zero-pressure balloons are open at the bottom and have venting ducts on the side to allow the extra lifting gas to escape after the balloon has reached its maximum volume at the float altitude. The zero-pressure balloon are used in two types of missions, called "conventional" and "Long Duration Balloon" (LDB).

In conventional missions the lifetime is limited to a few hours or days due to the day/night fluctuations in buoyancy altitude (when the balloon reaches its maximum volume at buoyancy altitude, the extra gas is released, then at sunset, when the solar radiation is zero, the lifting gas temperature decreases, and then the buoyancy altitude). To avoid the loss of lift, it is common to use ballast mass, which is released at night, causing the extra lifting gas to be vented through the venting ducts at the following sunrise, to compensate for the reduction in payload mass. It is this cycling that limits the lifetime of a conventional mission. LDBs, on the contrary, avoid the limitations of the conventional type by launching under constant daylight conditions, which are achieved in the local summer at high latitude regions. For instance, at Antarctica, a LDB mission can last some 55 days [23].

The super-pressure balloon are used in missions named Ultra-Long Distance Balloons (ULDB). They are sealed at the bottom and do not have venting ducts. Then, the sunset-sunrise effect is avoided but the balloon film shall withstand the difference between the internal and external pressure. This type of mission can last up to some 100 days [23].

Besides, the lifetime of balloon-borne missions is subjected to additional constraints. The trajectory, which is entirely dependent on the wind direction, may lead the balloon-borne system into regions restricted for geopolitical reasons or over densely populated areas. Moreover, the possibility of reaching regions with unfeasible payload recovery, such as lakes or other challenging terrains, poses inherent risks. Consequently, the overall mission lifetime is constrained by safety considerations related to landing regions and geopolitical restrictions on non-accessible areas [24].

Esrange in Kiruna, Sweden in the North Hemisphere [25], [26] and McMurdo in Antarctica [27], [28] in the South Hemisphere are amongst the more relevant balloon launch sites, due to the flying conditions achieved at these regions. During the local summer, besides the existence of

constant daylight, the trajectory of the balloon-borne system becomes more predictable during this season, thanks to the stable winds associated with the polar vortex [29]. For instance, at this season in the Northern hemisphere, the wind is very stable in a westerly direction at float altitude (around 37 km), and after 4-6 days, the balloon-borne experiment may reach Russia, which is a restricted region and then the mission shall end [19], [20].

1.3 Spacecraft thermal control

Space thermal control allows the different subsystems to maintain their temperature within certain ranges during the different phases of the mission. Mechanical and electronic devices only work properly within a certain temperature range, known as the operational range. In addition, some payloads, such as telescope elements, require dimensional stability in order to function. The dimensional variation of materials (most of them have a non-zero thermal expansion coefficient) must be controlled in order to avoid observation errors. In other words, the temperature must be controlled to achieve the dimensional requirements. For these two reasons, thermal control is essential to ensure the success of the mission.

To maintain the temperature of the different devices in the correct range, the heat fluxes must be managed to reach the thermal requirements. The heat fluxes are the thermal energy transferred from one body to another due to its temperature gradient. In the following sections, the three different types of thermal energy transfer, and the usual thermal environment in space mission are summarized.

1.3.1 Mechanism of thermal energy transfer

There are three different mechanisms of thermal energy transfer which are conduction, convection and radiation.

1.3.1.1 Conductive heat transfer

Heat transfer by conduction is the flow of thermal energy between regions of matter due to a temperature gradient. The transfer of thermal energy in this mechanism is due to the motion of free electrons from regions with higher energy to regions with lower energy. Due to this fact, this phenomena requires the presence of matter. Thus, it is not possible in vacuum but it is possible

within liquids, fluids and gases [18]. Heat conduction is governed by Fourier's law which is an empirical law obtained from experimentation and observation. Fourier's law states that the rate of heat flow, $\dot{Q}$, through a uniform material is directly proportional to the area of heat transfer and to the temperature gradient, ΔT, in the direction of heat flow throughout the constant of proportionality called thermal conductivity, k, and is inversely proportional to the length of the path flow Δx [18]:

$$\dot{Q} = kA\frac{\Delta T}{\Delta x}. \tag{1.1}$$

1.3.1.2 Convection heat transfer

Conduction and convection require the presence of material medium but convection heat transfer requires the presence of fluid motion [30]. The rate of convection heat transfer is observed to be proportional to the temperature difference expressed by Newton's law cooling [31]:

$$\dot{Q} = hA(T_s - T_\infty), \tag{1.2}$$

where A is the heat transfer surface area, T_s is the temperature of the surface, T_∞ is the temperature of the fluid sufficiently far from the surface, and h is the convection heat transfer coefficient. This coefficient can be defined as the rate of heat transfer between a solid surface and a fluid per unit surface area per unit temperature difference [30]. This coefficient depends on the fluid properties dynamic viscosity μ, thermal conductivity k, density ρ, and specific heat c. It also depends on the geometry and the roughness of the solid surface and the type of fluid flow (turbulent or laminar). The difficulty to compute the convection heat transfer appears in the complexity to obtain the convection heat transfer coefficient. This mechanism is deeply explained and studied in a dedicated chapter (see chapter 2).

1.3.1.3 Thermal radiation heat transfer

All matter which is at a non-zero temperature emits electromagnetic radiation. Thermal radiation is the electromagnetic radiation emitted in the wavelength range from 0.1 µm to 100 µm which includes part of ultraviolet (UV), and the complete visible and infrared (IR) ranges.

Due to radiative heat transfer is the result of oscillations or transitions of the electrons that constitute matter there is not required material medium for its propagation such as convective or conductive heat transfer do [18].

Besides, a surface may have directions with preferential emissions. These surfaces are named directional surfaces. In thermal control, it is usual to assume that all surfaces emit omnidirectionally, in other words, there is not a direction with preferential emissions. These surfaces are named diffusive surfaces. The finishing of the surface is a key element in the radiative heat transfer.

The total energy that a body emits is proportional to the fourth power of the body temperature. This relation is defined by Stefan-Boltzmann law [18]:

$$E_b = \sigma T^4, \tag{1.3}$$

where E_b is the energy radiated per unit area, and $\sigma = 5.67 \times 10^{-8}\,\mathrm{W \cdot m^{-2} \cdot K^{-4}}$ is the Stefan-Boltzmann constant.

When radiant energy strikes a material surface, part of the radiation is reflected, part is absorbed, and part is transmitted. It is defined the reflectivity, ρ', as the fraction reflected, the absorptivity, α, as the fraction absorbed, and the transmissivity, τ, as the fraction transmitted [32]. Thus, the thermal energy absorbed, reflected and transmitted by a body are related as follows:

$$\alpha + \rho' + \tau = 1, \tag{1.4}$$

for opaque surfaces, $\tau = 0$.

The emissivity (ε) of the surface can be related with the absorptivity according to Kirchhoff's law, that establishes for each direction and wavelength, the emissivity is equal to the absorptance, and assuming diffusive surfaces [18]:

$$\alpha(\lambda_w, T) = \varepsilon(\lambda_w, T). \tag{1.5}$$

Surfaces are defined to be grey surfaces if its properties are independent of the wavelength, being its radiation emission constant with the wavelength. Hence, Kirchhoff's law becomes:

$$\alpha(T) = \varepsilon(T). \tag{1.6}$$

For convenience, α is used for short wavelengths (UV) and ε for long wavelengths (IR). This convention comes from the fact that solar radiation is concentrated in the short wavelengths whereas room temperature (ideally, the satellite temperature is close to room environment) emission is concentrated in the long wavelengths, as it is shown in Figure 1.2.

Once wavelength and temperature influence in thermal radiation have been depicted, to compute the thermal energy exchange between two surfaces, it is necessary to calculate the amount of energy emitted by one surface that reaches the other surface. In this regard, the viewfactor F_{ij}, is

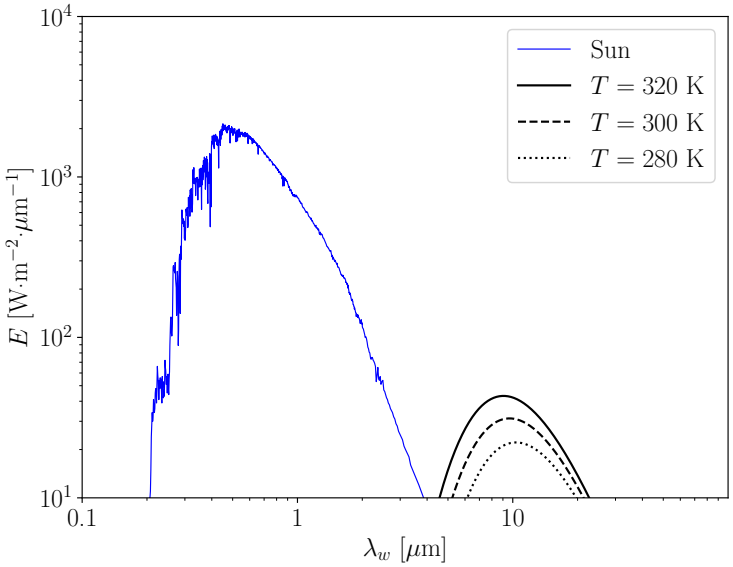

Figure 1.2: Solar and blackbody emissive power as a function of wavelength (adapted from [18]).

defined as the fraction of energy exiting an isothermal, opaque, and diffuse surface i that directly impinges in surface j [33]:

$$F_{ij} = \frac{1}{\pi A_i} \int_{A_i} \left(\int_{A_j} \frac{\cos \beta_{ij} \cos \beta_{ji}}{r_{ij}^2} \mathrm{d}A_j \right) \mathrm{d}A_i, \tag{1.7}$$

where A_i is the area of the surface i, A_j is the area of surface j, r_{ij} is the distance between the surfaces i and j, and β is the tilting angle relative to the line of centres.

The radiation heat exchanges between only two surfaces can be computed as:

$$\dot{Q}_{ij} = A_i F_{ij} \varepsilon_i \alpha_j \sigma (T_j^4 - T_i^4), \tag{1.8}$$

1.4 Thermal environment

Once the spacecraft is placed on its orbit, the heats loads from the thermal environment depend on the mission (orbit a planet or deep space). For the particular case of orbiting a planet, the main

sources of heat loads are solar radiation (direct and reflected by the planet), and the infrared energy emitted by the planet, as it is shown in Figure 1.3.

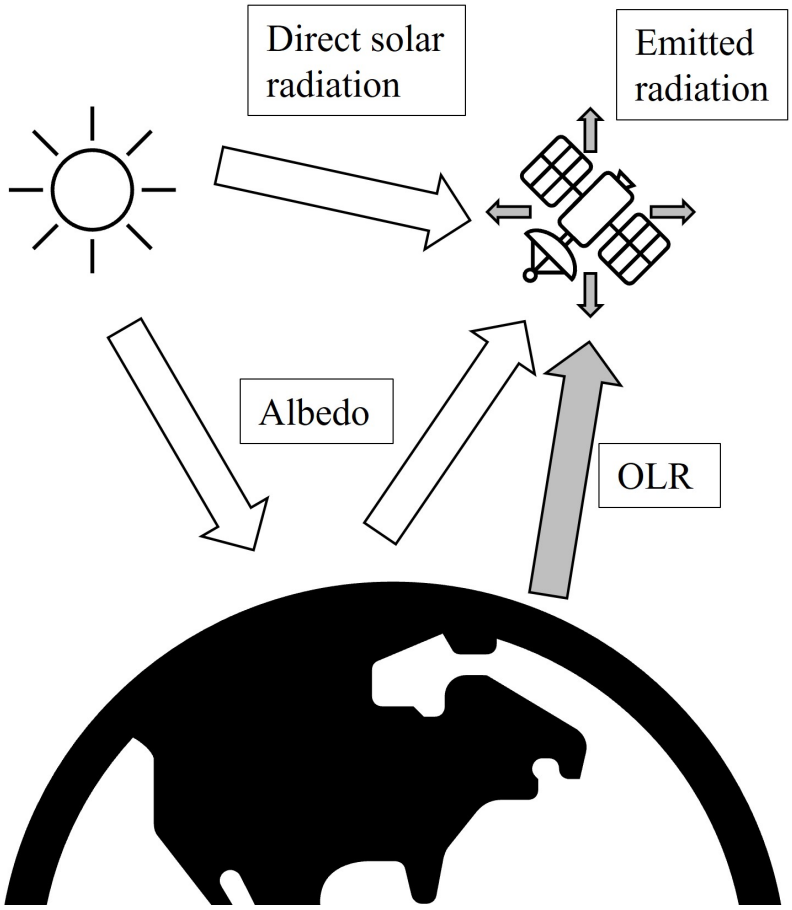

Figure 1.3: Thermal environment for a spacecraft orbits a planet (adapted from [18]).

In the following subsections the solar, albedo and planetary radiation are summarized.

1.4.1 Solar radiation

Solar radiation is the most important energy source for the majority of the spacecrafts. Its spectral distribution can be represented mathematically as the thermal energy emitted by a blackbody at a temperature of $T = 5762$ K [18] as it is shown in Figure 1.4.

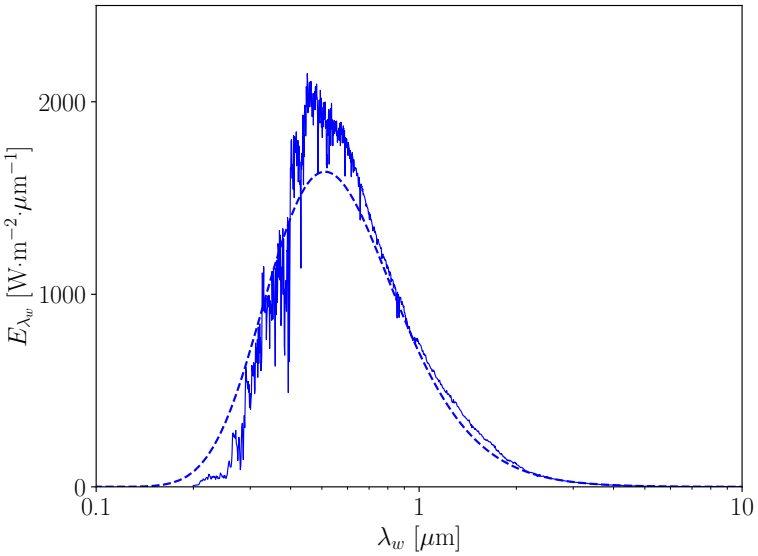

Figure 1.4: Spectral distribution of solar irradiation at 1AU at different wavelengths, λ_w. Spectral emissive power, E_{λ_w} (solid line). Spectral emissive power of the Sun as a blackbody at 5672 K at Earth's orbit (dashed-line) (adapted from [18]).

Approximately 99 % of the solar radiation is emitted between 150 nm and 10 µm. The maximum takes place at 0.45 µm [34].

The integrated spectral irradiance at 1 AU is the so called "Solar constant", $G_s = 1366.1 \pm 21\ \mathrm{W \cdot m^{-2}}$ [35].

The solar constant value as a function of the distance d between the spacecraft and the Sun can be computed:

$$G_s(d) = G_s(d_o)\left(\frac{d_o}{d}\right)^2, \tag{1.9}$$

where $d_o = 1$ AU.

A simple analytical model to compute the solar direct radiation absorbed by a flat plate of surface A, considering solar radiation with parallel rays, and the surface normal vector forms an angle θ_s with the solar rays [18] is given by the expression:

$$\dot{Q}_s = \alpha G_s A \cos\theta_s, \tag{1.10}$$

where α is the absorptivity of the surface.

1.4.2 Albedo

Albedo is the fraction of the solar radiation reflected or scattered by the planet surface and/or the atmosphere (if any) [36]. Its magnitude increases as the orbit altitude decreases, and this heat load only appears in the lighted regions of the planet (in case of eclipse, there is not albedo heat load). Albedo radiation has approximately the same spectral distribution as the Sun and it is supposed to be diffuse [37]. The albedo load is quantified through the albedo coefficient, a, which determines the fraction of solar energy reflected again to the space from the planet. Its value depends strongly on the optical characteristics of the planet surface. In case of a variable surface, such as of the Earth, this coefficient can vary from 0.1 (ocean surface) to 0.95 (ice or snow surface) [18]. In continental areas, the albedo coefficient can be range from small values over forests to higher values over desert areas. The presence of clouds is also an important factor. According to [37] the average albedo coefficient of the Earth is 0.3.

The calculation of the albedo loads on the spacecraft must consider the solar zenith angle, θ (see Figure 1.5). This angle is defined as the angle between the Sun-planet vector and the planet-spacecraft vector. Assuming that the planet behaves as a reflecting sphere [18], the albedo energy absorbed by a surface A, can be computed as:

$$\dot{Q}_{albedo} = aG_sAF_{SC-P}\cos\theta, \quad -\frac{\pi}{2} < \theta < \frac{\pi}{2} \tag{1.11}$$

where F_{SC-P} is the viewfactor between the surface and the planet.

1.4.3 Planetary thermal radiation

Planetary radiation is the thermal radiation emitted by the planet, also called Outgoing Longwave Radiation (OLR). It is referred to the radiation emitted by the planet's surface and the atmospheric gases. It is considered diffuse within the IR band [36]. As it happens with albedo, the temperature of the Earth surface varies geographically. The average infrared radiation emitted by the Earth is 230 $\mathrm{W \cdot m^{-2}}$. This value can be obtained from the assumption that the thermal energy emitted by Earth can be characterized by the Earth's blackbody equivalent temperature. The energy balance is defined by [18]:

$$G_s\pi R_E^2(1-a) = 4\pi R_E^2\sigma T_E^4, \tag{1.12}$$

where the left-hand side of the equation is the solar energy absorbed minus the solar energy reflected (albedo) and the right-hand side is the thermal energy emitted by Earth. Using the average albedo coefficient $a = 0.3$, the equivalent temperature is $T_E = 255$ K.

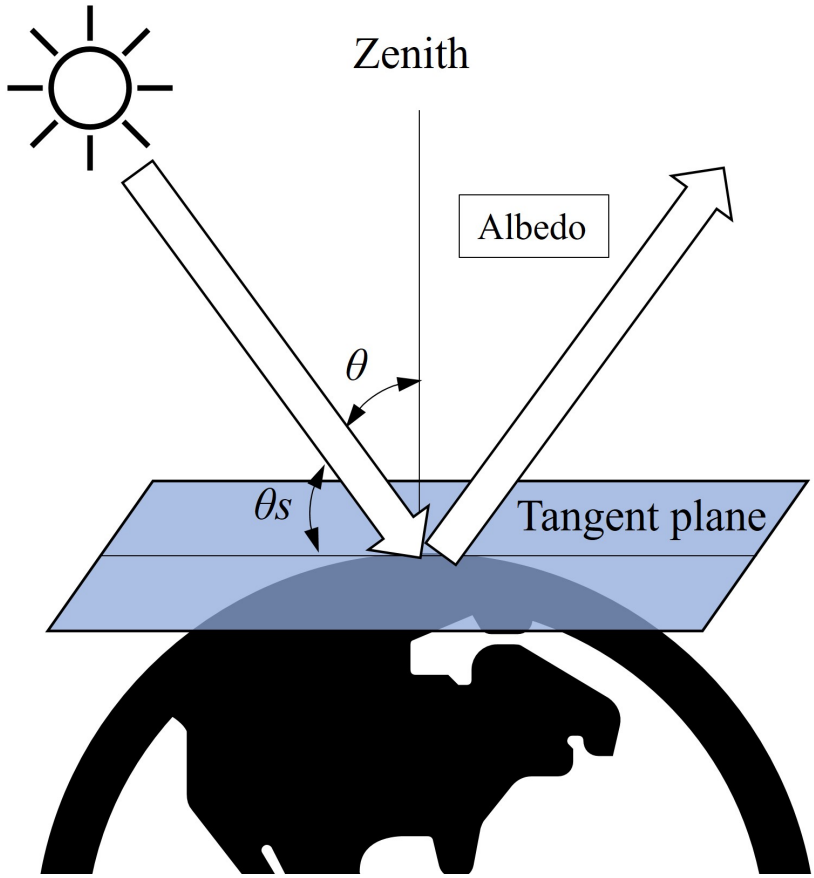

Figure 1.5: Albedo scheme. θ : Solar Zenith Angle; θ_S : Sun Elevation Angle.

For an orbiting spacecraft it can vary from 150 W · m^{-2} to 350 W · m^{-2} [37].

Finally the planetary thermal infrared load on a spacecraft surface, $\dot{Q}_p$, can be computed as a function of the blackbody planet's temperature [18]:

$$\dot{Q}_p = \varepsilon A F_{SC-P} \sigma T_p^4, \tag{1.13}$$

where F_{SC-P} is the viewfactor between the spacecraft surface and the planet, ε is the infrared emissivity of the spacecraft surface, and A is the area of the surface.

1.5 Thermal Model. Lumped Parameters Method

The mathematical model used along this work is based on the Lumped Paramters Method (LPM) using the software ESATAN-TMS. This method is based on the discretisation of a continuous medium as a discrete network of nodes representing the capacitance of the system linked by conductive (G_L) and radiative (G_R) couplings [38]. The basic justification for this spatial discretisation is the isothermal assumption, meaning that each node is considered as isothermal. Hence, in regions where spatial temperature gradient exists, more nodes are needed to fulfil the isothermal assumption [35].

These nodes include information relative to the bulk and the thermo-optical properties making possible to complete the GMM (Geometrical Mathematical Model).

Once the GMM has been built, the geometry is used to compute the radiative thermal environment loads and the conductor and radiative couplings between nodes. This result is the definition of the TMM (Thermal Mathematical Model) making the system ready to be solved.

LPM can be seen as a means of deriving a first-order finite-difference approximation to the governing differential equation [38].

Supposing an spacecraft orbiting a planet, discretized as a model of N nodes, where C_i is the heat capacity, T_i is the temperature, $\dot{Q}_i$ is the internal heat load, and $\dot{Q}_{load,i} = \dot{Q}_P + \dot{Q}_{albedo} + \dot{Q}_S$ is the environmental heat load absorbed by the node i, the energy balance is approached by [38]:

$$C_i \frac{\mathrm{d}T_i}{\mathrm{d}t_i} = \sum_{i \neq j}^{N} K_{ij} \left(T_j - T_i\right) + \sum_{i \neq j}^{N} R_{ij} \left({T_j}^4 - {T_i}^4\right) + \dot{Q}_i + \dot{Q}_{load,i}, \tag{1.14}$$

where the linear couplings (G_L) between node i and node j is K_{ij}, and the radiative exchange constant between those nodes is R_{ij}. Hence, solving the N first order differential equations with enough boundary conditions, the temperature of the nodes and the heat fluxes exchange between them are obtained.

The differential system is solved by numerical methods. The criteria to select the correct time step is to achieve the convergence of the solution, and to resolve the characteristic times of the phenomena involved, sustaining the physical sense of the problem.

Chapter 2. Convection

2.1 Introduction

The convection, as it has previously been commented in subsubsection 1.3.1.2, is the heat transfer mechanism between a solid surface and the adjacent fluid in motion, and it involves two different mechanisms [39]. One is the random molecular motion of the fluid (diffusion), and the other one, the macroscopic (bulk) motion of the fluid (advection). Then, if the fluid and the solid surface are at different temperatures, there will be a heat transfer. The term convection refers to the superposition of energy transport by the random motion of the molecules and by the bulk motion of the fluid, as the molecules, in the aggregate, retain their random motion [39]. According to the nature of the fluid flow, convection may be classified into natural (or free) convection and forced convection. In natural convection, the source of the macroscopic fluid motion is caused by the buoyancy forces induced by the temperature gradient (density gradient) [30]. In contrast, in forced convection, the macroscopic motion is caused by an external source such as a fan or the wind [32]. It is obvious that the greater the random molecular motion (or in other words, the lower the distance between the molecules), the larger the frequency of the impacts with the solid surface and, thus, the heat transfer.

Similarly, with regard to the macroscopic motion, the greater the velocity of the fluid, the greater the heat transfer. According to this definition, one may think that there will be a region in the fluid close to the solid surface and the fluid where the fluid velocity varies from zero at the surface to the unperturbed fluid velocity, u_∞. In fact, this region is called velocity boundary layer, δ_v. Then, close to the solid surface, the heat transfer is dominated by the random molecular motion (actually, due to the no-slip condition, at the interface between the solid surface and the fluid, the velocity is null, and the random molecular motion is the only contributor to the heat transfer).

For the same reason as for the velocity boundary layer, there will be a thermal boundary layer

where the fluid temperature varies from the solid surface temperature, T_s at the interface, (due to the no-temperature-jump condition) to the unperturbed fluid temperature T_∞. The thermal boundary layer may be larger, equal or smaller than the velocity thermal gradient, and is the key to properly understand the convection mechanism. As one may anticipate, the analysis of the convection heat transfer is strongly related to the fluid mechanics. An scheme of the velocity and thermal boundary layer is represented in Figure 2.1, where δ_T is the thickness of the thermal boundary layer, and it is typically defined as the value y where the condition $\frac{T_s - T_{y=\delta_T}}{T_s - T_\infty} = 0.99$ is verified, and δ_v is the thickness of the velocity boundary layer, and it is typically defined as the value y where the condition $u_{y=\delta} = 0.99 u_\infty$ is verified [39].

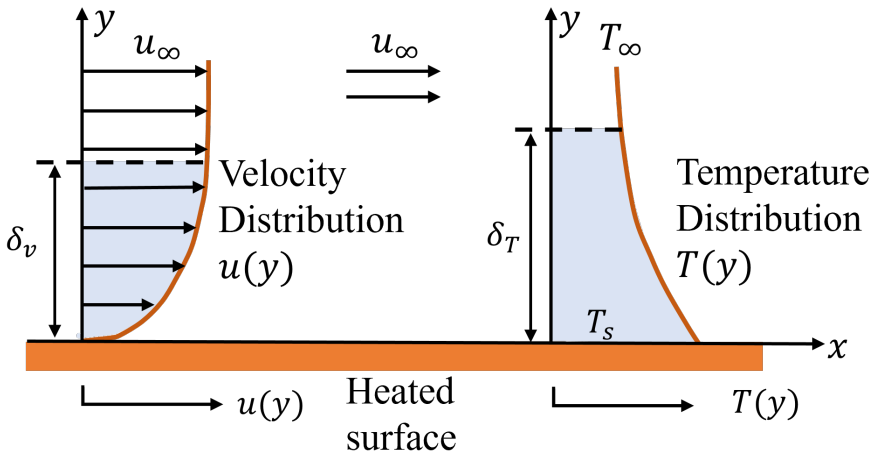

Figure 2.1: Scheme of the thermal and velocity boundary layers near a plate parallel to a uniform flow (adapted from [32]).

Whatever the nature of the convective heat transfer process, the appropriate analytical expression to compute the convective heat transfer is the Newton's law of cooling [39]:

$$\dot{Q}_{conv} = hA(T_s - T_\infty), \tag{2.1}$$

where A is the heat transfer surface area, and h is the convection heat transfer coefficient. This coefficient can be defined as the rate of heat transfer between a solid surface and a fluid per unit surface area and per unit temperature difference [30]. Experience shows that this coefficient not only depends on the fluid properties but also depends on the boundary layer conditions, which are influenced by the geometry, the nature of the fluid motion, and a set of fluid, thermodynamic and transport properties [39]. The convection heat transfer coefficient, h, is more often determined experimentally. Typical values for this coefficient are given in Table 2.1.

Table 2.1: Typical values of the convection heat transfer coefficient, h [39].

Fluid	Type of convection	h [W · m^{-2} · K^{-1}]
Gas	Free	2-25
	Forced	25-250
Liquid	Free	50-1000
	Forced	100-20000

The analytical expression for the coefficient h is derived from both the no-slip condition and the no-temperature-jump condition. These conditions imply that the heat transfer from the solid surface to the fluid layer close to the surface ($y \to 0^+$ in Figure 2.1) is by pure conduction [30], as there is no motion in the fluid, and it can be stated:

$$\dot{q}_{conv} = \dot{q}_{cond} = -k_{fluid} \left. \frac{\partial T}{\partial y} \right|_{y=0^+}, \tag{2.2}$$

and using (2.1) and (2.2):

$$h = \frac{-k_{fluid} \left. \frac{\partial T}{\partial y} \right|_{y=0^+}}{(T_s - T_\infty)}, \tag{2.3}$$

where k_{fluid} is the fluid thermal conductivity.

As the temperature and velocity boundary layer usually varies along x-axis, the heat transfer rate $\dot{q}$ for the entire surface can be calculated through the average convection heat transfer coefficient, $\bar{h}_L$. For instance, in the scenario where the surface is a flat plate:

$$\bar{h}_L = \frac{1}{L} \int_0^L h \mathrm{d}x. \tag{2.4}$$

When a thermal engineer is facing a problem where the convection heat transfer shall be considered, two approaches can be followed to obtain the convection heat transfer coefficient. One approach is to obtain the profile of the temperature fluid field solving the analytical equations of mass, momentum and energy balance. The other one is to use experimental correlations defined through dimensionless parameters that quantifies the convection heat transfer (see section 2.3).

The first approach requires Computational Fluid Dynamics (CFD) computations due to the equations are usually too complex to be solved analytically and numerical methods should be used (even for simple applications such as a flat plate parallel to uniform flow). The second approach is simpler and faster, but it can only be used under the same assumptions as the experiments developed to obtain the correlations, and in applications where the temperature fluid field determination is not required.

In the particular case of a hot plate immersed in a fluid at rest, (assuming natural convection flow) a steady, laminar, two-dimensional flow can be considered with constant properties (such as the dynamic viscosity, μ), except for the density difference $\rho - \rho_\infty$ between the inside and outside boundary layer (Boussinesq approximation [40]), as it shown in Figure 2.2, and the motion equations can be written as follows [30]:

- Conservation of mass

$$\frac{\partial u}{\partial x} + \frac{\partial v}{\partial y} = 0, \tag{2.5}$$

- Momentum balance

$$\rho\left(u\frac{\partial u}{\partial x} + v\frac{\partial u}{\partial y}\right) = g\left(\rho_\infty - \rho\right) + \mu\frac{\partial^2 u}{\partial y^2}, \tag{2.6}$$

- Energy balance

$$\left(u\frac{\partial T}{\partial x} + v\frac{\partial T}{\partial y}\right) = \alpha_D\frac{\partial^2 T}{\partial y^2}. \tag{2.7}$$

where $\alpha_D = \dfrac{k}{\rho c_p}$ and it is the thermal diffusivity, which represents how fast heat diffuses through the fluid (the larger the thermal diffusivity, the faster the propagation of heat).

The momentum balance equation can be rewritten using the volume expansion coefficient, β, which represents the variation of the density of a fluid with temperature at constant pressure:

$$\beta = -\frac{1}{\rho}\left(\frac{\partial \rho}{\partial T}\right)_p \approx -\frac{1}{\rho}\frac{\rho_\infty - \rho}{T_\infty - T}, \tag{2.8}$$

then, the momentum equation:

$$u\frac{\partial u}{\partial x} + v\frac{\partial u}{\partial y} = g\beta\left(T - T_\infty\right) + \nu\frac{\partial^2 u}{\partial y^2}, \tag{2.9}$$

where $\nu = \dfrac{\mu}{\rho}$ is the kinematic viscosity.

It is clearly shown in the previous equations that free convection is related to the volume expansion coefficient β, which for an ideal gas ($p = \rho RT$) is given by:

$$\beta = \frac{1}{T}. \tag{2.10}$$

The equations (2.5)-(2.7) can be expressed in terms of the appropriate dimensionless parameters [30]:

$$x^* = \frac{x}{L}, \quad y^* = \frac{y}{L}, \quad u^* = \frac{u}{u_o}, \quad v^* = \frac{v}{u_o}, \quad \text{and} \quad T^* = \frac{T - T_\infty}{T_s - T_\infty}, \tag{2.11}$$

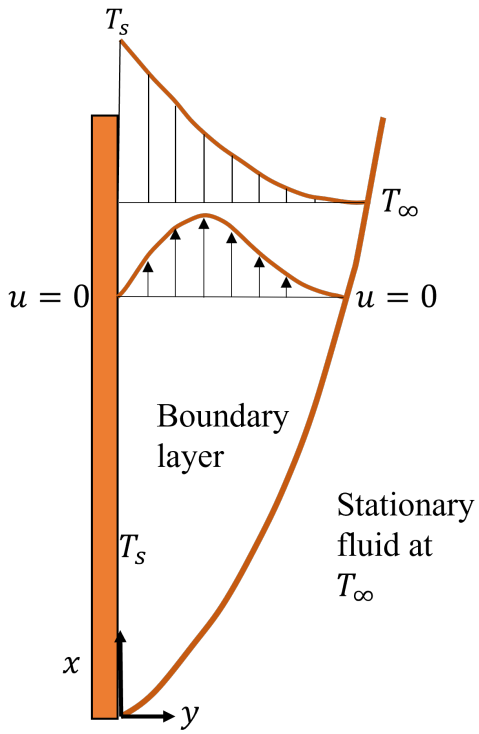

Figure 2.2: Natural convection flow over a hot vertical plate immersed in a fluid application. Scheme of typical velocity and temperature profiles (adapted from [31]).

where L is the characteristic length of the problem, and u_o is an arbitrary reference velocity (as free convection is defined assuming the free stream is at rest, there is not external reference velocity).

Then the mass, momentum and energy balance equations are rewritten using the previous dimensionless parameters as:

- Mass

$$\frac{\partial u^*}{\partial x^*} + \frac{\partial v^*}{\partial y^*} = 0, \tag{2.12}$$

- Momentum

$$u^* \frac{\partial u^*}{\partial x^*} + v^* \frac{\partial u^*}{\partial y^*} = g\beta \left(T_s - T_\infty\right) \frac{L}{u_o^2} T^* + \frac{\nu}{u_o L} \frac{\partial^2 u^*}{\partial y^{*2}}, \tag{2.13}$$

- Energy

$$u^* \frac{\partial T^*}{\partial x^*} + v^* \frac{\partial T^*}{\partial y^*} = \frac{\alpha_D}{u_o L} \frac{\partial^2 T^*}{\partial y^{*2}}. \tag{2.14}$$

2.2 Dimensionless numbers

The most relevant dimensionless numbers required to describe the free convection heat transfer are the following ones:

- Reynolds number, Re. It determines whether the fluid flow is laminar or turbulent at forced convection heat transfer applications. It is defined by the ratio of the inertia forces to viscous forces in the fluid:

$$\mathrm{Re} = \frac{u_o L}{\nu}, \tag{2.15}$$

  where u_o is the upstream velocity (equivalent to the free-stream velocity u_∞ in forced convection.

- Prandtl number, Pr. The thickness of the velocity and thermal boundary layers have an impact on the heat transfer. Then, the Prandtl number is defined by the ratio of the molecular diffusivity momentum and the molecular diffusivity of heat:

$$\mathrm{Pr} = \frac{\nu}{\alpha_D} = \frac{c_p \mu}{k}. \tag{2.16}$$

  One can note that for Pr$\ll$1, the thermal boundary layer is much thicker than the velocity boundary layer, and the heat dissipates very quickly. For gases, Pr ≈ 1.

- Grashof number, Gr. It provides a measure of the ratio of buoyancy forces to viscous forces in the velocity boundary layer [30]:

$$\mathrm{Gr} = \frac{g\beta \left(T_s - T_\infty\right) L^3}{\nu^2}. \tag{2.17}$$

  In natural convection, the Grashof number plays the same role in free convection heat transfer applications as the Reynolds number does in forced convection heat transfer applications.

- Rayleigh number, Ra. It is defined by:

$$\mathrm{Ra} = \mathrm{GrPr}. \tag{2.18}$$

- Nusselt number, Nu. It represents the enhancement of heat transfer through a fluid layer as a result of convection compared with pure conduction [32]:

$$\mathrm{Nu} = \frac{\dot{q}_{conv}}{\dot{q}_{cond}} = \frac{hL}{k}, \tag{2.19}$$

  where k is the thermal conductivity of the fluid. Thus, the case where the fluid is motionless, Nu $= 1$, represents the heat transfer across the layer by pure conduction.

- Kundsen number, Kn. In some applications, there is heat transfer between the solid surface and a low-density gas, where the mean free path of the gas molecules, λ_c, is not small compared with the characteristic length, L, of the heat transfer [32] (free molecule regime). Then, the assumption that the molecules of the gas impacts immediately with both their neighbour molecules and the solid surface, communicating the molecule temperature (continuum regime), may be no longer assumed. The Knudsen number, Kn, determines the rarefaction of the fluid (the term rarefaction means that the molecular mean free path λ_c is not small compared to the characteristic length L), or in other words, it determines the regime of the fluid [32]:

$$\mathrm{Kn} = \frac{\lambda_c}{L}, \tag{2.20}$$

  Between the continuum and free molecule regimes there is a wide range of rarefied flow situations [41], and it is appropriate to divide rarefied gas dynamics problems into the following regimes [41], [42]; free molecule (Kn > 10), transition (10 > Kn > 0.1), temperature jump (slip) (0.1 > Kn > 0.01), and continuum (Kn < 0.01).

2.3 Boundary layer dimensionless equations

Then, taking into account the Re and Pr definition, the mass, momentum and energy conservation dimensionless equations $((2.12), (2.13), (2.14))$, can be rewritten as follows:

- Mass

$$\frac{\partial u^*}{\partial x^*} + \frac{\partial v^*}{\partial y^*} = 0, \tag{2.21}$$

- Momentum

$$u^* \frac{\partial u^*}{\partial x^*} + v^* \frac{\partial u^*}{\partial y^*} = g\beta \left(T_s - T_\infty\right) \frac{L}{u_o^2} T^* + \frac{1}{\mathrm{Re_L}} \frac{\partial^2 u^*}{\partial {y^*}^2}, \tag{2.22}$$

- Energy

$$u^* \frac{\partial T^*}{\partial x^*} + v^* \frac{\partial T^*}{\partial y^*} = \frac{1}{\mathrm{Re_L Pr}} \frac{\partial^2 T^*}{\partial {y^*}^2}. \tag{2.23}$$

As above mentioned, the reference velocity is defined arbitrarily, then, for convenience, here it is defined as:

$$u_0^2 = g\beta \left(T_s - T_\infty\right) L, \tag{2.24}$$

and, therefore,

$$\mathrm{Re_L}^2 = \frac{g\beta\left(T_s - T_\infty\right)L^3}{\nu^2} = \mathrm{Gr}, \tag{2.25}$$

where Gr, is the Grashof number. It determines whether the fluid regime is laminar or turbulent in natural convection [30], and it plays the equivalent role (or more accurate, $\mathrm{Gr}^{1/2}$) as the Reynolds number does in forced convection. Then, (2.22) becomes:

$$u^*\frac{\partial u^*}{\partial x^*} + v^*\frac{\partial u^*}{\partial y^*} = \frac{\mathrm{Gr_L}}{\mathrm{Re_L^2}}T^* + \frac{1}{\mathrm{Re_L}}\frac{\partial^2 u^*}{\partial {y^*}^2}, \tag{2.26}$$

where the term multiplying T^* at the right hand side becomes unity at free convection heat transfer applications, and the heat transfer correlations are expected to be $\mathrm{Nu} = f(\mathrm{Gr}_L, \mathrm{Pr})$. However, in some applications, the intensity of the forced and free convection effects are of the same order of magnitude. Then, the speed $u_\infty > 0$ (see Figure 2.2), and the term multiplying T^* is not unity. In these situations, $\mathrm{Nu} = f\left(\mathrm{Re}_L, \mathrm{Gr}_L, \mathrm{Pr}\right)$.

2.4 Free and forced convection combination

It has been mentioned that the convection heat transfer may be classified into forced convection heat transfer and free convection heat transfer, according to the fluid motion source. The correlations and the equations that governs forced convection assume that free convection is negligible [39], however, as above mentioned, free convection heat transfer can appear if there is a temperature gradient between the solid surface and the fluid. Then, there may be situations where forced convection heat transfer is not strong enough to neglect free convection heat transfer [30].

As above mentioned, the Grashof number determines the laminar or turbulent regime in natural convection, as the Reynolds number does in forced convection. In addition, the Grashof has its equivalence in natural convection with the Re^2. Therefore, the $\mathrm{Gr}/\mathrm{Re}^2$ ratio can be used to determine whether the application under study can be considered as forced convection $\mathrm{Gr}/\mathrm{Re}^2 \ll 1$ [43], as natural convection $\mathrm{Gr}/\mathrm{Re}^2 \gg 1$ or a combination or mixture of both, $\mathrm{Gr}/\mathrm{Re}^2 \approx 1$.

Thus, in the situations where $\mathrm{Gr}/\mathrm{Re}^2 \approx 1$, the Nusselt number computation using the experimental approach is obtained combining the Nusselt obtained from pure forced convection, Nu_F, with the Nusselt obtained from pure free convection, Nu_{Free} [43]:

$$\mathrm{Nu}_{combined} = \left(\mathrm{Nu}_F^n \pm \mathrm{Nu}_{Free}^n,\right)^{\frac{1}{n}} \tag{2.27}$$

The sign between the Nusselt numbers for pure free and forced convection depends on the relative direction between the buoyancy motion generated by the temperature gradient and the forced flow. For instance, in the situation of a hot vertical plate immersed in a forced flow with its source located at the bottom of the plate or transverse to the plate, the buoyancy currents assist the forced flow. However, when the source is at the top of the plate, the buoyancy currents are in opposite direction to the forced flow.

The value of the exponent, n, depends on the geometry, and it is obtained from experimental data. For vertical plates, the use of $n = 3.0$, gives a good correlation with experimental data [39]. However, for horizontal plates (transverse flow) an exponent $n = 3.5$ is more suitable [39].

2.5 Stratospheric flight conditions

The convection heat transfer between the stratospheric balloon-borne experiments and the surrounding air (inner or outer) varies with altitude. This is due to, during the ascent phase of stratospheric balloon-borne experiments to reach the float altitude (depending on the mission between 25 to 40 km), the air properties (temperature, pressure, density) change with altitude. The ISA air temperature, the air density and air pressure profiles [44] are shown in Figure 2.3.

In addition, the air thermal conductivity, dynamic viscosity and Prandtl number depends only on the temperature [45], (and not in the pressure [39]):

- Air thermal conductivity, k.

$$k = \frac{2.681\,51 \times 10^{-3} \cdot T^{3/2}}{T + 245.4 \times 10^{-12/T}} \quad [\mathrm{W \cdot m^{-1} \cdot K^{-1}}] \tag{2.28}$$

- Air dynamic viscosity, μ.

$$\mu = \frac{1.458 \times 10^{-6} \cdot T^{3/2}}{T + 110.4} \quad [\mathrm{kg \cdot m^{-1} \cdot s^{-1}}] \tag{2.29}$$

- Air Prandtl number, Pr.

$$\mathrm{Pr} = 0.804 - 3.25 \times 10^{-4} \cdot T \tag{2.30}$$

Therefore, these parameters change along the ascent phase due to the ambient air temperature variation. However, as above mentioned, the correlations are typically evaluated at the temperature film, then, the surface temperature has an influence in the evaluation of these properties. The profiles of these properties at different surface temperature, T_s, are shown in Figure 2.4.

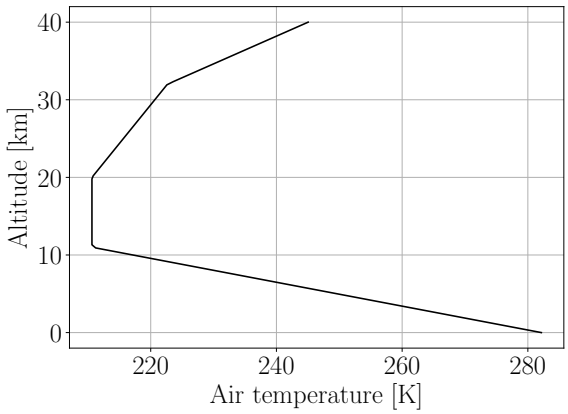

(a)

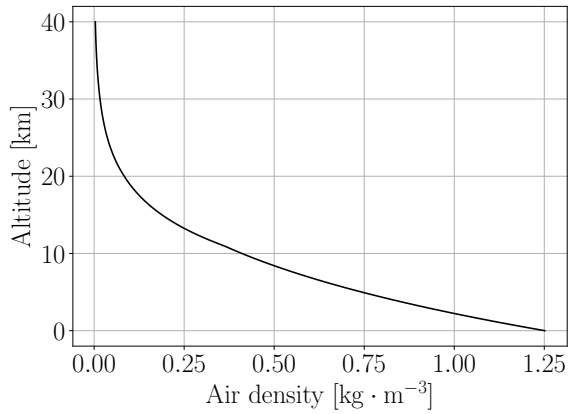

(b)

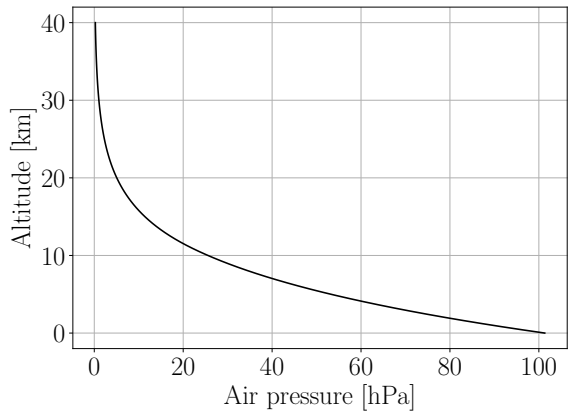

(c)

Figure 2.3: Air temperature (a), air density (b), and air pressure (c) ISA profiles [44].

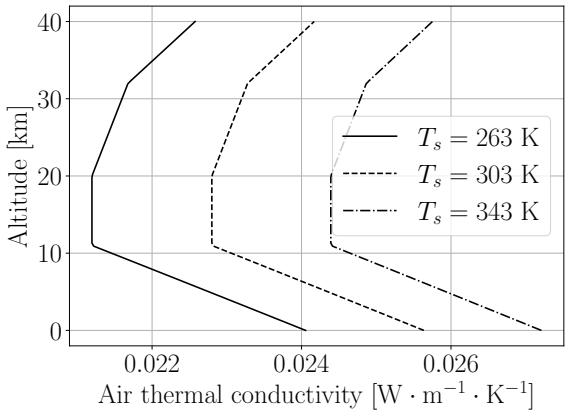

(a)

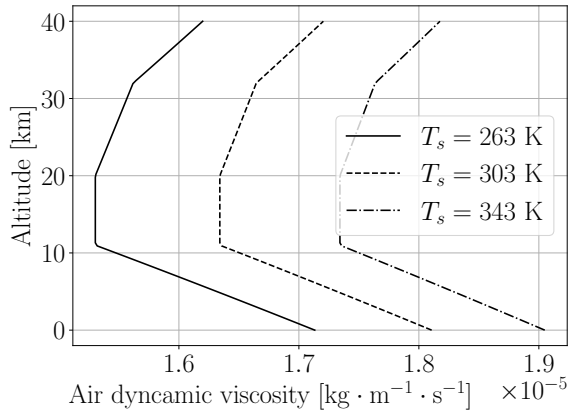

(b)

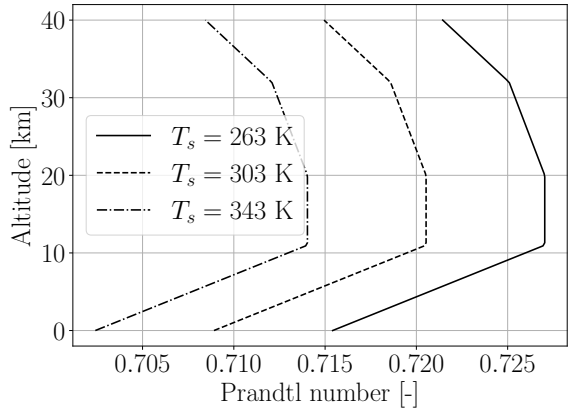

(c)

Figure 2.4: Air thermal conductivity (a), air dynamic viscosity (b), and air Prandtl number (c) profiles [45] comparison. Solid line: properties evaluated at surface temperature $T_s = 263$ K; dashed-line: $T_s = 303$ K; dot-dashed line: $T_s = 343$ K.

The mean free path, λ_c, to compute the Knudsen number, is defined by [46], [47]:

$$\lambda_c = \frac{\mu\sqrt{2\pi R_a T}}{2p}, \tag{2.31}$$

where R_a is the air gas constant.

The variation of the Rayleigh and Knudsen numbers during the ascent phase, for different characteristic length L at different surface temperature T_s, are represented in Figure 2.5.

It is well appreciated that the Knudsen number is smaller than 1×10^{-3} in all cases analysed so that continuum regime can be assumed except for the characteristic length of $L = 1 \times 10^{-3}$ m once the altitude is above 35 km. Concerning the Rayleigh number, the variation from the ground to the float altitude covers a range that depends on the temperature and characteristic length of the application.

2.6 Horizontal flat plate correlation review

This section provides a summary of various existing studies devoted to determine the Nusselt number for flat heated plates in a horizontal position within the expected Rayleigh range for stratospheric flights.

For large Rayleigh numbers, which are expected at the beginning of the ascent phase, there are different correlations in the literature whose use is very contrasted [30], [32], [39], [48]. However, for flat plates at small Ra numbers, which is expected to happen as the balloon rises (as seen in the Figure 2.5a), there is no consistent standard in the literature regarding the application of correlations.

Numerical simulations of a heated horizontal plate were performed by Suriano [49], that propose Nu values for both the lower face and the upper face in the range of Ra ≤ 300.

The average results differ very little from those presented by Buznik [50] (obtained from experimental data) for Ra < 100. However, in the range $100 <$ Ra ≤ 300, as the Ra increases, the difference between them increases.

A correlation for the downward face (opposite to the buoyancy motion) and another one for the upward face (buoyancy direction) were proposed by Goldstein and Lau [51]. The combination of both correlations can be applied in the Ra number range $250 <$ Ra $< 4.5 \times 10^3$, showing the same trend as the previous references.

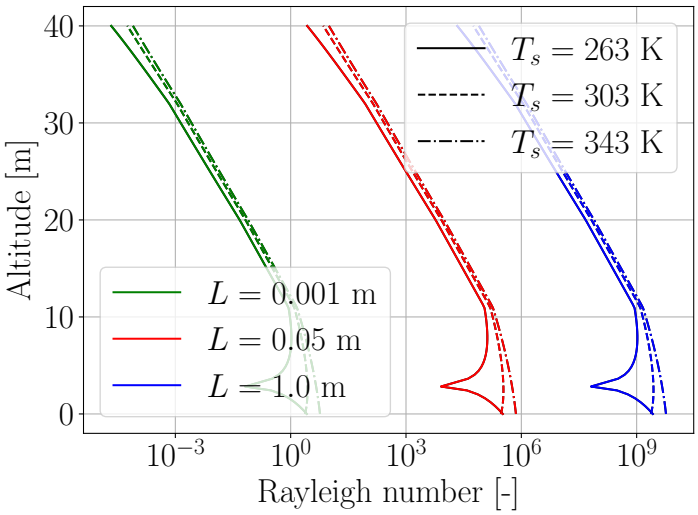

(a) Rayleigh number profile comparison.

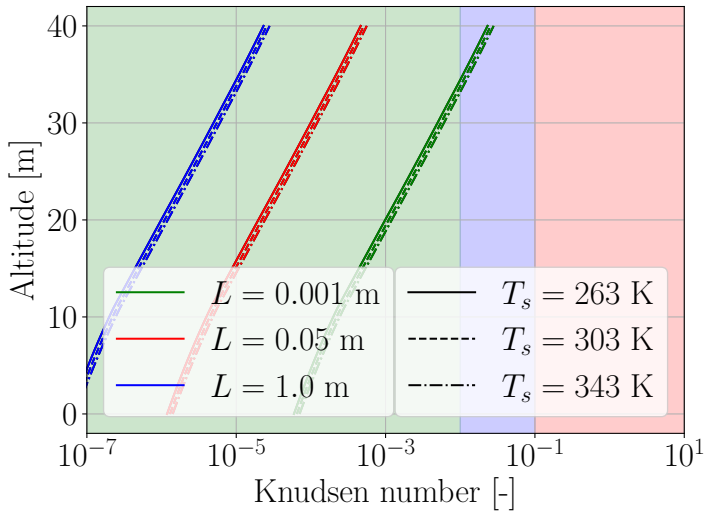

(b) Knudsen number profile comparison. Green background represents continuum regime; Blue: slip jump regime; Red: transition regime.

Figure 2.5: Rayleigh number and Knudsen number profiles comparison. Solid line: properties evaluated at surface temperature $T_s = 263$ K; dashed-line: $T_s = 303$ K; dot-dashed line: $T_s = 343$ K. Black line: $L = 1 \times 10^{-3}$ m; blue line: $L = 5 \times 10^{-2}$ m; red line: $L = 1.0$ m.

Horizontal heated plates were numerically analysed by a difference-finite method by Miyamoto [52], who proposed a new correlation in terms of Rayleigh number $2.88 < \text{Ra} < 19.44 \times 10^3$ to obtain the average Nusselt.

A numerical study of local and average natural convection was performed by Chambers [53], who proposed two correlations, one for the upper side and another one for the lower face, for a Ra range $86 < \text{Ra} \leq 1.4 \times 10^4$.

Finally, a experimental study of the natural convection at different pressure levels was performed by Liu [54], who proposed a correlation valid on the Ra range $1 \times 10^3 < \text{Ra} < 1 \times 10^7$, for a plate with double sided convection. However, they calculated β based on T_∞ instead of T_{film}, then the trend for the Rayleigh number may differ with regard to the previous correlation hereby described.

The correlations found in the literature for the expected Ra range during the flight of a stratospheric balloon payload are summarized in Table 2.2, Table 2.3, and Figure 2.6. In Table 2.2, the correlations distinguish between the lower and the upper sides, while in Table 2.3, the correlations consider both sides.

Table 2.2: Literature correlations comparison in terms of Nusselt number as a function of Rayleigh numbers, for horizontal plates with the downward face isolated and the upward face heated (U), and vice-versa (D).

Correlation	Rayleigh range	Comment	Data source	Reference
$\text{Nu} = 0.54\text{Ra}^{1/4}$	2×10^4 - 8×10^6	(U)	Experimental	LLoyd [55]
$\text{Nu} = 0.15\text{Ra}^{1/3}$	8×10^6 - 1×10^{11}			
$\text{Nu} = 0.27\text{Ra}^{1/4}$	1×10^5 - 1×10^{11}	(D)		
$\text{Nu} = 1.030\text{Ra}^{1/7}$	86 - 1.4×10^3	(U)	Numerical	Chambers and Lee [53]
$\text{Nu} = 0.677\text{Ra}^{1/5}$	1.4×10^3 - 9.1×10^5			
$\text{Nu} = 1.076\text{Ra}^{1/6}$	9.1×10^5 - 1.6×10^8			
$\text{Nu} = 1.033\text{Ra}^{1/7}$	86 - 9.1×10^5	(D)		
$\text{Nu} = 0.747\text{Ra}^{1/6}$	9.1×10^5 - 1.6×10^8			
$\text{Nu} = 0.746\text{Ra}^{1/5}$	10 - 4.8×10^3	(U)	Experimental	Goldstein and Lau [51]
$\text{Nu} = 0.906\text{Ra}^{0.089}$	10 - 2.5×10^2	(D)		
$\text{Nu} = 0.495\text{Ra}^{1/5}$	2.5×10^2 - 4.5×10^3			
$\text{Nu} = 0.621\text{Ra}^{1/5}$	40 - 8×10^3	(U)	Numerical	
$\text{Nu} = 0.524\text{Ra}^{1/5}$	40 - 8×10^3	(D)		

The trend is quite consistent across all correlations, as Ra decreases, Nu decreases. In the experimental data obtained by Suriano [49], Buznik [50], and Peinado [56], it becomes evident

Table 2.3: Literature correlations comparison in terms of Nusselt number as a function of Rayleigh numbers for horizontal plates double sided heated.

Correlation	Rayleigh range	Comment	Data source	Reference
$\mathrm{Nu} = 0.653\mathrm{Ra}^{1/7} + 0.922\mathrm{Ra}^{1/7}$	86 - 1.4×10^4	Double sided	Numerical	Chambers and Lee [53]
$\mathrm{Nu} = 0.367\mathrm{Ra}^{1/5} + 0.922\mathrm{Ra}^{1/7}$	1.4×10^4 - 9.1×10^5			
$\mathrm{Nu} = 0.608\mathrm{Ra}^{1/6} + 0.654\mathrm{Ra}^{1/6}$	9.1×10^5 - 1.6×10^8			
$\mathrm{Nu} = 4.3$	$< 1 \times 10^3$	Double sided	Numerical	Liu et al. [54]
$\mathrm{Nu} = 1.106\mathrm{Ra}^{0.214}$	1×10^3 - 1×10^7			
Experimental Data	86 - 1.4×10^3	Double sided	Experimental	Suriano [49]
Experimental Data	1×10^{-5} - 1×10^5	Double sided	Experimental	Peinado [56]
Experimental Data	86 - 1.4×10^3	Double sided	Experimental	Buznik [50]

that especially for $\mathrm{Ra} < 1$, Nu tends to stabilize at values close to $\mathrm{Nu} \approx 2$. In the range of $10 < \mathrm{Ra} < 3 \times 10^2$, Suriano [49], Buznik [50] and Liu [54] propose Nu values up to twice as high as those predicted by other correlations, which exhibit very similar values. For $\mathrm{Ra} > 1 \times 10^3$, the rate at which Nu increases varies depending on the specific correlation.

To emphasise the effect of correlation selection on the temperature of a heated plate, the different correlations are shown in Figure 2.7, in the case that the steady-state temperature of a horizontal heated plate is dissipating 0.8 W when exposed to air temperature at different altitudes, and then at different Rayleigh numbers (radiation and conduction heat transfer are not considered). The characteristic length of the plate is $L = 0.008$ m, and the heat transfer area is $A = 0.0025$ m^2 (double sided convection).

The difference between the correlations shows the great influence that the choice of correlation can have on the temperature obtained for the plate.

It is clear that some tests should be carried out in order to reduce the uncertainty in the modelling by using correlations for a horizontal heated plate exposed to natural convection. This point is covered in the next section.

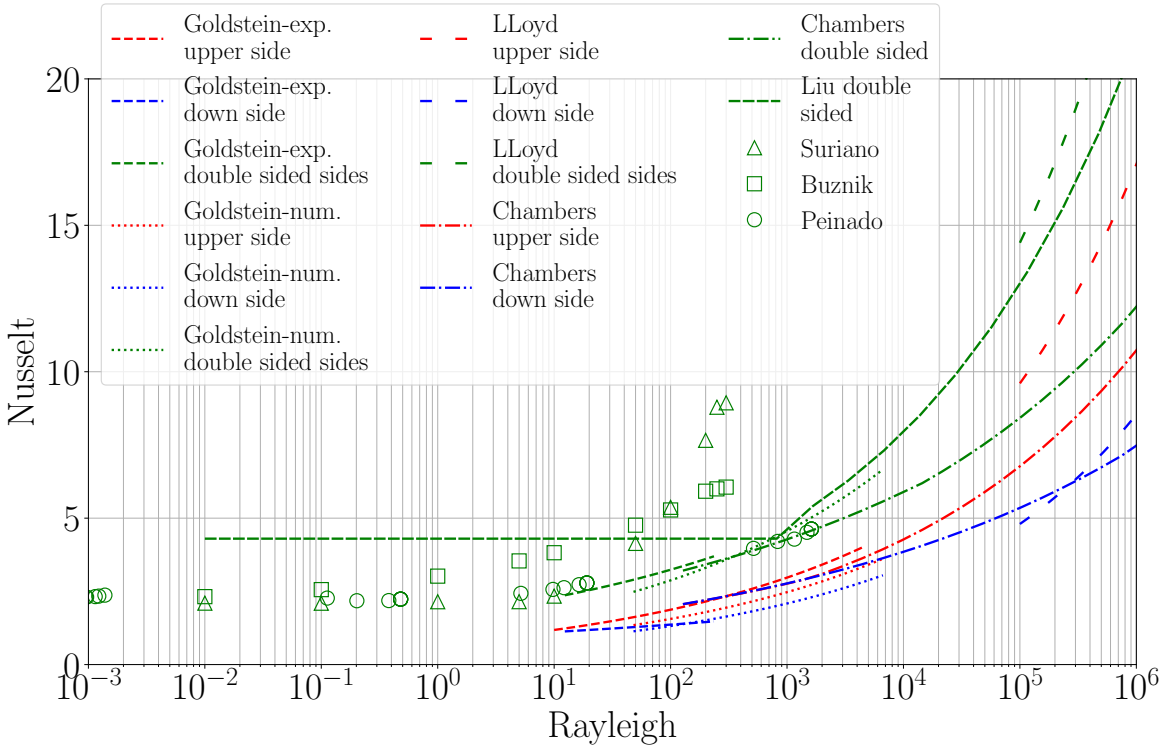

Figure 2.6: Literature correlations comparison in terms of Nusselt number variation as a function of Rayleigh number. Red color: upward facing heated plate (single sided convection) average Nusselt number correlation; blue color: downward facing heated plate (single sided convection) average Nusselt number correlation; green color: average Nusselt number correlation for the upper and lower surface (doubled sided convection). Numerical correlation: dotted-lines, correlation from Goldstein [51]; dashdotted-lines, Chambers [53]. Experimental correlation: dashed-lines, correlation from Goldstein [51]; loosely-dashed-lines, Lloyd [55]; densely-dashed-lines, Liu [54]. Experimental data: green-triangle-markers, data from Suriano [49]; square-green-markers, Buznik [50]; circle-green-markers, Peinado [56].

2.7 Experimental set-up and results

Due to the remarkable differences in the available literature for the case of a flat heated plate under the expected conditions of stratospheric flight, tests under different pressure and temperature conditions, i.e. different Ra, has been carried out to improve the modelling of convection in this type of problems.

The experimental set-up (see Figure 2.8) consists of a horizontal heated plate with dimensions 25 mm $\times$ 50 mm $\times$ 1 mm, placed in the middle of a 150 mm $\times$ 150 mm $\times$ 150 mm cavity, and assem-

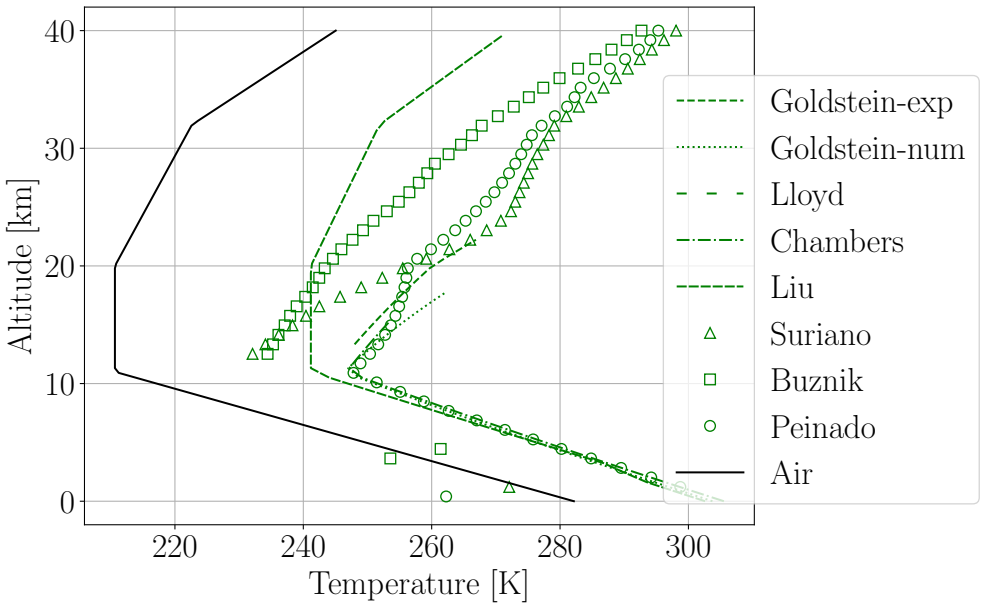

Figure 2.7: Comparison of the steady-state temperature vertical profiles of a horizontal plate of characteristic length $L = 0.008$ m, and heat transfer area $A = 0.0025$ m^2, dissipating 0.8 W, exposed to air at different altitudes (double sided convection), obtained on the basis of the different correlations available in the literature in the range of application of Ra. Numerical correlation: dotted-lines, correlation from Goldstein [51]; dashdotted-lines, Chambers [53]. Experimental correlation: dashed-lines, correlation from Goldstein [51]; loosely-dashed-lines, Lloyd [55]; densely-dashed-lines, Liu [54]. Experimental data: green-triangle-markers, data from Suriano [49]; square-green-markers, Buznik [50]; circle-green-markers, Peinado [56].

bled to the supporting tray through a Delrin support to minimize the conductive heat transfer. In addition, to minimize the thermal radiative couplings between the inner side of the closure panels in the cavity and the heated plate, both items were covered with aluminum tape 3M [57] (with IR emivissivity $\varepsilon = 0.03$).

The test was performed in the IDR/UPM TVAC facilities [58]. The characteristics of the chamber are listed below:

- Shroud and baseplate can be independently controlled.
- Baseplate dimension of 700 mm $\times$ 700 mm.
- Temperature range from -150 °C to 180 °C.
- Maximum changing rate: < 5 °C $\cdot$ min^{-1}.
- The pressure inside can be controlled.

The cavity walls, the heated plate, and the inner cavity air temperature were measured by using type-T thermocouples. Besides, the air temperature above the structure was also measured by type-T thermocuple covered by a SLI (Single Layer Insulation). The position of the temperature sensors are summarized in Table 2.4, and the experimental setup is shown in Figure 2.8.

Table 2.4: Temperature sensors location during the test.

TC #	Sensor location	Element
01	Baseplate close the DUT	BP
02	Centre of the heated plate	PL
03	Centre of the horizontal tray inner face	DUT
04	Centre of the upper cavity inner face $X-$	DUT
05	Centre of the upper cavity inner face $Y+$	DUT
06	Centre of the upper cavity inner face $Y-$	DUT
07	Air inside the cavity (corner)	Air
08	Centre of the upper cavity inner face $Z+$	DUT
09	Centre of the upper cavity inner face $X+$	DUT
10	Air inside the cavity (above the plate)	Air
11	Air outside the cavity (above the upper tray)	Air

The aim of the test was to determine the Nusselt number for each of the Ra to be tested. To do this, it is necessary to generate each one of the heat transfer mechanisms that occur on the plate, in order to obtain the convection heat transfer coefficient, h, and subsequently the Nusselt through its definition (see section 2.2). The steady-state energy balance of the heated plate is defined as:

$$0 = \dot{Q}_{cond} + \dot{Q}_{rad} + \dot{Q}_{conv} + \dot{Q}_{heat}, \tag{2.32}$$

where $\dot{Q}_{cond}$ is the conductive heat flow through the Delrin support, $\dot{Q}_{rad}$ is the radiative exchange between the heated plate and the surrounding walls, $\dot{Q}_{heat}$ is the power dissipation of the heated plate, and $\dot{Q}_{conv}$ is the convective exchange.

For the heated plate, the conductive exchange, $\dot{Q}_{cond}$, between the heated plate of the HTL and supporting tray through the Delrin support is obtained from:

$$\dot{Q}_{cond} = -G_{L_{del}} \left(T_p - T_s \right), \tag{2.33}$$

where T_p is the heated plate temperature, T_s is the supporting tray temperature, and $G_{L_{del}}$ is the thermal conductance through the Delrin.

The radiative exchange between the heated plate and the surrounding walls is computed by using:

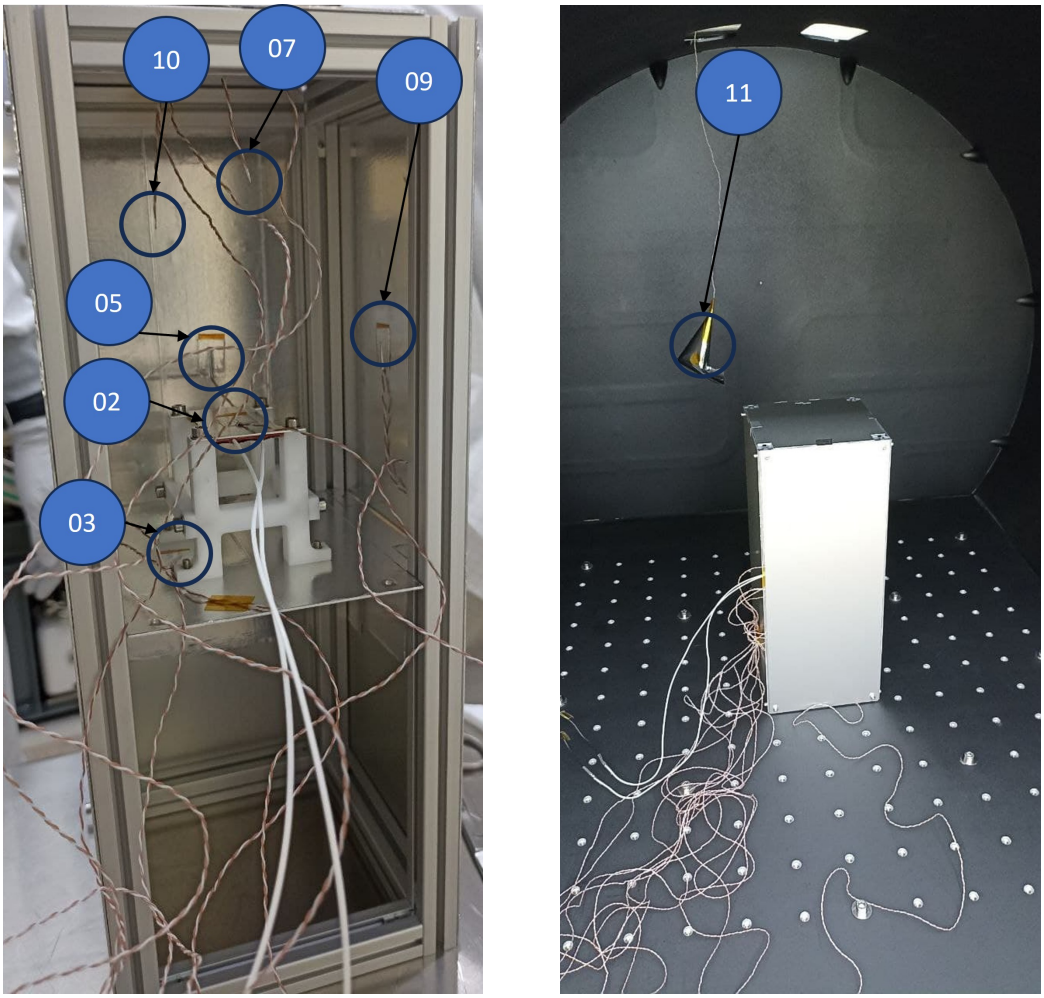

(a) Heated plate inside the cavity.

(b) Prototype inside the Thermal-Vacuum chamber.

Figure 2.8: Test set-up. (See marker keys in Table 2.4).

$$\dot{Q}_{rad} = \sum_{j=0}^{n} A_j \varepsilon_j \sigma T_j^4 B_{p,j} - A_p \varepsilon_p \sigma T_p^4, \tag{2.34}$$

where A_j, ε_j, and T_j are the area, the infrared emissivity and the temperature of the surrounding walls j, respectively. $B_{p,j}$ is the Gebhart Factor [59] from the heated plate to the wall j, σ is the Stefan-Boltzmann constant [59], and A_i, ε_i, and T_i are the area, the infrared emissivity and the temperature of the heated plate, respectively.

The convective exchange between the heated plate and surrounding air is computed by using:

$$\dot{Q}_{conv} = -hA_p(T_p - T_a). \tag{2.35}$$

The power dissipation of the heated plate is given by:

$$\dot{Q}_{heat} = VI, \tag{2.36}$$

where V and I are the voltage and the current of the heater, respectively.

Therefore, to obtain the convective heat transfer, the voltage and the current during the test are measured, and the thermal conductance through the Delrin, $G_{L_{del}}$, should be determined. To do so, a preliminary test was performed in vacuum conditions (to avoid the convection flow), setting the temperature of the baseplate (BP) and shroud (SHR) of the chamber to -30 °C, the stabilization criteria to 0.5 °C $\cdot$ h^{-1} for 2 hours, and the power dissipation of the plate to 1.25 W.

Then, to properly estimate the radiative exchange between the heated plate and the surrounding elements, a GMM and TMM of the cavity was built in ESATAN-TMS to determine the Gebhart factors. Finally, the closure panels of the cavity were set as boundary nodes with the temperature measured by the corresponding thermocouples, and the heated plate temperature was correlated with the measured one. The conductive coupling obtained is $G_{L_{del}} = 0.0124\,\mathrm{W \cdot K^{-1}}$, with an error of 0.5 °C in the heated plate temperature after the thermal correlation. The position of the thermocouples placed at the closure panels, and at the centre of the horizontal tray inner face, which are defined as boundary in the TMM to correlate the conductive coupling, $G_{L_{del}}$, and their temperature measurements, are summarized in Table 2.5.

Table 2.5: Temperature of the thermocouples at the closure panels, and at the centre of the horizontal tray inner face, defined as a boundary in the TMM.

ID	Location	TBT Temp. [°C]
03	Tray inner face (Z—)	−24.9
04	Closure panel (X—)	−30.6
05	Closure panel (Y+)	−28.6
06	Closure panel (Y—)	−27.5
08	Closure panel (Z+)	−27.3
09	Closure panel (X+)	−27.8

Once the conductive heat losses have been determined, the free convection heat transfer around the heated plate can be estimated. To do so, seven cases were carried out at different pressure levels, from 3 mbar to 750 mbar. Then, taking into account the conductive and radiative losses, a free convection correlation as a function of the Rayleigh number was obtained. The thermal

conditions of each test is summarized in Table 2.6, together with the conductive, radiative and convective heat flows obtained for each test, where the relevance of the free convection, not only at high pressure but also at low pressure in the test set-up can be observed. It has to be pointed out that the relevance of the free convection is strongly dependent on the assembly. In case the conductive heat transfer and/or the IR emissivity of the element increase, the magnitude of the free convection compared to the conductive and radiative heat transfer would become negligible at a low pressure, as it is shown in Table 2.6, the lower the pressure, the less relevant the convection. Then, if the ratio $\dot{Q}_{cond}/\dot{Q}_{heat}$ and $\dot{Q}_{rad}/\dot{Q}_{heat}$ increase by improving the conductive and radiative coupling respectively, the convection term will become lower.

Table 2.6: Thermal boundary conditions of the test performed (Cases 1 to 8) and comparison of the contribution of each heat transfer mechanism at steady-state conditions. $\dot{Q}_{heat}$ is the power dissipation of the plate, $\dot{Q}_{cond}$ is the conductive heat flow, $\dot{Q}_{rad}$ is the radiative heat flow, and $\dot{Q}_{conv}$ is the convective heat flow.

	Boundary conditions			Heat transfer mechanism comparison [%]		
ID	Pres. [mbar]	Power [W]	BP and SHR[1] Temp. [°C]	$\dot{Q}_{cond}/\dot{Q}_{heat}$	$\dot{Q}_{rad}/\dot{Q}_{heat}$	$\dot{Q}_{conv}/\dot{Q}_{heat}$
Case 1	3	1.25	−30	67.0	1.3	31.7
Case 2	3	1.25	−20	65.1	1.4	33.5
Case 3	20	1.25	−20	65.4	1.4	33.2
Case 4	20	1.25	−30	67.7	1.3	31.0
Case 5	20	0.6	−30	69.6	1.1	29.3
Case 6	300	1.25	−20	45.4	0.9	53.7
Case 7	750	1.25	−10	37.6	0.7	61.7
Case 8	1×10^{-7}	1.25	−30	97.2	2.8	0.0

[1] BP: Baseplate
SHR: Shroud

The temperature measurements of the thermocouples and the pressure during the test are shown in Figure 2.9.

To study the effect of possible mass transfer between the internal (hot) and external (cold) air, the same test was developed with the same cases as above described, but the top cover of the cavity was modified so that in this second test the top cover had four openings of 10 mm × 1 mm each.

The temperature measurements of the thermocouples and the pressure during the test with the open cover are shown in Figure 2.10.

The temperature measured by the thermocouple on the heated plate at the different pressure

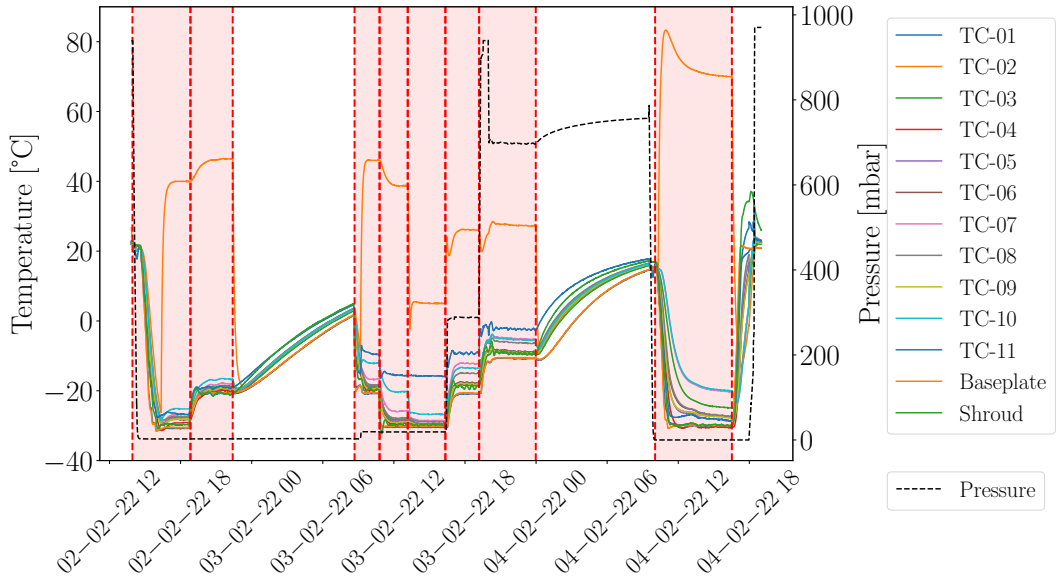

Figure 2.9: Overview of test temperature measurements (for closed cover configuration). Temperature measurements (solid lines) in the left y-axis, and pressure measurements (black dashed line) in the right y-axis. Vertical dashed lines: beginning and end of cases listed in Table 2.6, whose duration is highlighted in red (from left to right the highlighted cases go from Case 1 to Case 8).

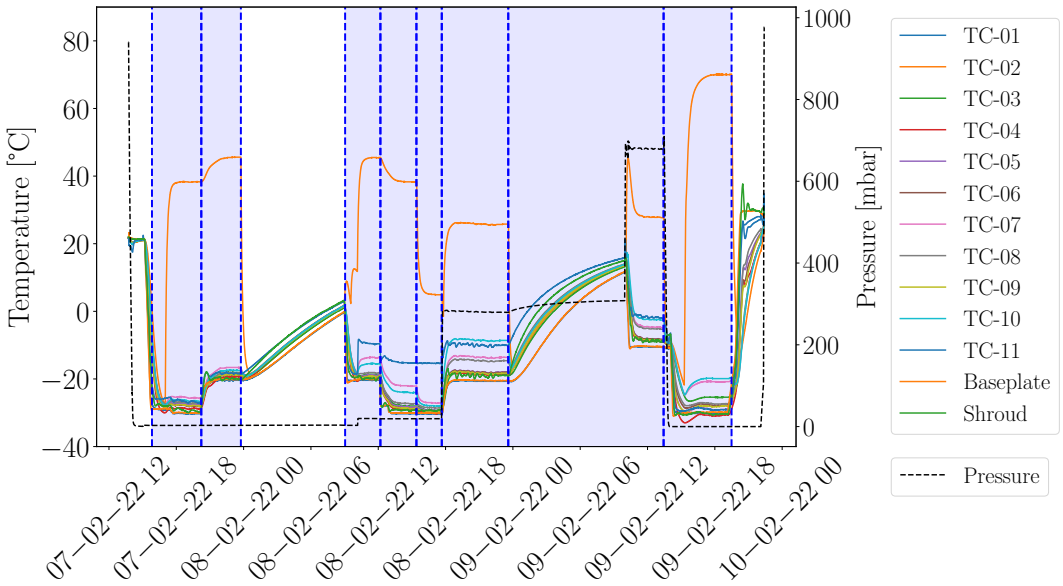

Figure 2.10: Open cover configuration (description as in Figure 2.9).

levels, comparing the closed cover scenario with the open cover scenario, is shown in Figure 2.11.

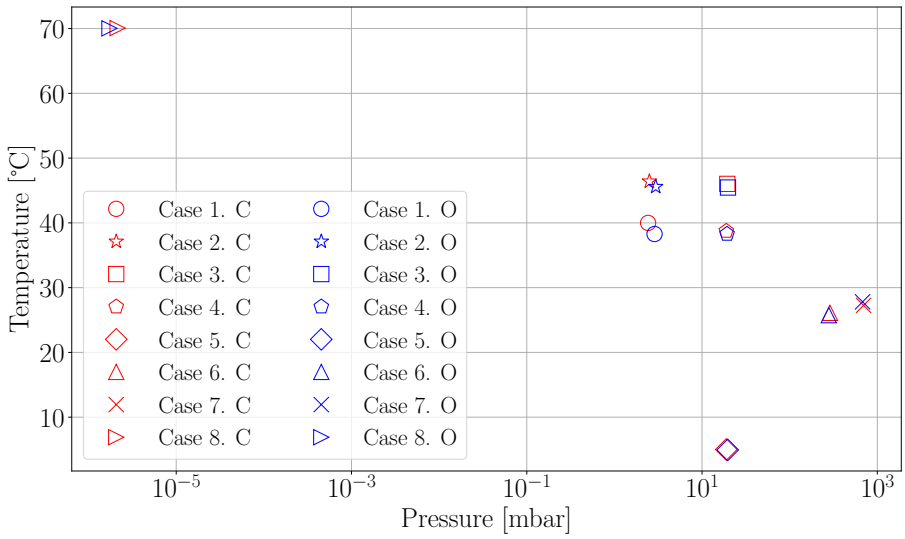

Figure 2.11: Measured heated plate temperature in both the closed cover (C) and the open cover (O) scenarios. Case explanation in Table 2.6 .

Two main conclusions can be obtained. First one, it can be shown that there is hardly any difference in the temperature measured in the two scenarios, so there has not been enough motion to generate mass transfer between the internal and external air through the apertures used. Second one, there is a difference of up to 20 °C when comparing the vacuum case (Case 8) with the expected float pressure (3 mbar), which shows the clear influence of the air on the plate temperature.

The temperature difference between the plate and air temperature (calculated as the average of thermocouples 07 and 10) between the scenarios closed and open cover is shown in Figure 2.12.

Again, there is little difference between the two scenarios considered, although there is a difference of a few degrees in the case of higher pressure.

In Figure 2.13, the plate temperature is plotted against the Ra number, obtained using the procedure described at the beginning of this chapter, again comparing the two scenarios. It is shown again that at high pressures (high Rayleigh), there is a slight influence between the two scenarios, with the plate temperature being lower.

In addition, in Figure 2.14, the obtained Nu number is plotted against the Rayleigh number for both scenarios. It is shown that at high Rayleigh (high pressures) the Nusselt number is slightly higher in the open cover scenario, which can be explained by a slight mass transfer between the

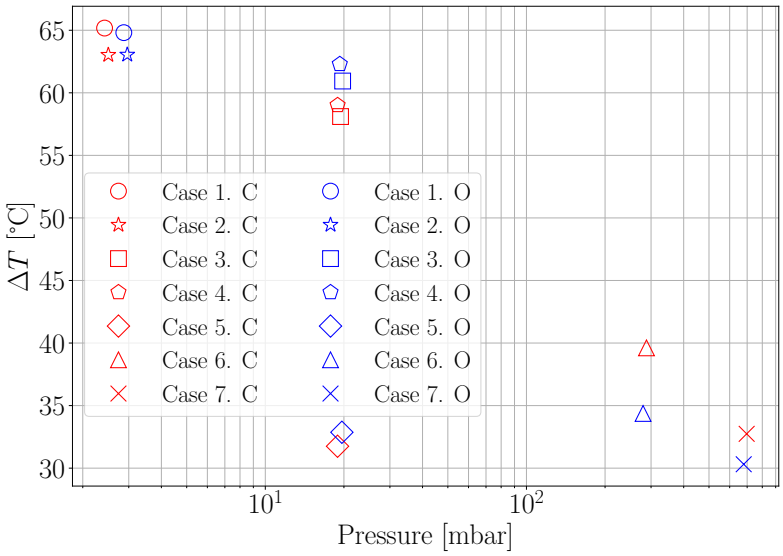

Figure 2.12: Measured temperature difference between the plate and the air in both the closed cover (C) and the open cover (O) scenarios at different pressure levels. Case explanation in Table 2.6.

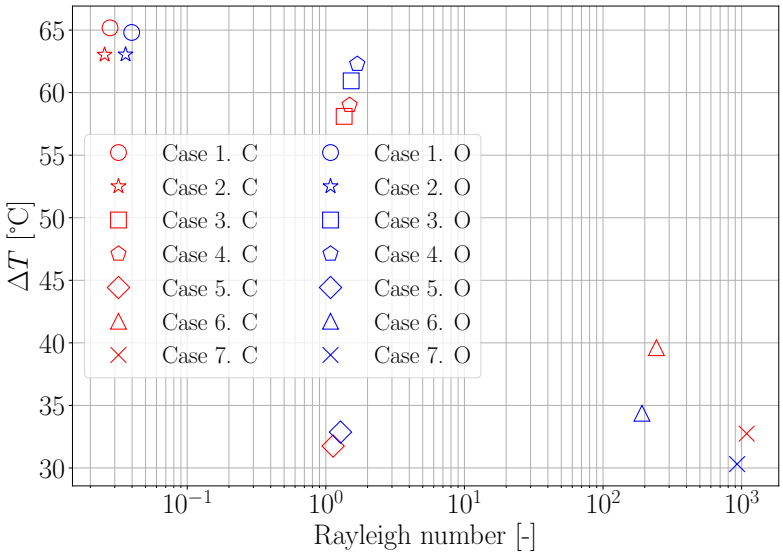

Figure 2.13: Measured temperature difference between the plate and the air in both the closed cover (C) and the open cover (O) scenarios at different Rayleigh numbers. Case explanation in Table 2.6.

internal and external air.

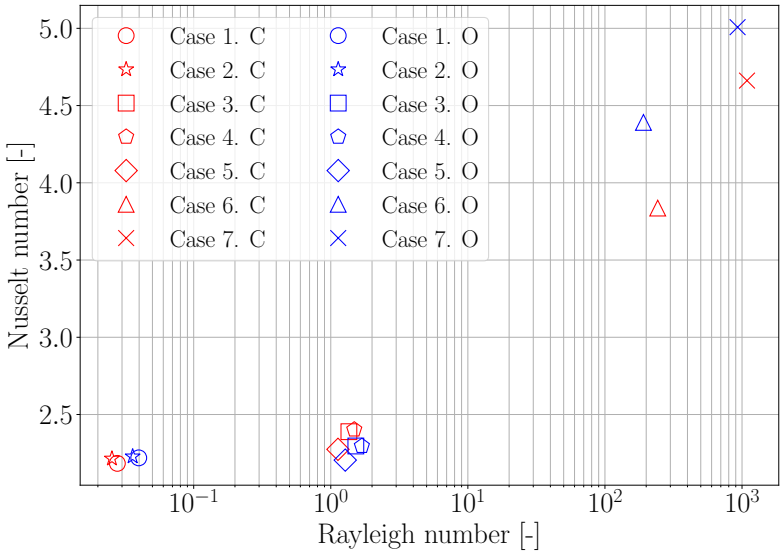

Figure 2.14: Nusselt number in both the closed cover (C) and the open cover (O) scenarios at different Rayleigh numbers. Case explanation in Table 2.6.

Finally, in Figure 2.15, the obtained convective heat transfer coefficient, h, is plotted against the Rayleigh number for both scenario, where, as expected, the trend observed is similar to that of the Nusselt number.

2.7.1 Results

The experimental results of the convection effects obtained are presented in Figure 2.16, where the variation of the Nusselt number as a function of the Rayleigh number is compared to the correlation published by other authors [39], [49], [50], [53], [54], [56]. An uncertainty lower than 20% taking into account all the variables involved is obtained, based on the methodology described in [60], for a generically function $y = f(x_1, x_2, ..., x_n)$:

$$\Delta y = \sqrt{\sum_{i=1}^{n} \left(\frac{\partial y}{\partial x} \Delta x_i \right)^2}, \tag{2.37}$$

where Δx_i is the uncertainty of variable x_i. Thus, by using (2.19) and (2.32)-(2.36):

$$\mathrm{Nu} = \frac{VI - G_{L_{del}}(T_p - T_s) - \sigma\varepsilon 2A(T_p^4 - T_w^4)}{A(T_p - T_a)} \frac{L}{k}, \tag{2.38}$$

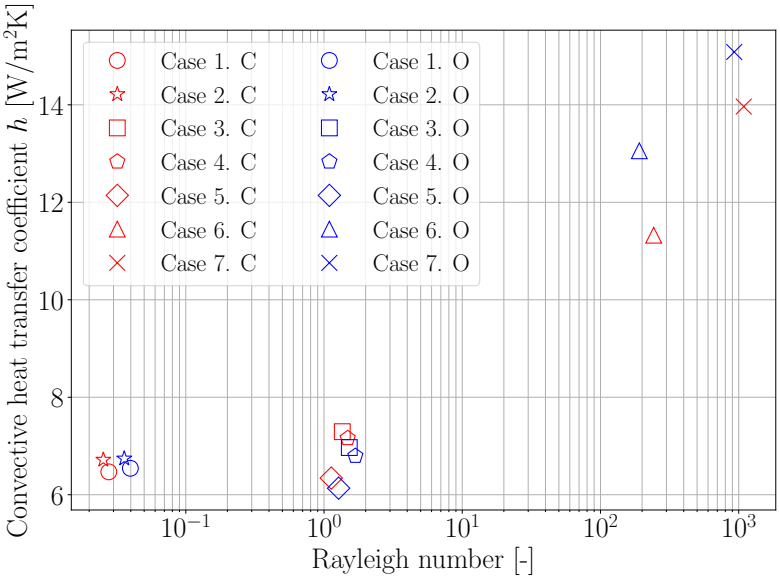

Figure 2.15: Convective heat transfer coefficient, h in both the closed cover (C) and the open cover (O) scenarios at different Rayleigh numbers. Case explanation in Table 2.6.

and taking into account the uncertainty of the parameters $I, V, T_a, T_p, T_w, \varepsilon$ and $G_{L_{del}}$:

$$\begin{aligned}\Delta \mathrm{Nu} = \Bigg\{ &\left[\left(\frac{\partial \mathrm{Nu}}{\partial V}\right)\Delta V\right]^2 + \left[\left(\frac{\partial \mathrm{Nu}}{\partial I}\right)\Delta I\right]^2 + \left[\left(\frac{\partial \mathrm{Nu}}{\partial T_a}\right)\Delta T\right]^2 \\ &+ \left[\left(\frac{\partial \mathrm{Nu}}{\partial T_p}\right)\Delta T\right]^2 + \left[\left(\frac{\partial \mathrm{Nu}}{\partial T_w}\right)\Delta T\right]^2 + \left[\left(\frac{\partial \mathrm{Nu}}{\partial \varepsilon}\right)\Delta \varepsilon\right]^2 \\ &+ \left[\left(\frac{\partial \mathrm{Nu}}{\partial G_{L_{del}}}\right)\Delta G_{L_{del}}\right]^2 \Bigg\}^{\frac{1}{2}}.\end{aligned}$$

The uncertainty associated to the measured parameters $I, V, T_a, T_p, T_w, \varepsilon$ and $G_{L_{del}}$ is summarized in Table 2.7

The experimental correlations available in the literature were obtained from experimental tests where the surrounding walls of the experiment were far enough to allow the complete evolution of the convective cell (external convection problem). However, in the case here presented, the surrounding walls are not far enough to fulfill this assumption. Then, a test setup adopted to our particular case has been developed.

In addition, as there is no continuity between different literature correlations along the expected Rayleigh range during the flight, the use of the convective correlation at Rayleigh values out of

Table 2.7: Parameters uncertainties.

Parameter	Uncertainty	Unit
I	0.001	A
V	0.001	V
T_a	1.0	K
T_p	1.0	K
T_w	1.0	K
ε	0.001	-
$G_{L_{del}}$	0.0005	$W \cdot K^{-1}$

the range established by the authors could provide wrong results. In fact, it is noticed that at low Rayleigh numbers (float phase) these correlations overestimate the free convection in this particular case. Slight differences in the Nusselt number may give rise to a considerable difference in the heated plate temperature, since at float phase (for a heated plate isolating conductively and radiatively) free convection has a significant contribution compared to conductive and radiative heat transfer mechanisms (see Case 1 and Case 2 in Table 2.6).

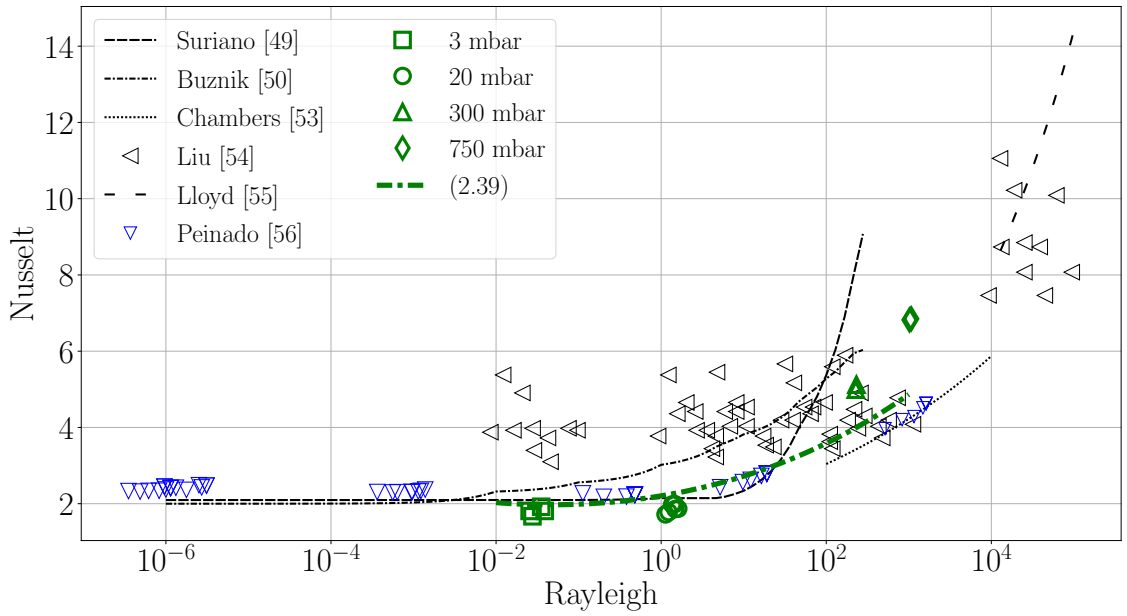

Figure 2.16: Nu vs Ra. Experimental results (green symbols); the correlation proposed (2.39) (thick dot-dashed green line); published results (see legend).

The trend of the Nusselt number with the Rayleigh number is clear: the greater the Rayleigh number, the greater the Nusselt number. Besides, for Ra $<$ 1, the Nusselt number seems to be almost constant (Nu $\approx$ 2). This fact means that, for Ra $<$ 1, the air conduction is as rel-

evant as the free convection. For $\mathrm{Ra} > 1$, the Nusselt number increases potentially. In order to define a unique correlation valid in the whole Rayleigh range expected for this type of platforms, a new correlation is proposed, based on the experimental data obtained from a range of $10^{-2} < \mathrm{Ra} < 10^{3}$ as follows,

$$\mathrm{Nu} = 2.207 \cdot \mathrm{Ra}^{-0.08363} + 2.92 \cdot (\mathrm{Ra}^{0.1169} - 1). \tag{2.39}$$

Note that for $\mathrm{Ra} < 10^{-2}$, the experimental results of [49] are very similar to the results obtained by [56].

Finally, the Nusselt number data obtained experimentally, Nu_{exp}, is plotted versus the Nusselt number predicted, Nu_{corr}, using the correlation proposed here (Equation 2.39), as it was done in [61] (see Figure 2.17). That is, for a given value of Rayleigh, the Nu_{exp} is known and the Nu_{corr} is computed using (2.39).

The diagonal of the plot (Figure 2.17) corresponds to the perfect correlation between the experimental and predicted values. A maximum relative error of 40% in the Nu_{exp} with the correlation is obtained as all the points are located inside the two shifted diagonals, which represent a relative error of $\pm 40\%$.

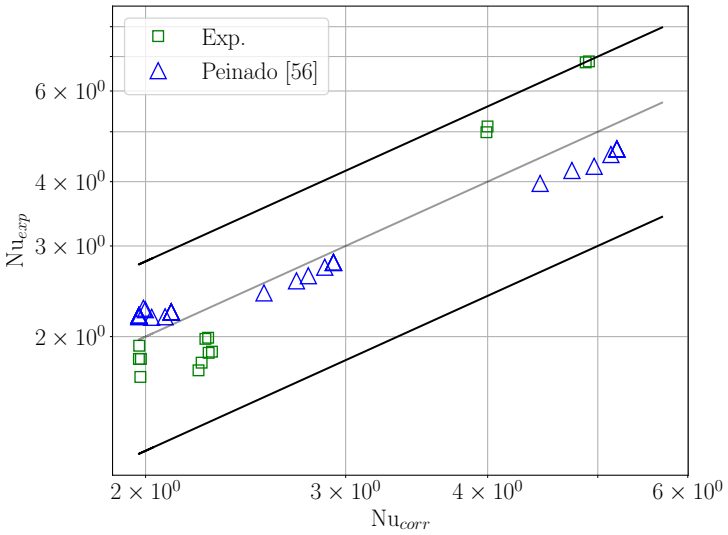

Figure 2.17: Comparison between experimental results, Nu_{exp} and the correlation Nu_{corr} (2.39). Experimental data: square, green symbol; data from [56]: triangle blue symbol ; solid line $\mathrm{Nu}_{exp} = \mathrm{Nu}_{corr}$; dashed line: diagonal 40% shifted from solid line.

Chapter 3. Ascent phase thermal analysis

The lift of a balloon-borne system is produced by the buoyancy force resulting from the difference in density between the surrounding air and the lifting gas (used to inflate the balloon), which compensates for the aerodynamic drag force and the balloon-borne system weight. The earliest stratospheric balloons used hydrogen as the lifting gas, but this was gradually replaced by helium [11], mainly for safety reasons. It is also important to consider the characteristics of the film used to provide the lifting force. Typically, scientific payloads are flown with zero-pressure or super-pressure balloons. While super-pressure balloons are completely sealed and can fly longer, zero-pressure balloons are vented at the bottom, and their flights are usually limited due to the gas losses [62] as previously described in section 1.2.

The ascent phase of stratospheric balloons typically lasts between 1-5 hours, depending on the float altitude. The ascent rate is strongly dependent on the characteristics of the system (i.e. the total mass, the float balloon volume, the thermo-optical properties of the balloon film, the temperature difference between the lifting gas and the free air). Typically, the ascent rate reaches values between 2-8 $m \cdot s^{-1}$ and it can be slightly controlled following two different strategies [62]. If the ascent rate is too high, the lifting gas can be valved to reduce the buoyancy force and, therefore, the ascent rate. When the ascent rate is too low, the system mass can be reduced, thus, both the net upward force and the ascent rate increase. To do so, ballast mass can be dropped during the ascent [19].

The float altitude typically varies from 18 km to nearly 40 km depending on the mission objective [19], [22], [63]. As for the balloon-borne horizontal motion, it is entirely dependent on the wind magnitude and direction, since stratospheric balloon missions relay the trajectory of the system on them. For instance, during the local summer period, the stratospheric winds at high latitudes are very stable from East to West direction allowing longer flights, such as those from

Kiruna to Alaska [19]. In contrast, some missions are limited by this fact, as the launch may be delayed due to the strong winds (for safety reasons), or the balloon may reach restricted areas, forcing an early cut-off [63]. Then, to predict the trajectory of a balloon-borne flight, not only at the float phase but also during the ascent phase, it is necessary to estimate magnitude and direction of the wind. Excursions in latitude and longitude around the launch site during the ascent phase are usually no greater than $\pm 1.5^{\circ}$ [16], as it is shown in Figure 3.1, where different profiles of altitude, longitude and latitude are compared during the ascent phase for different BEXUS balloon flights, all launched from Kiruna, Esrange (Sweden) [22].

The trajectories during the ascent phase for four LDB flights [19], [20], [64], [65] with a float altitude around 40 km are also compared in Figure 3.2.

The analysis and design of a payload onboard this type of platforms from a thermal point of view should consider all mission phases [16], [66], [67]. During the first stage of the ascent phase, convection is the heat transfer mechanism that leads the thermal behaviour (until the tropopause is exceeded) [12], due to the combination of the low air temperature and the relative velocity of the balloon-borne system to the wind. Thus, the information about the flight dynamics of the balloon can be very useful to perform the thermal analysis of stratospheric experiments (forced convection on the elements exposed to the outer air). Hence, the influence of different parameters in the ascent rate should be studied, as will have an impact in the thermal behaviour of the payload's exposed to the outer air. In addition, the horizontal relative wind speed should be also considered because sometimes, it may be of the same order of magnitude than the ascent rate [16].

Both the ascent rate and the horizontal relative wind speed during the ascent phase can be derived from an aerodynamic model [11] that combines the dynamics, the thermal behaviour of the lifting gas, and the geometrical variation of the balloon due to the air pressure variation throughout the altitude. Many researchers have developed dynamic models to predict the balloon flight trajectory [68] using analytical approaches based on global averaged values to define the thermal environment. The accuracy of the developed models (measured in terms of the ascent rate) widely varies between authors. For example, Palumbo et al. [69] improved their predictions by considering real-data of the air wind speed and the air temperature from different sources such as NOAA (National Oceanic and Atmospheric Administration) [70] and ECMWF (European Centre for Medium-Range Weather Forecasts) [71]. However, the radiative parameters are still defined based on global space averages. Nowadays, there are space missions focused on studying the Earth energy balance [72]–[74], whose data is then post-processed and included in open-access databases [75]. Therefore, by statistically analysing local data of the thermal environment, it is possible to obtain more reliable results of the ascent rate predictions, which allows a better thermal study. In this way, it is possible to obtain an envelope for the ascent rate values, which allows a robust

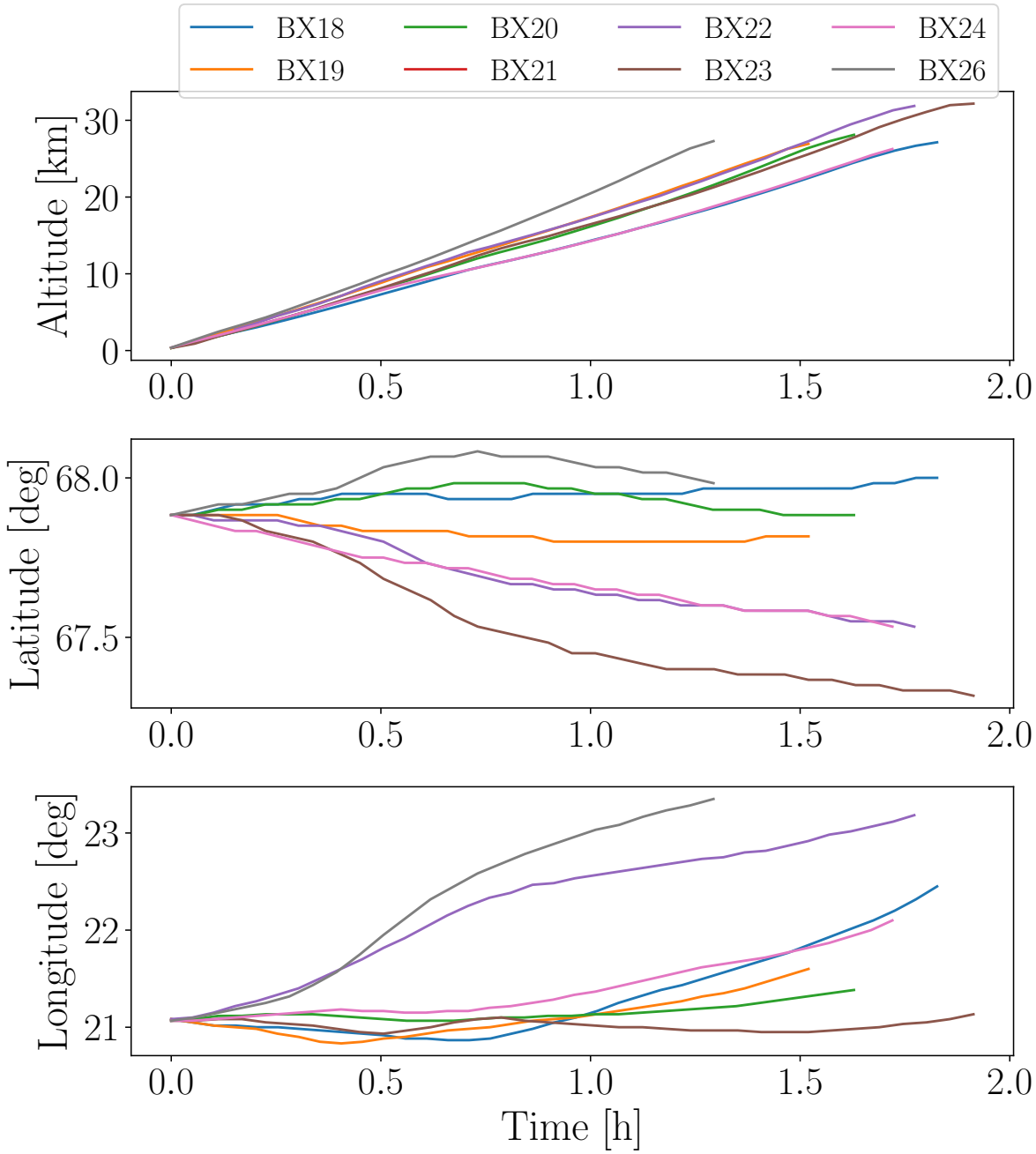

Figure 3.1: Latitude and longitude time profiles for different BEXUS flights during the ascent phase.

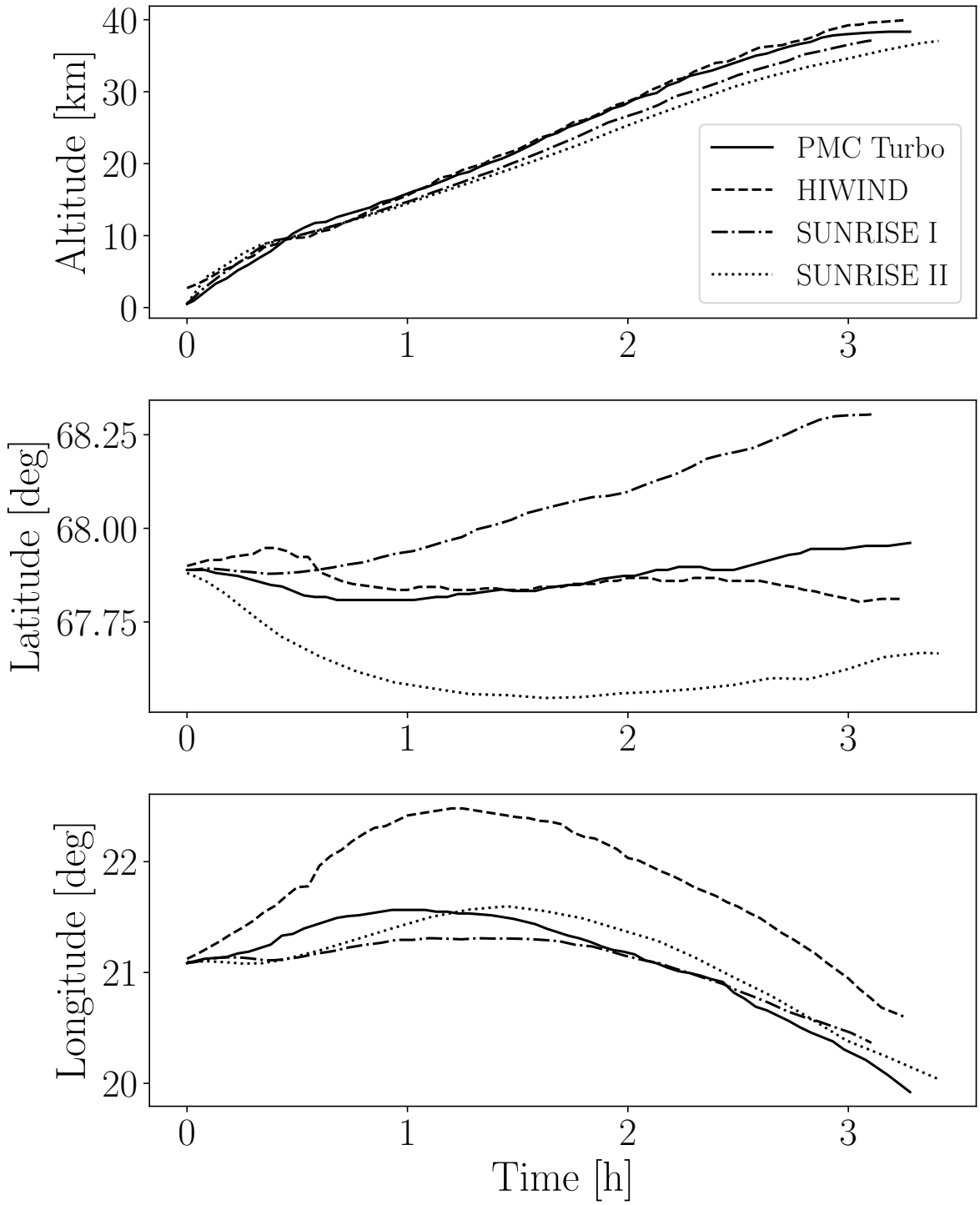

Figure 3.2: Altitude, latitude and longitude time profiles during the ascent phase of PMC-Turbo, HIWIND, SUNRISE I and SUNRISE II missions.

thermal design of the payload based on worst-case analyses.

In this work, a new methodology for developing ascent phase stratospheric balloon dynamics predictions for robust payload thermal design (based on a worst-case approach) has been carried out. The work presented here reduces the uncertainties of the thermal analysis of stratospheric payloads during the ascent phase by introducing the following innovative ideas:

- The variation of the parameters that define the radiative and convective thermal environment have been statistically treated from local databases.
- The influence on the ascent rate of the thermal environment parameters has been included to determine the thermal worst-case scenario.

The content of this chapter is organized as follows. First of all, the databases used to analyse the local data are presented in section 3.1. The payload analytical model used is presented in section 3.2, where the definition of the thermal environment during the ascent phase is described in subsection 3.2.1, and the governing equations to solve the thermal behaviour of a payload are shown in subsection 3.2.2. The characterization of the thermal environment for a particular scenario (in terms of launch site and launch time during the year) is described in section 3.3. Then, the equations that describe the dynamics of the balloon-borne are presented in section 3.4, and the validation of the tool developed to solve these equations summarized in section 3.5. A sensitivity analysis to determine the influence of each thermal environment parameter on the ascent rate is performed in section 3.6, and section 3.7. Finally, the thermal environment worst-case selection approach is presented in section 3.8, and applied to a particular case study in section 3.9.

3.1 Database description

3.1.1 CERES

The Clouds and the Earth's Radiant Energy System (CERES) [75] project provides data from observation of the entire Earth-atmosphere system radiation budget, obtained by using several instruments on multiple plarforms over two decades of observations [76]: CERES instruments flown on board the Terra (launched in 1999), Aqua (launched in 2002), Suomi–National Polar-Orbiting Partnership (launched in 2011) [77], and the latest CERES instrument (launched in 2017), on board the Joint Polar-Orbiting Satellite System 1 (JPSS-1) satellite, now called NOAA-20 [75].

In this work, the CERES Synoptic (SYN) 1 degree (SYN1deg) products, which provide parameters on a one-hourly temporal resolution and 1°-regional spatial scales, have been used. This product uses 1-hourly radiances and cloud property data from geostationary satellites combined with Terra and Aqua measurements [77]. Then, fluxes are provided in the longwave (LW), shortwave (SW), and window regions at four pressure levels (70, 200, 500 and 850 mbar)[75].

Data is retrieved in NETCDF4 [78] format directly from [79] under a request order, where the user must define the region window (in terms of latitude and longitude), the time range, and the parameters. The parameters used in this work are:

- Shortwave flux up (OLR).
- Shortwave flux down (sky IR radiation).
- Longwave flux up (albedo).
- Longwave flux down (solar direct radiation).

Once the request is approved, the user will received a NETCDF4 file, which has four dimensions (time, latitude, longitude and the parameter). Python tools have been developed in-house to read and treat all data provided.

3.1.2 ECMWF

The air temperature and the wind speed at different pressure levels have been obtained from ECMWF (European Centre for Medium-Range Weather Forecasts) data [80]. ECMWF is not

only a research institute but also a operational service to its Member States, producing numerical weather predictions (e.g. in Spain, AEMET (*Agencia Estatal de Meteorología*) uses ECMWF data). One of the most relevant dataset available at ECMWF is the ERA5 atmospheric reanalysis dataset [71]. This dataset is the latest ECMWF reanalysis archive observations, and is being produced by C3S (Copernicus Climate Change Service), as part of the Copernicus Earth Observation Programme [81], that is managed by the European Commission.

ERA5 data provides hourly regular latitude-longitude grids at $0.25° \times 0.25°$ resolution, with atmospheric parameters on 37 pressure levels. Data can be retrieved from [82], following the instructions summarized in [83]. Data is provided in NETCDF4 [78] format, where the user must define the region window (in terms of latitude and longitude), the time range, and the parameters (air temperature, and wind speed discretized in three directions, based on the North-East-Down (NED) system frame).

However, limitations with this dataset were found at the tropopause (where the air temperature trend changes), because the pressure levels grid were very limited at these altitudes (500, 300, 175, 70 mbar, or around 5.5, 9.0, 12.6, 18.0 km), as the air temperature trend has an impact on the ascent rate (see section 3.6). Then, the same dataset was required from ECMWF's MARS (Meteorological Archival and Retrieval System) catalogue [84]. Access to this data has been granted to the author by the licence holder requested. Then, data on 137 pressure levels, 3-hourly regular latitude-longitude grids at $0.25° \times 0.25°$ was retrieved [85]. Data was obtained in GRIB (General Regularly distributed Information in Binary form), a binary format [86], and then, split into surface and pressure levels. Then, data was converted to NETCDF4 format to use python tools (developed by the author) to read, assemble, and treat all data provided.

3.2 Payload thermal analytical model

3.2.1 Thermal environment definition

During the ascent phase, there is a change of the thermal environment with altitude due to the variation of the atmosphere composition. The parameters that must be considered to define the thermal environment during the ascent phase are shown in Figure 3.3. These parameters can be divided into radiative and convective parameters. Radiative parameters include direct solar radiation, albedo radiation, IR radiation from the sky, and IR radiation from the Earth. Ascent speed, wind speed, air density, and air temperature determine the convective heat transfer.

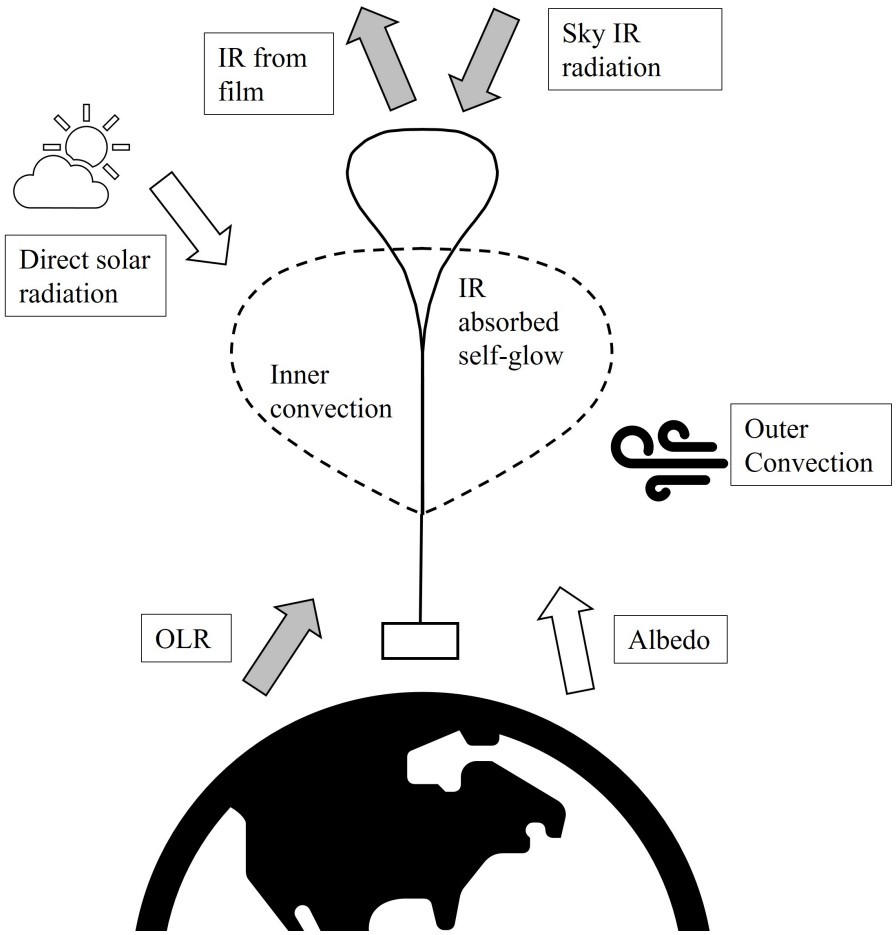

Figure 3.3: Parameters that affect the payload thermal environment (grey filled arrows: IR radiation; empty arrows: solar radiation).

Besides, not only the convective parameters but also the radiative parameters depends on both the season of the year and the launch site (e.g. at the polar regions (high latitudes), there are continuous light conditions during the local summer). There is also a dependence, especially on the radiative parameters, on the daytime through the Solar Zenith Angle (SZA) [87].

SZA is the angle between the vertical (perpendicular to the Earth's surface) and the line connecting the Sun and the payload, and it is complementary to the Sun Elevation Angle (SEA), as shown in Figure 3.4. SZA is primarily determined by the latitude and the time of day. It is largest in the morning and evening when the Sun is closer to the horizon, and it decreases as the Sun rises higher in the sky during the day. For locations closer to the equator, the Sun's path is more vertical, resulting in a lower SZA throughout the year. Conversely, at higher latitudes, such as near the poles, the Sun's path is more horizontal, leading to higher SZA.

Analytically, it can be estimated as follows [69]:

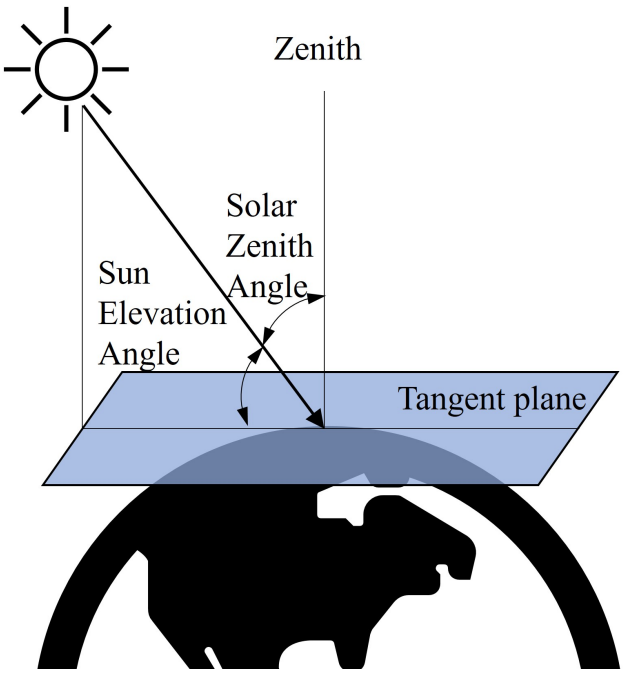

Figure 3.4: Solar Zenith Angle definition scheme.

$$\cos(\text{SZA}) = \sin(\lambda)\sin(\delta) + \cos(\lambda)\cos(\delta)\cos(\Omega), \tag{3.1}$$

where λ is the latitude, δ is the solar declination, and Ω is the Local Hour Angle (LHA), whose definition is presented in Figure 3.5.

3.2.1.1 Radiative parameters

As previously commented, during a typical ascent phase, there is a high variability with the altitude of the radiative thermal environment (solar irradiance, albedo coefficient, Outgoing Longwave Radiation (OLR) and the sky temperature) due to the atmospheric absorption. Moreover, this effect, together with the directionality effect of the thermal radiation, causes a SZA dependence of the radiative parameters, so that a parameterisation in terms of both, the altitude and the SZA, should be considered when characterising the thermal environment, except for the sky temperature, for which no relevant variations with the SZA have been observed. Then, raw data from CERES [75] is obtained based on a grid of altitude, longitude, altitude, and hour during the days of the launch window from previous years in order to obtain statistical profiles of every parameter. As an example, in the next subsubsections the particular thermal environment was studied for the BEXUS 32 mission, whose launch window in the earliest phases of the project was from 15$^{\text{th}}$ September to 15$^{\text{th}}$ October 2023 from Esrange, Kiruna, Sweden (N67°53′22″ E21°06′15″) with light con-

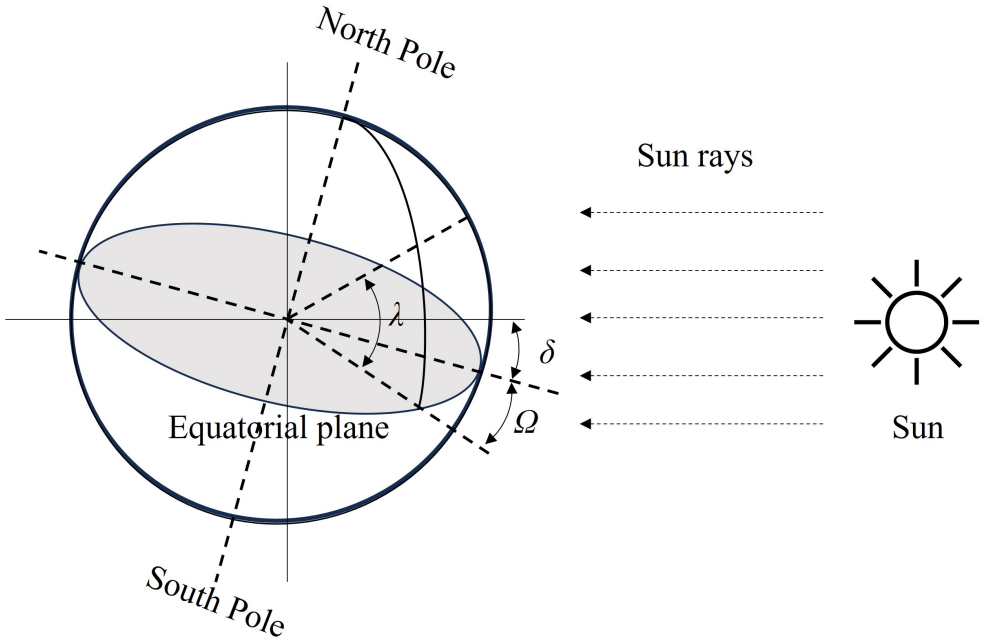

Figure 3.5: Latitude, solar declination and Local Hour Angle scheme. λ: latitude; δ: solar declination, and Ω: Local Hour Angle.

ditions. Then, the raw data from CERES were obtained with a grid in latitude of 66.5°-68° and in longitude of 21°-23° during the days from 15th September to 15th October of the years 2018 to 2020. The variation of the SZA along the daytime during the two months is represented in Figure 3.6.

Direct solar radiation Solar radiation is a significant factor in determining payload heat balance. Its magnitude is influenced by multiple factors, including the Solar Zenith Angle, and thus varies with the time of day. Additionally, solar radiation is affected by the altitude, as the reflection and absorption of solar radiation by the atmosphere change with the altitude. In addition, in a given region, there is a seasonal variation throughout the year due to the relative position of the Earth with the Sun along the Earth orbit. The variation of the solar irradiance at different altitudes along the SZA is shown in Figure 3.7. The dependence on the SZA at each altitude, and the variability of solar irradiance especially at low altitudes, is clearly visible.

Albedo The albedo is the fraction of the solar radiation that is reflected by the planet surface or by the planet atmosphere. Therefore, the albedo radiation is strongly dependent on the launch site because it will be different if the surface is covered by snow (high albedo), or the surfaces is darker (low albedo). In addition, there is a dependence on the SZA. The variation of the albedo

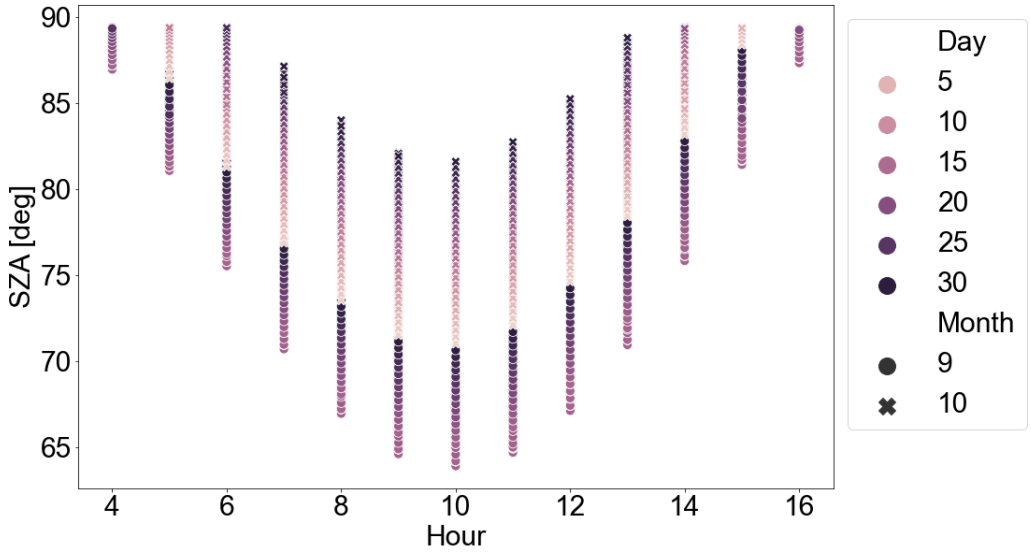

Figure 3.6: Variation of the SZA with the launch hour, during the launch window, for BEXUS 32 mission. Shape indicates month (9 or 10) and color the day of the month, according to the legend.

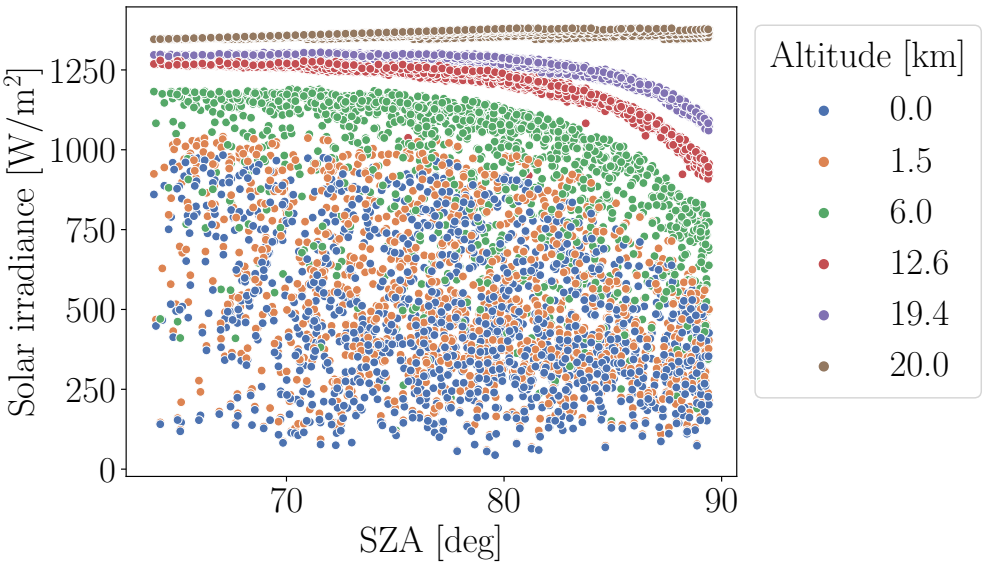

Figure 3.7: Variation of the solar irradiance as a function of the SZA, during the launch window for BEXUS 32 mission at $\lambda = 66.5°$, $\phi = 21.5°$, at different altitudes [75].

coefficient at different altitudes along the SZA is shown in Figure 3.8, where the variability of albedo coefficient with both the altitude and the SZA is clearly shown.

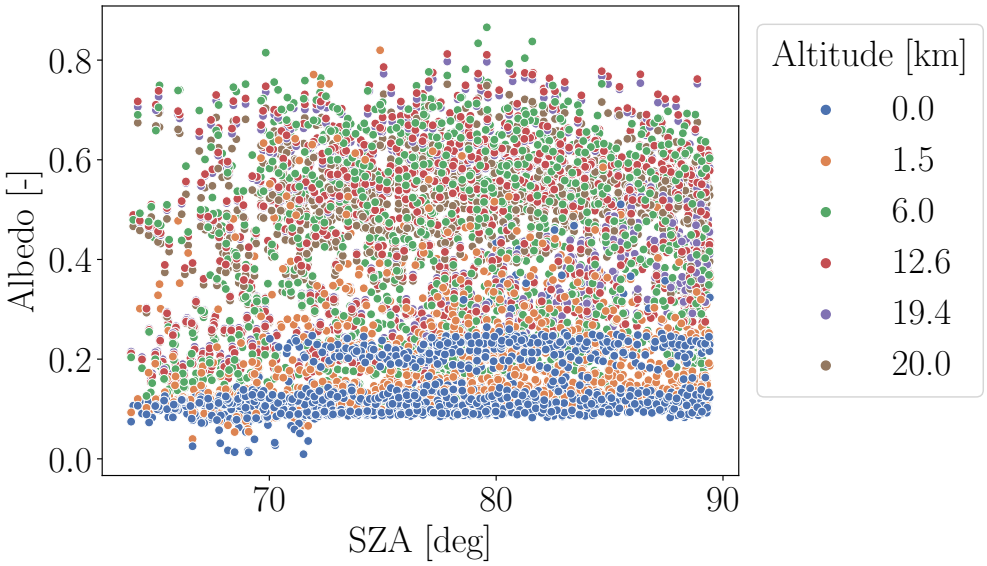

Figure 3.8: Variation of the albedo coefficient as a function of the SZA, during the launch window for BEXUS 32 mission at $\lambda = 66.5°$, $\phi = 21.5°$, at different altitudes [75].

Earth IR radiation It refers to the infrared radiation emitted by the Earth's surface and atmosphere back into space. There is a dependence on both the altitude, and on the SZA.

The variation of the OLR at different altitudes as a function of the SZA is shown in Figure 3.9. The influence of the altitude on the OLR is clearly shown, the lower the altitude, the higher the OLR. In addition, this parameter shows a dependence with the albedo.

Sky IR radiation The Earth's atmosphere contains various gases with the ability to absorb and emit infrared radiation. Sky IR radiation specifically refers to the portion of infrared radiation emitted by the atmosphere itself. Then, there is a dependent on the altitude due to the variation of the atmosphere composition. At space, the equivalent sky temperature (or deep space temperature) is around 3 K.

The variation of the sky temperature at different altitudes as a function of the SZA is represented in Figure 3.10, where it is well shown that the SZA has not a relevant impact on this parameter.

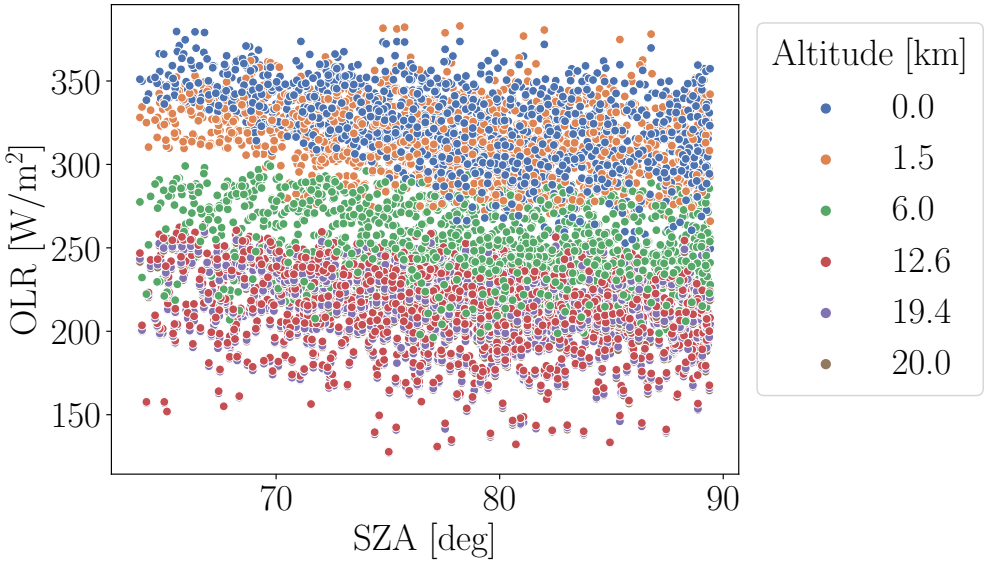

Figure 3.9: Variation of the OLR as a function of the SZA, during the launch window for BEXUS 32 mission at $\lambda = 66.5°$, $\phi = 21.5°$, at different altitudes [75].

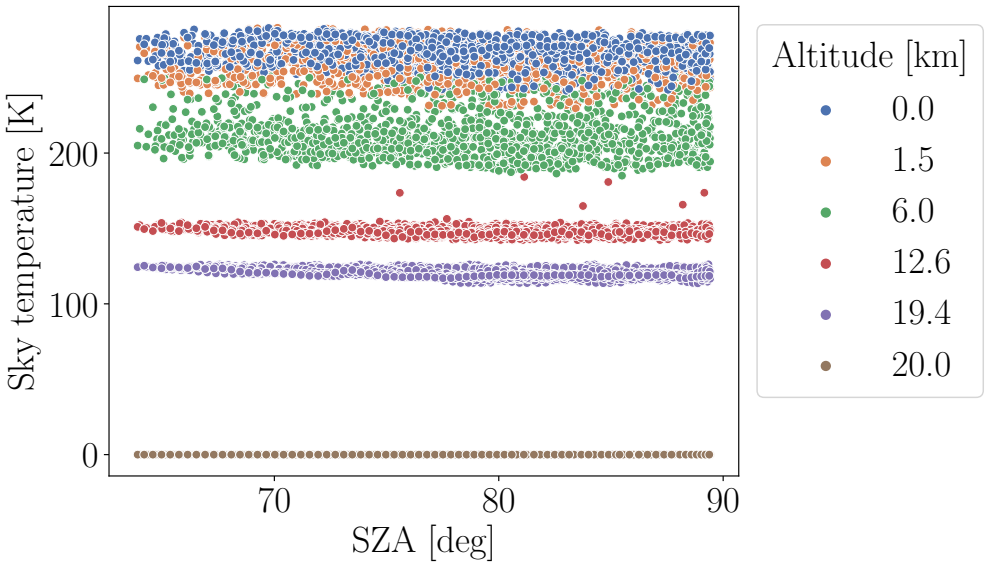

Figure 3.10: Variation of the T_{sky} as a function of the SZA, during the launch window for BEXUS 32 mission at $\lambda = 66.5°$, $\phi = 21.5°$, at different altitudes [75].

3.2.1.2 Convective parameters

The air temperature and the air pressure (and, therefore, the air density), as well as the ascent rate and the horizontal relative speed with the wind are denoted as the convective parameters, which are obtained as follows. The air temperature data has been obtained from the ECMWF database [71], where local temperature data is available at different pressure levels for a grid in latitude and longitude, and the pressure levels can be converted into altitude following [88]. Regarding the ascent rate, a geometrical-thermal-dynamic model should be used to predict the evolution in this phase, considering the evolution of the radiative and convective parameters (the whole process description is detailed in section 3.4).

Air temperature Air temperature changes with altitude and not always monotonously. In the troposphere, air temperature decreases with altitude, while at the tropopause, the normal behaviour of air temperature is to remain constant. Once the stratosphere is reached, air temperature rises. These changes shall be evaluated to estimate the convective effects, as the cooler the air temperature, the stronger the convection mechanism. The variation of the air temperature at daytime as a function of the altitude is represented in Figure 3.11.

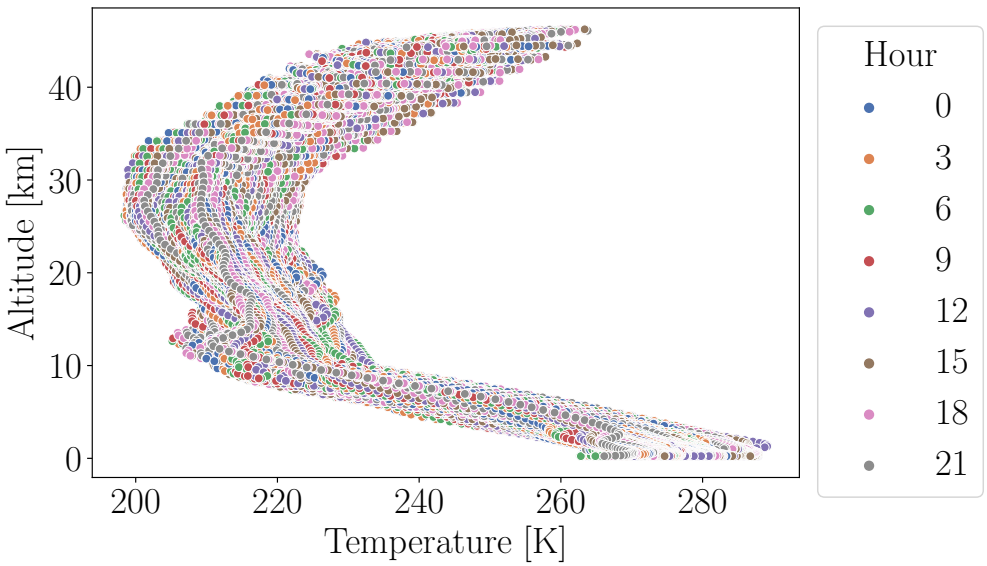

Figure 3.11: Variation of air temperature as a function of altitude, during the launch window for BEXUS 32 mission at $\lambda = 66.5°$, $\phi = 21.5°$, at different daytime hours [71].

Air pressure Air pressure decreases with altitude. This reduction together with that of the air density (that can be obtained from the air temperature and the air pressure based on the ideal gas assumption) leads to the decrease of the convection cooling, especially once the stratosphere has been reached. The variation of the air pressure at daytime as a function of the altitude is represented in Figure 3.12.

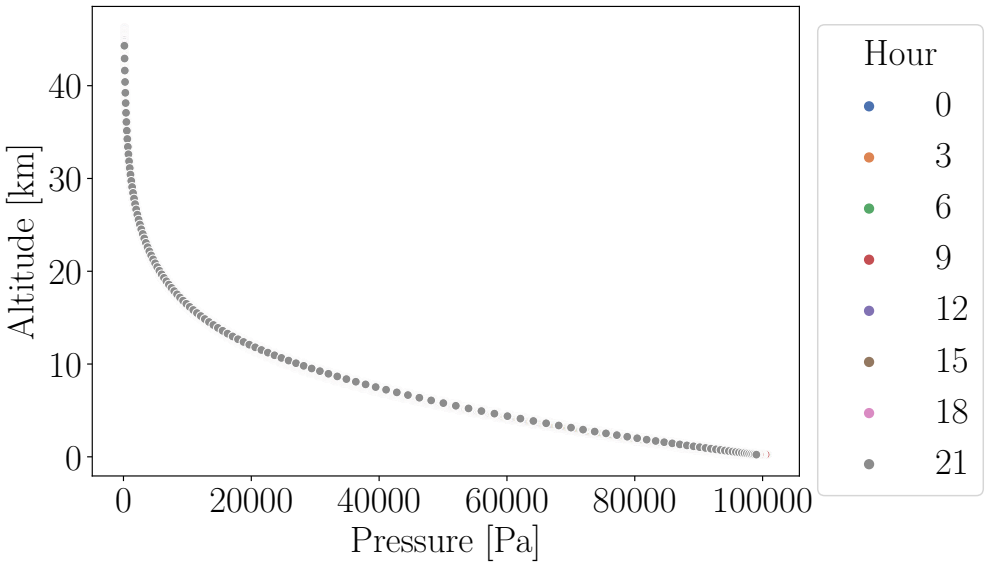

Figure 3.12: Variation of the atmospheric pressure, p_A, as a function of altitude, during the launch window for BEXUS 32 mission at $\lambda = 66.5°$, $\phi = 21.5°$, at different daytime hours [71].

Relative wind speed The horizontal relative wind speed and the vertical ascent rate should be obtained from an aerodynamic model that combines the variation of the thermal environment, the geometry of the balloon (due to the reduction of the air pressure), and the dynamics of the motion (see section 3.4). The variation of the air wind speed magnitude at daytime as a function of the altitude is shown in Figure 3.13, where the jet streams at the tropopause (around 11 km) can be observed. The combination of high wind speed (relative wind speed is examined in section 3.4) and low air temperature at these altitudes makes this region potentially the coldest of the entire mission.

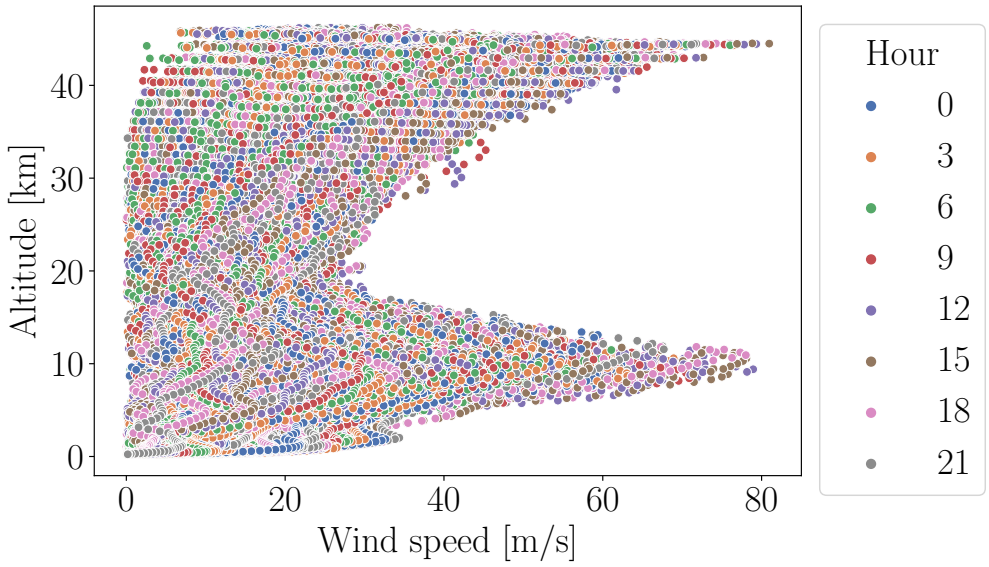

Figure 3.13: Variation of the air speed magnitude as a function of altitude, during the launch window for BEXUS 32 mission at $\lambda = 66.5°$, $\phi = 21.5°$, at different daytime hours [71].

3.2.2 Governing equations

The temperature behaviour of a payload during the ascent phase can be obtained using the energy thermal balance equation [12]:

$$m_i c_i \frac{\mathrm{d}T_i}{\mathrm{d}t} = \dot{Q}_{cond,i} + \dot{Q}_{rad,i} + \dot{Q}_{conv,i} + \dot{Q}_{\text{load},i} + \dot{Q}_{\text{heat},i}, \tag{3.2}$$

where the product $m_i c_i$ represents the heat capacity of the node i, and $\dot{Q}_{\text{heat},i}$ stands for the power dissipation of the node i. The conductive exchange, $\dot{Q}_{cond,i}$, the radiative exchange, $\dot{Q}_{rad,i}$, the convective exchange $\dot{Q}_{conv,i}$, the internal heat, $\dot{Q}_{\text{heat},i}$, and the environment heat load $\dot{Q}_{\text{load},i}$ (the solar, the albedo, the infrared from the sky and the planetary heat load) are defined in the following paragraphs.

3.2.2.1 Conductive heat flow from node i to other elements

According to [38], the conductive heat flow between a node i and the surrounding elements is computed as follows:

$$\dot{Q}_{cond,i} = -\sum_{j=1}^{n} G_{L,ij} \left(T_i - T_j\right), \tag{3.3}$$

where $G_{L,ij}$ is the linear conductor between the node i and node j. This parameter takes into account the material (thermal conductivity), the geometry (cross section of the heat path) and the length. Then, from the node i considered, the conductive heat flow from node i to j will outcome if the temperature T_i is greater than T_j or vice-versa.

3.2.2.2 Convective heat flow from node i to other elements

As the conductive heat flow, the convective heat flow is modelled linearly with the temperature difference of the node i and the surrounding air [30]:

$$\dot{Q}_{conv,i} = -h_L A_i \left(T_i - T_a\right), \tag{3.4}$$

where h_L is the average convective heat transfer coefficient on A_i. This coefficient depends on the particular problem analysed by means on the geometry (surface, roughness, flatness), relative speed with the air, the material (thermal conductivity), as has been presented in chapter 2. As the conductive heat flow, the convective heat flow from node i to the surrounding air will outcome if the temperature T_i is greater than T_a.

3.2.2.3 Radiative heat flow from node i to other elements

The radiative exchange between the node i and the surrounding elements is computed as follows [59]:

$$\dot{Q}_{rad,i} = \sum_{j=1}^{n} A_j \varepsilon_j \sigma T_j^4 B_{j,i} - A_i \varepsilon_i \sigma T_i^4, \tag{3.5}$$

where A_j, ε_j, and T_j are the area, the infrared emissivity and the temperature of the surrounding elements, node j, respectively. σ is the Stefan-Boltzmann constant [59], and A_i, ε_i, and T_i are the area, the infrared emissivity and the temperature of the node i, respectively. The term $B_{j,i}$, called Gebhart Factor [89], is the fraction of energy emitted by A_j that reaches A_i and is absorbed. For opaque, grey surfaces, with constant surface emissivity and absorptivity, it is computed as follows [89]:

$$B_{j,i} = F_{j,i}\varepsilon_i + \sum_{k=1}^{n} F_{j,i} \left(1 - \varepsilon_k\right) B_{k,j}, \tag{3.6}$$

where $F_{j,i}$ is the view factor between faces j and i. The Gebhart factor, as the view factor between faces i and j, satisfies the reciprocity relationship [59]:

$$\varepsilon_i A_i B_{i,j} = \varepsilon_j A_j B_{j,i}, \tag{3.7}$$

and then (3.5) can be rewritten as:

$$\dot{Q}_{rad,i} = -A_i \varepsilon_i \sum_{j=1}^{n} B_{i,j} \sigma \left(T_i^4 - T_j^4 \right), \tag{3.8}$$

3.2.2.4 Environmental heat loads

The term $\dot{Q}_{\text{load},i}$ represents the sum of the solar direct radiation, $\dot{Q}_{S,i}$, the solar radiation reflected by the Earth (albedo), $\dot{Q}_{A,i}$, the infrared radiation emitted by the Earth, $\dot{Q}_{E,i}$, and the infrared radiation emitted by the sky, $\dot{Q}_{sky,i}$, absorbed by the thermal node:

$$\dot{Q}_{\text{load},i} = \dot{Q}_{S,i} + \dot{Q}_{A,i} + \dot{Q}_{E,i} + \dot{Q}_{sky,i}. \tag{3.9}$$

The direct solar radiation absorbed by the node i, $\dot{Q}_{S,i}$, is determined from:

$$\dot{Q}_{S,i} = \alpha_i G_s A_i \cos(\theta_s) + \Gamma_{S_{j,i}}, \quad -\frac{\pi}{2} < \theta_s < \frac{\pi}{2} \tag{3.10}$$

where G_s is the solar irradiance, θ_s is the Sun Elevation Angle (if $\cos\theta_s < 0$, no solar radiation reaches the face A_i, and then the first term is null). The second term, $\Gamma_{S_{j,i}}$, represents the direct solar radiation reflections on the surroundings elements j which reaches the face A_i.

The solar albedo radiation absorbed by the node i, $\dot{Q}_{A,i}$, is as follows [12]:

$$\dot{Q}_{A,i} = \alpha_i a G_s A_i F_{i,E} \sin(0.9\theta_s)^{3/2} + \Gamma_{A_{j,i}}, \tag{3.11}$$

where a is the albedo coefficient, $F_{i,E}$ is the view factor of A_i with regard to the Earth, which decreases with the altitude. The second term $\Gamma_{A_{j,i}}$ refers to the albedo radiation reflected by the surrounding elements j, which reaches the face A_i.

The infrared radiation emitted from the Earth absorbed by the face A_i, $\dot{Q}_{E,i}$, is given by:

$$\dot{Q}_{E,i} = \varepsilon_i A_i F_{i,E} \sigma T_E^4 + \Gamma_{E_{j,i}}, \tag{3.12}$$

where the product σT_E^4 is the OLR (modelled as a blackbody), or $\dot{q}_E$, and the second term refers to the Earth infrared radiation reflected by the surrounding elements j, which reaches the face A_i.

The infrared radiation coming from the sky absorbed by the face A_i, $\dot{Q}_{sky,i}$, is given by:

$$\dot{Q}_{sky,i} = \varepsilon A_i F_{i,sky} \sigma T_{sky}^4 + \Gamma_{sky_{j,i}}, \tag{3.13}$$

where the product T_{sky} is the sky equivalent temperature, and then the product σT_{sky}^4 is the $\dot{q}_{sky}$, and the second term refers to the sky infrared radiation reflected by the surrounding elements j, which reaches the face A_i.

3.3 Thermal environment characterisation

Once all the parameters related to the thermal environment required for analysing a balloon-borne experiment from a thermal point of view have been presented, and the variation of most of them with the altitude and the SZA has been explained, statistical techniques can be used to capture the variability of these parameters, and then, to define representative profiles with both variables to characterise the thermal environment. In the following subsections, the heatmaps obtained are applied to the BEXUS 32 mission launch window, as an example.

3.3.1 Radiative parameters

The approach followed for the radiative parameters is first to group the SZA for each of the altitudes, from the minimum value to the maximum value that will occur along the launch window, and a grid is defined of the data in altitude and SZA. Then, in each of the elements of this grid, the data of the variable to be analysed are processed, computing the 10^{th} and 90^{th} percentiles to define the potential worst hot and cold thermal environments.

3.3.1.1 Direct solar radiation

The 90^{th} and 10^{th} percentiles for the solar irradiance at each element of the mesh defined in altitude and SZA are shown in Figure 3.14.

3.3.1.2 Outgoing Longwave Radiation and Albedo coefficient

OLR and albedo should be analysed together as there is a relationship between them (the higher the OLR, the lower the albedo and vice-versa [90]). Therefore, to obtain the worst combination, the

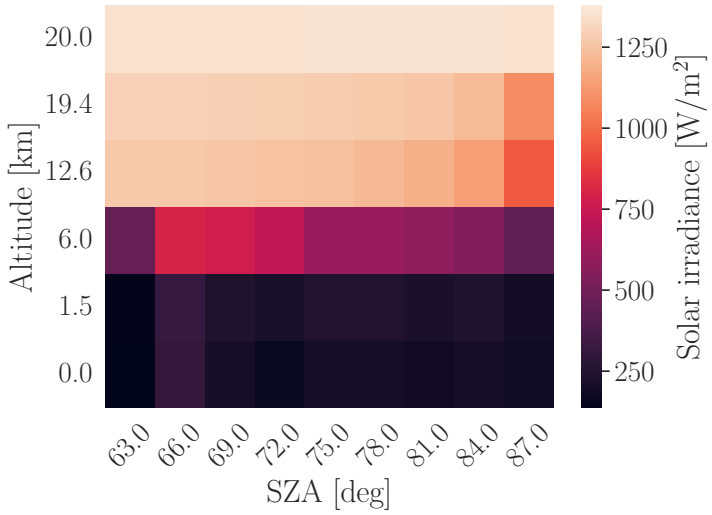

(a)

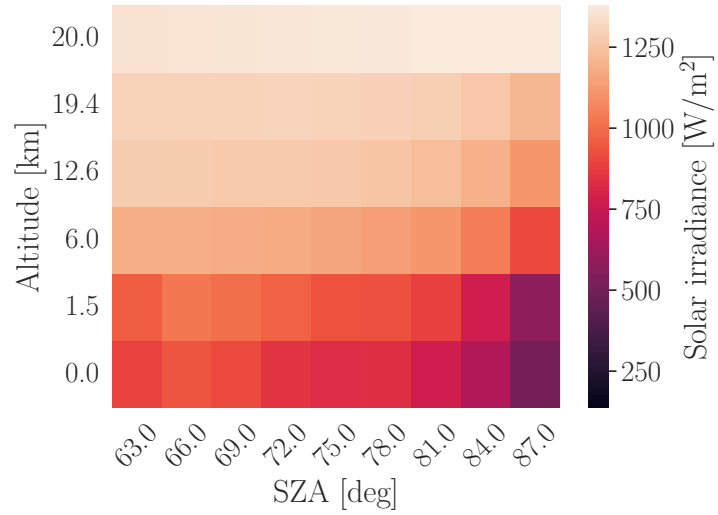

(b)

Figure 3.14: Comparison of the solar irradiance percentiles 10^{th} (a), and 90^{th} (b), at each altitude and SZA cell during the launch window for BEXUS 32 mission at $\lambda = 66.5°, \phi = 21.5°$ [75].

thermo-optical properties of the analysed payload should be taken into account, since the worst combination will be affected by the ratio absorptance/emittance (α/ε) of the surface (i.e a black surface will absorbs more albedo radiation than a white surface as its α is greater). Then, based on the ratio (α/ε), the worst-case OLR-albedo pair scenario is influence by either the extreme OLR values, the extreme albedo values, or a combination of both. Given this consideration, three distinct approaches can be employed to identify the most critical OLR-albedo pair combination. The variations among these approaches are the statistical methodologies applied to determine the OLR-albedo pair:

- Approach 1. For the albedo coefficient data, obtain a certain percentile, and the associated average value for the OLR (of the subset of that albedo percentile data). This approach may be the most suitable for white painted surfaces.
- Approach 2. For the OLR data, obtain a certain percentile, and the associated average value for the albedo coefficient (of the subset of that OLR percentile data). This approach may be the most suitable for black painted surfaces.
- Approach 3. Normalize the OLR-albedo pair distribution (Equal normalized variate, following $X_N = \frac{X-\mu}{\sigma}$), and obtain a certain percentile. This approach may be the most suitable for surfaces with intermediate (α/ε) ratio values.

To ease the understanding of the statistical methodologies, the representative OLR-albedo pairs at percentile 10^{th}, and 90^{th}, of each approach are shown in Figure 3.15.

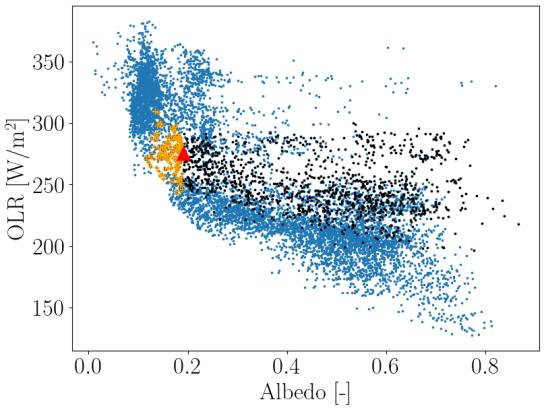

(a) Percentile 10th for the approach 1.

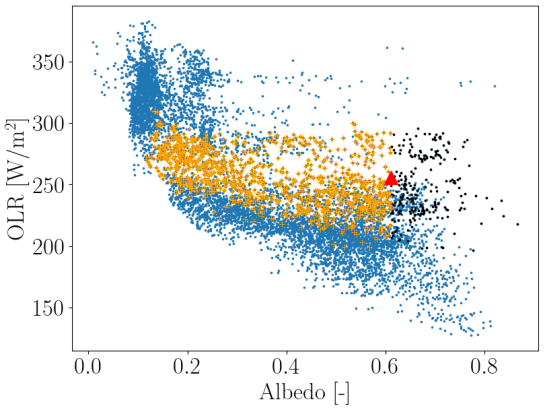

(b) Percentile 90th for the approach 1.

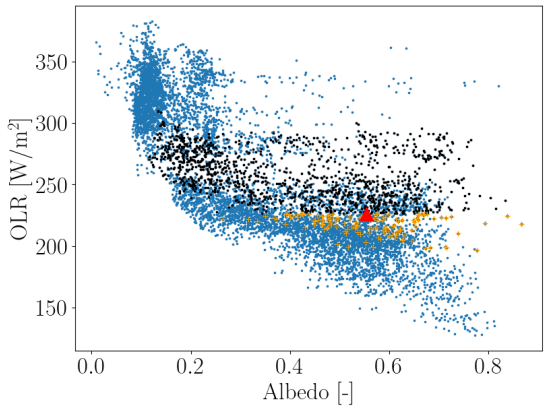

(c) Percentile 10th for the approach 2.

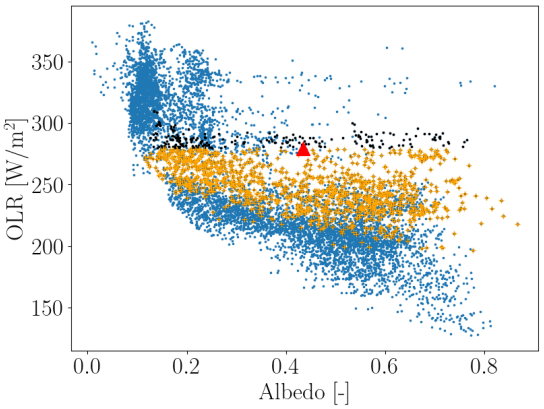

(d) Percentile 90th for the approach 2.

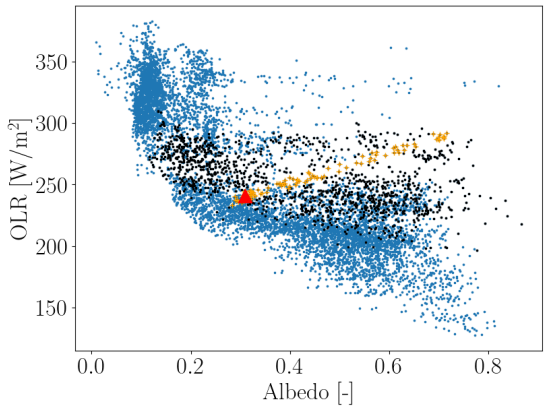

(e) Percentile 10th for the approach 3.

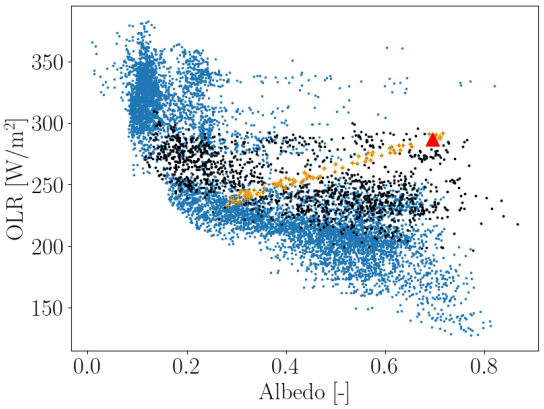

(f) Percentile 90th for the approach 3.

Figure 3.15: Comparison of the OLR-albedo worst-case representative pair percentiles 10th and 90th following approach 1, approach 2 and approach 3, for $z = 6$ km, SZA $= 63°$, during the launch window for BEXUS 32 mission at $\lambda = 66.5°$, $\phi = 21.5°$. Blue circle marker: all data at $\lambda = 66.5°$, $\phi = 21.5°$; Black square marker: subset at $z = 6$ km, SZA $= 63°$; Yellow sum operator marker: subset at certain percentile; Red triangle marker: representative pair [75].

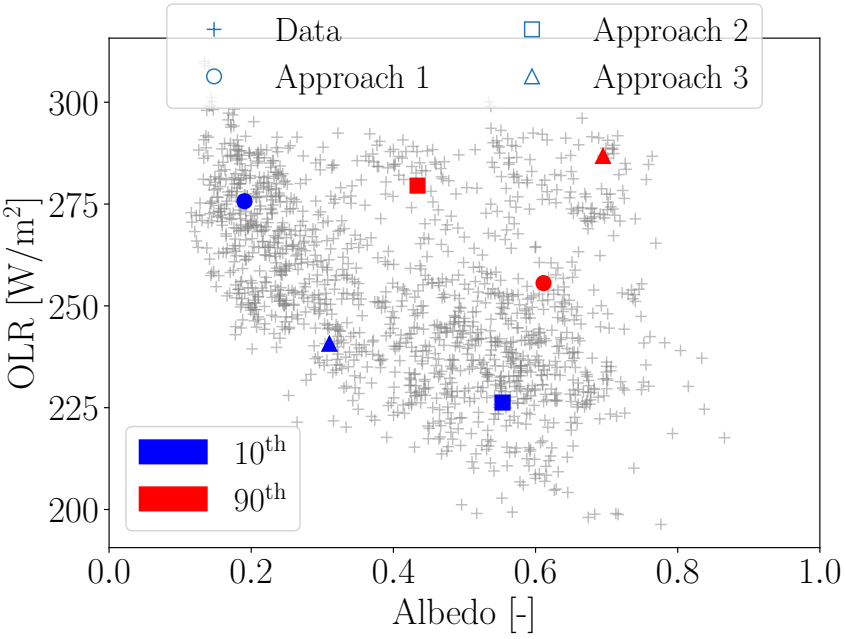

Figure 3.16: Variation of the OLR-albedo worst-case representative pairs percentiles as a function of the approach. Circle marker: approach 1 (for the albedo coefficient data, obtain a certain percentile, and the associated average value for the OLR); square marker: approach 2 (for the OLR data, obtain a certain percentile, and the associated average value for the albedo coefficient); triangle marker: approach 3, (Normalize the OLR-albedo pair distribution) for $z = 6$ km, SZA $= 63°$, during the launch window for BEXUS 32 mission at $\lambda = 66.5°, \phi = 21.5°$ [75]. Red color: percentile 90^{th}; blue color: percentile 10^{th}.

3.3.1.3 Sky temperature

The 90^{th} and 10^{th} percentiles for the sky temperature at each element of the mesh defined in altitude and SZA are shown in Figure 3.17, where the negligible effect of the SZA is clearly shown.

3.3.2 Convective parameters

The approach followed to determine the worst-case conditions for the convective parameters is similar to the one followed for the radiative parameters. Firstly, the raw data from ECMWF [71] is grouped by the SZA for each of the altitudes, from the minimum value to the maximum value in light conditions that will occur in the launch window, and a grid is defined of the data in altitude and SZA. Then, in each of the elements of this mesh, the data of the variable to be analysed are processed, defining the 90^{th} and 10^{th} percentiles to define the potential hot and cold thermal en-

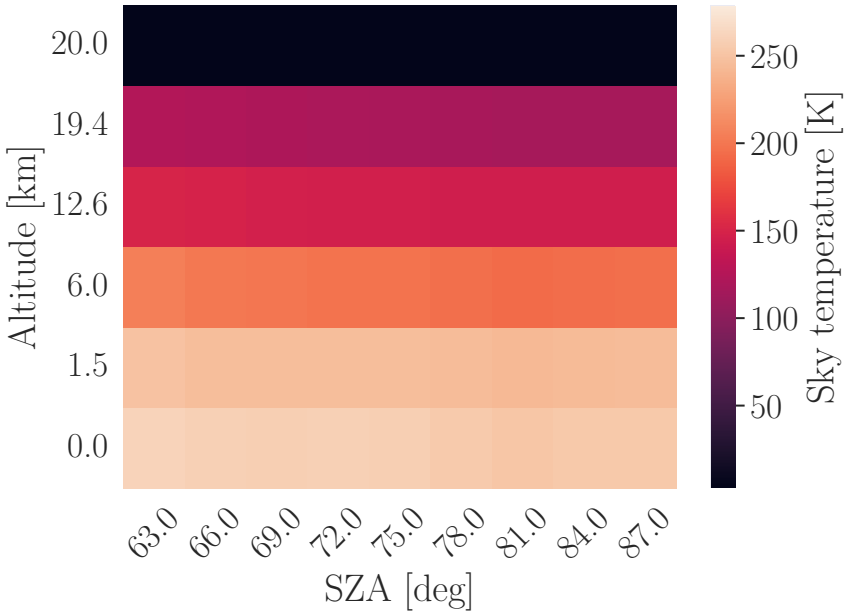

(a)

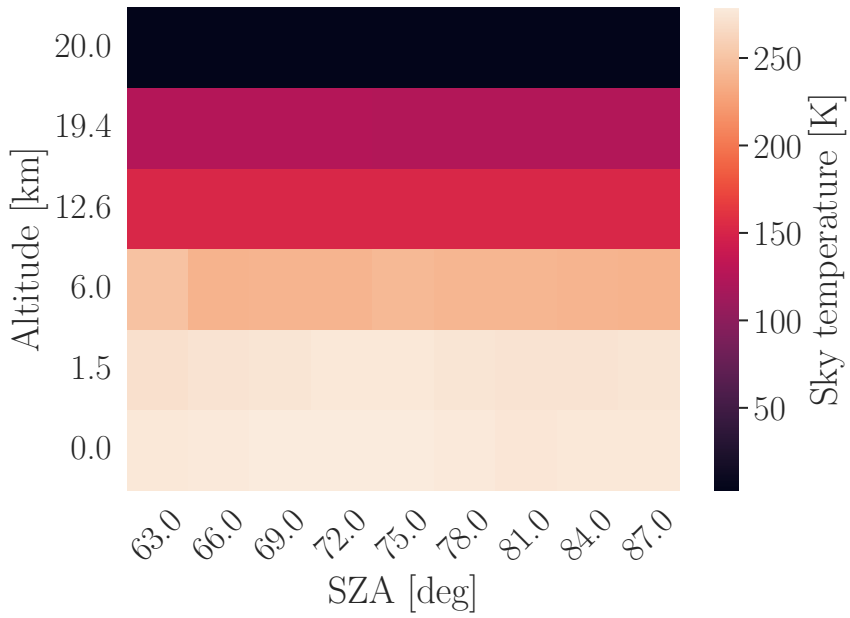

(b)

Figure 3.17: Variation of the equivalent sky temperature percentiles 10^{th} (a), and 90^{th} (b), as a function of altitude and SZA, during the launch window for BEXUS 32 mission at $\lambda = 66.5°, \phi = 21.5°$ [75].

vironments. The results obtained for the BEXUS 32 mission are presented and discussed as an example in the following paragraphs.

3.3.2.1 Air temperature

The influence of the time of day (of the SZA) on the air temperature is analysed, and then, the need for taking it into account is considered. To do this, a box-and-whisker plot of the air temperature is shown in Figure 3.18, where the $x-$axis stands for the altitude and in the $y-$axis represents the air temperature at one cell of the grid in latitude and longitude. Each box shows the quartiles of the dataset while the whiskers extend to show the rest of the distribution, except for points that are determined to be "outliers" using a method that is a function of the inter-quartile range [91]. In Figure 3.18, the ends of the box represent the 25^{th} and 75^{th} percentiles, while the line inside the box is the 50^{th} percentile.

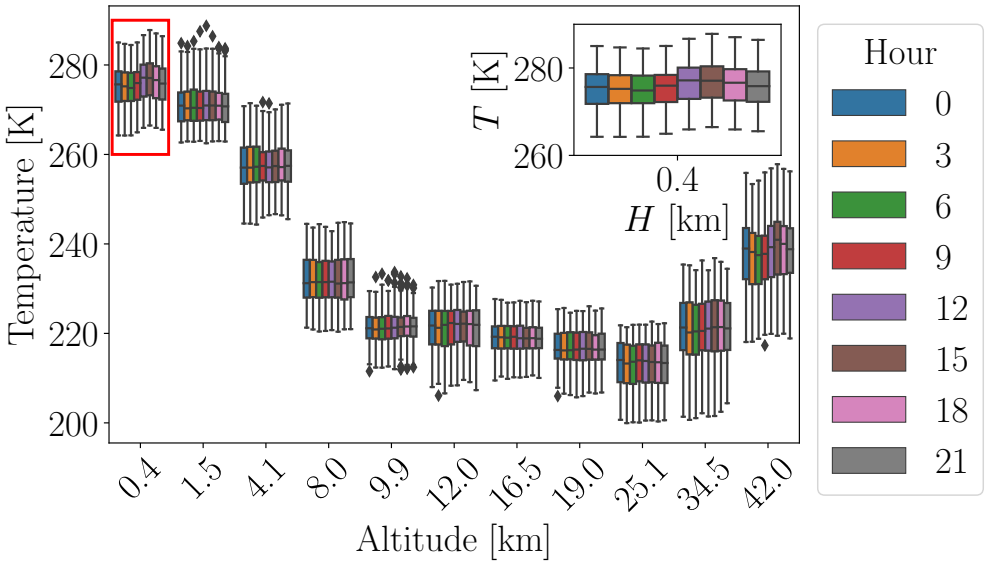

Figure 3.18: Box-and-whisker plot of the air temperature during the launch window for BEXUS 32 mission at $\lambda = 66.5°, \phi = 21.5°$ as a function of altitude comparing different daytime hours [71]. Insert: zoom of the first box on the left.

It is clearly that shown at each altitude the variation of the percentile is much larger than the influence of the time of day. Then, it is decided to consider only the dependence of the air temperature on the altitude. To do so, as it was done with the radiative parameters, the percentile 10^{th} and 90^{th} are obtained at each altitude, as is shown in Figure 3.19.

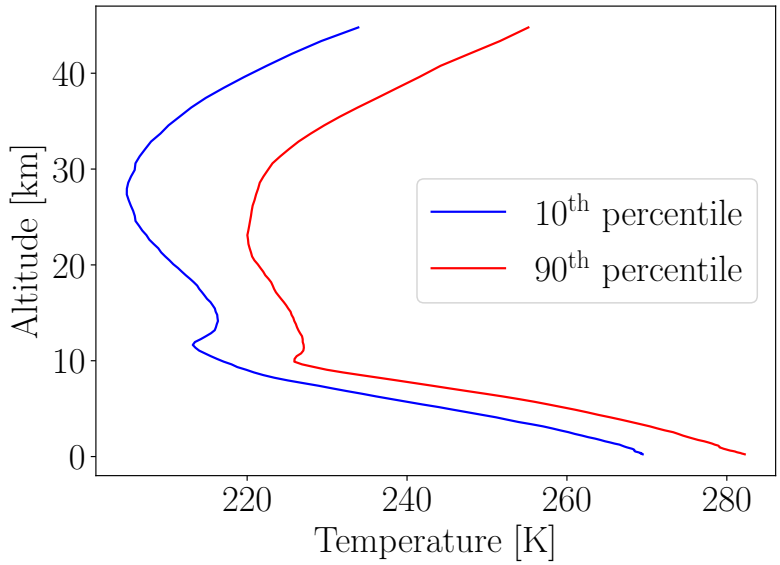

Figure 3.19: Variation of the percentiles 10^{th} (blue) and 90^{th} (red) of the air temperature as a function of altitude, during the launch window for BEXUS 32 mission at $\lambda = 66.5°, \phi = 21.5°$ [71].

3.3.2.2 Air pressure

The different pressure levels are converted into altitude following the approach described in [88]. In Figure 3.20, it is represented the relationship between the air pressure with the altitude and the hour of the day (the SZA) through a box-and-whisker plot, as it was done with the air temperature. It is clearly shown that in this case there is not a relevant dependence of the SZA on the air pressure.

Then, it is decided to determine the limit 10^{th} and 90^{th} for the two potential air pressure profiles, which are represented in Figure 3.21.

3.3.2.3 Air wind speed

The air wind speed raw data has two components, the northward and the eastward components (the downward component is negligible).

As previously done with the air temperature, the influence of the time of day (of the SZA) on each air speed component is analysed in order to decide whether it needs to be taken into account. The results are shown in Figure 3.22, where the y-axis stands for the wind speed and in the x-axis represents the altitude at one cell of the mesh in latitude and longitude.

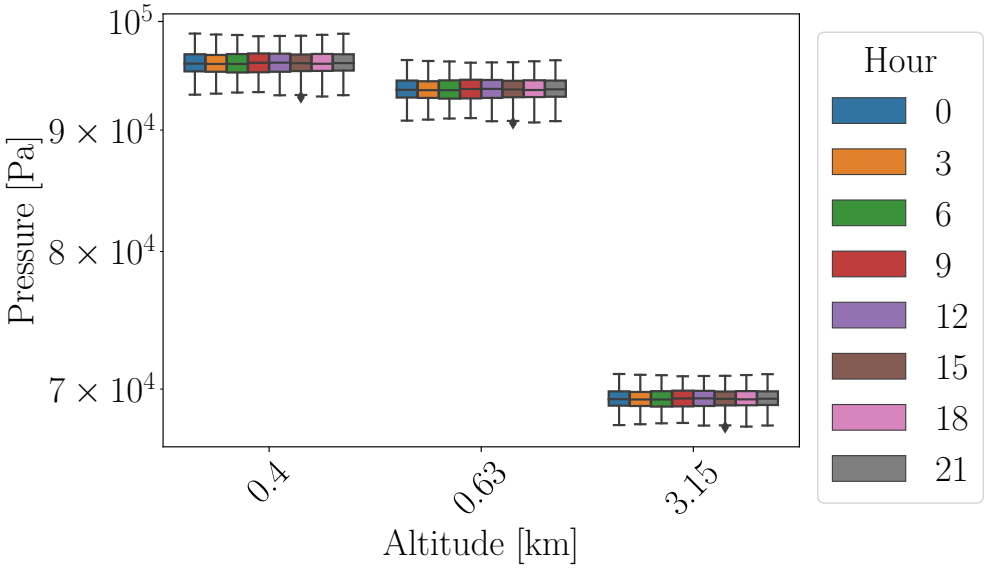

Figure 3.20: Box-and-whisker plot of the air pressure during the launch window for BEXUS 32 mission at $\lambda = 66.5°, \phi = 21.5°$ at different altitude comparing different daytime [71].

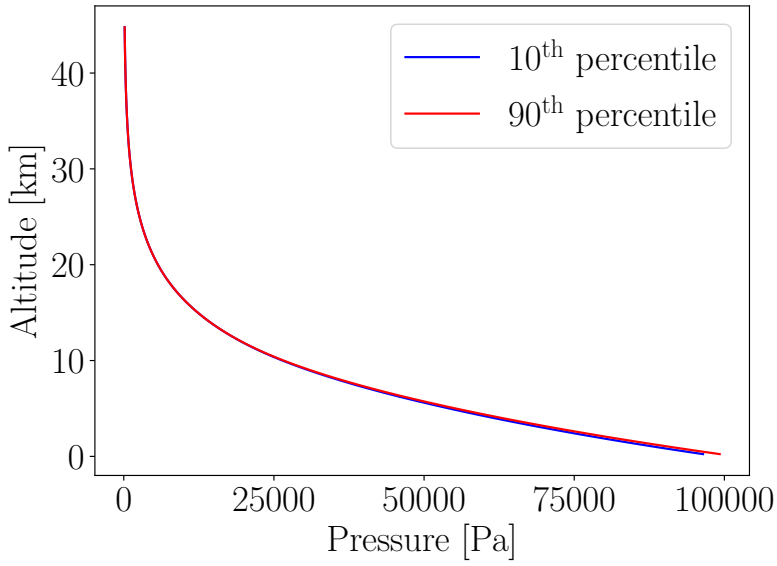

Figure 3.21: Variation of the percentiles 10^{th} (blue) and 90^{th} (red) of the air pressure as a function of altitude, during the launch window for BEXUS 32 mission at $\lambda = 66.5°, \phi = 21.5°$ [71].

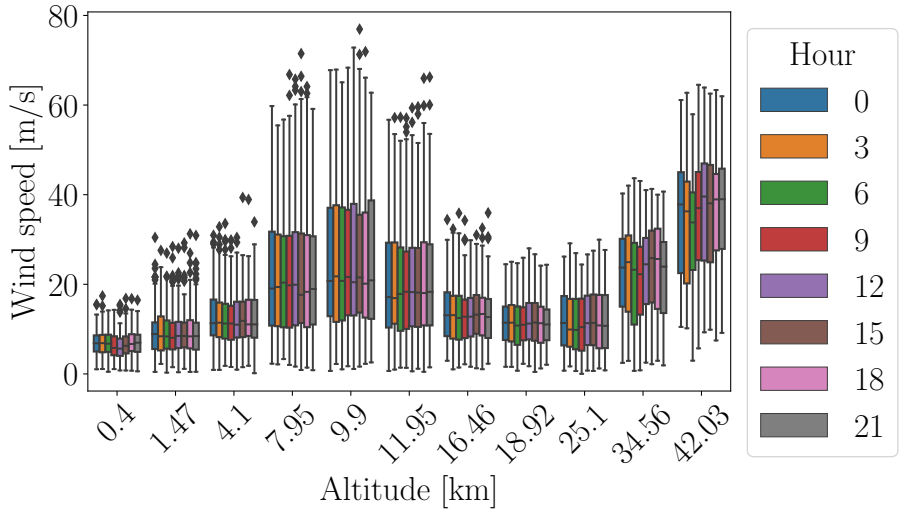

Figure 3.22: Box-and-whisker plot of the air wind speed during the launch window for BEXUS 32 mission at $\lambda = 66.5°, \phi = 21.5°$ at different altitude comparing different daytime [71].

Then, the percentile 10^{th} and 90^{th} of the wind speed magnitude are shown in Figure 3.23.

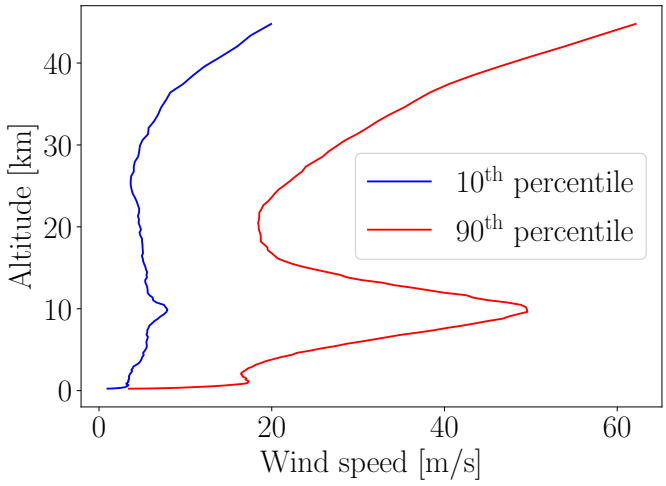

Figure 3.23: Variation of the percentiles 10^{th} (blue) and 90^{th} (red) of the air wind speed as a function of altitude, during the launch window for BEXUS 32 mission at $\lambda = 66.5°, \phi = 21.5°$ [71].

3.4 Ascent phase motion

Modelling the dynamics of the balloon during its ascent phase is a very complex problem that requires the combination of aerodynamic, thermal and geometric models, together with the definition of the thermal environment. This interaction is essential to correctly simulate the ascent dynamics. As already mentioned, many studies have been carried out on this subject to date.

In 1974, the state-of-the-art work to date was developed by Kreider [92], with the aim of predicting the performance of high-altitude balloons by introducing the effects of direct and reflected solar radiation, terrestrial and atmospheric infrared radiation, convection and radiative emission. With this model, during the ascent phase too high ascent rates were predicted below the tropopause and too slow velocities above it, compared to flight data.

In 1981, the previous model was improved by Carlson [93] taking into account the experimentally observed gas temperature rise, obtaining a good agreement with the flight data during the entire flight. In 1990, based on both previous work, the state-of-the-art tool was created by Runnels [94] to simulate ballooning vertical motion, named SINBAD .

In 2003, for the first time, the horizontal and vertical trajectory modeling was integrated by Pankine [95], improving the fidelity of the thermal models in their tool named NAVAJO. In 2004, 48-h wind forecast data was introduced by Musso [96] to improve the horizontal trajectory prediction. Almost in parallel, a new tool to simulate the vertical and horizontal motions of the high-altitude balloons was developed by Farley [68] for NASA.

The thermodynamic model to predict the zero-pressure balloons thermal behaviour during the ascent phase was modified by Palumbo [69] in 2007 and by Liu [97] in 2012. They compared their simulations with flight tests data, obtaining a good agreement. In 2009, from daily ECMWF weather forecast, a statistical estimation of the trajectory error was performed by Morani [98], who maximised the probability of reaching a predefined target area at the float altitude. Following the study, in 2010, an accurate statistical estimation of trajectory prediction errors and its direct application to nominal trajectory simulation without the use of Monte Carlo analysis was developed by Palumbo [99].

In 2014, Monte Carlo techniques to predict the landing area were used by [100]. In 2015, the effects of launch location and launch date using analytical formulas based on global values was studied by Zhang [101]. In 2016, a genetic algorithm to predict the necessary inflation quantity was implemented by Saleh [102], using analytical formulas to define the thermal environment based on global values. In 2017, the predicted trajectories of a scientific balloon considering various

uncertainties were numerically analysed by Lee [103], with the use of Monte Carlo simulations.

Hence, over the years, dynamic-thermal-geometric models have been developed and improved to simulate the ascent phase of zero-pressure balloons [68], [69], [92]–[103]. However, to the author knowledge, no model has used local values obtained from extense databases generated by spacecraft-borne sensors to define the thermal environment interacting with the balloon, except in recent works, where the previous day's predicted air temperature and wind speed have been used to estimate the trajectory. Therefore, based on the dynamic and thermodynamic equations to estimate the balloon trajectory, a deep statistical study of the local data of the radiative and convective environment is carried out, which will feed the model allowing us to obtain the relative velocity needed to analyse the thermal behaviour of a payload during the ascent phase.

The aim of this chapter is to study the influence of the above mentioned parameters on the ascent rate and the horizontal relative wind speed prediction. Since they are the main contributors to the convective heat cooling during the ascent phase, the objective is to obtain the worst-case conditions that allows a robust thermal design for missions that share some common characteristics (such as the launch window, the launch site, or the balloon film thermo-optical properties). To do so, the variability range of these parameters is obtained for the launch station of Esrange (Kiruna) based on both, local environmental data and registered trajectories of stratospheric mission from the REXUS/BEXUS programme. From this study, an envelope of relative velocity (in terms of the ascent rate) is obtained, which can be used for missions of similar characteristics, is obtained. To show the relevance of this study, the influence of these parameters in the temperature response of a payload onboard a stratospheric balloon is analysed. Moreover, the methodology followed to extend this analysis to other type of mission is presented.

3.4.1 Dynamics model

As has previously been described in chapter 1, the forces acting on the balloon-borne system are the buoyancy force, **I**, the aerodynamic drag force, **D**, and the balloon-borne weight, **W**. Hence, the acceleration of the balloon-borne motion, in North-East-Down (NED) frame is obtained from [69],

$$\frac{\mathrm{d}^2\mathbf{r}}{\mathrm{d}t^2} = \frac{\mathbf{W}+\mathbf{I}+\mathbf{D}}{m_t}, \tag{3.14}$$

where **r** is the position of the center of mass. The balloon-borne weight, **W** is defined as,

$$\mathbf{W} = m_G \mathbf{g}, \tag{3.15}$$

where m_G is the sum of the payload mass, m_p, the balloon film mass, m_B and ballast mass, m_b, (if any), and $\mathbf{g}$ is the gravity acceleration.

The buoyancy force, $\mathbf{I}$, can be obtained from,

$$\mathbf{I} = \mathbf{g}\left(\rho_a - \rho_g\right) V, \tag{3.16}$$

where ρ_a is the air density, ρ_g is the lifting gas density, and V is the balloon volume, computed following the ideal gas assumption [68]:

$$V = \frac{m_g}{\rho_g} = m_g R_g \frac{T_g}{p_g}, \tag{3.17}$$

where T_g, p_g and R_g, are the temperature, the pressure, and the specific gas constant of the lifting gas, respectively.

The total mass, m_t, is computed as the sum of three components,

$$m_t = m_G + m_g + m_{add}, \tag{3.18}$$

where m_g is the lifting gas mass, and m_{add} is the additional mass, which takes into account the flow unsteadiness as an added mass effect, which appears when a non-lifting bluff body immersed in a fluid (air), is accelerated,

$$m_{add} = C_{add} \rho_a V. \tag{3.19}$$

The values of the coefficient C_{add} are assumed to be in the range $0.25 < C_{add} < 0.5$ [68].

The lifting gas mass can be estimated taking into account the excess of gas that the zero-pressure balloons require to be launched [11] using,

$$m_g = \frac{m_G \left(\frac{F_L}{100} + 1\right)}{\frac{\mathrm{M}_a}{\mathrm{M}_g} - 1}, \tag{3.20}$$

where F_L, the free lift, is the percentage of the extra gas (typical values are around $10 - 20\%$ [69]). M_g and M_a are the molecular mass of the lifting gas and the air, respectively.

The drag force is defined as,

$$\mathbf{D} = \frac{1}{2} \rho_a \mathrm{v}^2 A C_D \frac{\mathbf{v}}{\mathrm{v}}, \tag{3.21}$$

where $\mathbf{v}$ is the balloon relative velocity to the wind speed, computed as the difference between the balloon velocity, $\dot{\mathbf{r}}$, and the wind speed, $\mathbf{v}_w$, which can be obtained from databases such as [70],

[71], as above mentioned, A is approximated by the balloon top view surface area, and C_D is the drag coefficient.

From (3.14)-(3.21), it is deduced that the computed ascent rate is affected by three types of parameters:

1. The design parameters (such as the gross mass or balloon float volume).

2. The model parameters, which are dependent on the approach used (such as the drag coefficient or the free lift).

3. The heat load parameters, which are environmental magnitudes (e.g. air temperature, OLR, albedo, direct solar radiation or wind speed).

Drag coefficient

The drag coefficient of the balloon film is a relevant parameter to estimate the ascent rate, especially during the first part of the ascent due to the larger air density in the lowest layers of the atmosphere. There is no clear criteria in the literature for quantifying this parameter. Musso et al. [96] proposes a model with a constant value for the drag coefficient, $C_D = 0.45$, during the whole ascent phase, based on comparison flight data. Farley [68] compares the balloon to an ice-cream cone at the earlier stages of the ascent, and proposes an equivalent drag coefficient based on calculated spherical diameter of $C_D = 0.8$, instead of considering the balloon a sphere, where the drag coefficient is a Reynolds function giving values from 0.1-0.47. Conrad and Robin [104] provides a different model that takes into account the variation of the balloon size through the Froude number, $\mathrm{Fr} = \mathrm{v}/\sqrt{\mathrm{g}d}$, and adding a new term to the sphere drag according to:

$$C_D = \frac{4}{3}\frac{1}{\mathrm{Fr}}\left\{1 - \frac{R_a T_a}{R_g T_g}\left[1 + \frac{m_G}{m_g} + \frac{m_g + m_{add}}{m_g g}\frac{\mathrm{d}v_z}{\mathrm{d}t}\right]\right\} + C_{D,\mathrm{Re}}(\mathrm{Re}), \tag{3.22}$$

where R_a is the specific air constant. The characteristic length to compute Re and Fr is the balloon diameter, d (see subsection 3.4.3). It is clear that the lower the drag coefficient the greater the ascent rate, so this parameter should be adjusted very carefully for accurate predictions.

3.4.2 Balloon film thermal model

As already mentioned, the thermal environment should be taken into account to compute both the balloon film and the lifting gas temperatures. The radiative and convective heat fluxes that are involved in their determination are described in the following subsections.

3.4.2.1 Radiative thermal loads

Concerning the radiative interactions that takes place at the balloon film surface, the following energy fluxes should be considered: the solar direct flux, the reflection of the solar flux on the Earth surface (albedo), the IR flux emitted by the ground (OLR), and the IR flux emitted by the sky. In addition, the thermo-optical properties of the balloon film are needed to consider not only the outer film interactions but also the multiple reflections that take place in the inner body of the film.

The direct solar heat load absorbed by the balloon film can be computed from [68]:

$$\dot{Q}_S = \alpha A_p G_S \left[1 + \frac{\tau_S}{1 - \rho'_S}\right], \tag{3.23}$$

where A_p is the projected area of the balloon surface in the Sun direction, G_S is the solar irradiance, α is the solar absorptance, ρ'_S is the solar reflectivity, and τ_S is the solar transmissivity. The term in brackets represents the additional solar absorption due to the multiple reflections in the inner body of the film.

The albedo heat load absorbed by the balloon film is defined by:

$$\dot{Q}_{albedo} = \alpha A_B \cdot \dot{q}_{albedo} \left[1 + \frac{\tau_S}{1 - \rho'_S}\right] F_{BE}, \tag{3.24}$$

where A_B is the balloon film area, F_{BE} is the view factor from the balloon to the Earth, and $\dot{Q}_A$ is the albedo heat flux by unit surface area reflected by the Earth surface placed below the balloon. It can be calculated as,

$$\dot{Q}_A = aG_s \cos\theta, \quad -\frac{\pi}{2} < \theta < \frac{\pi}{2}, \tag{3.25}$$

where a is the albedo coefficient and θ the Solar Zenith Angle (SZA).The longwave diffuse heat load emitted from the ground and absorbed by the balloon film is given by:

$$\dot{Q}_E = \varepsilon A_B \cdot \dot{q}_E \left[1 + \frac{\tau_{IR}}{1 - \rho'_{IR}}\right] F_{BE}, \tag{3.26}$$

where ρ'_{IR} is the infrared reflectivity, and τ_{IR} is the infrared transmissivity.

The longwave diffuse heat load emitted from the sky and absorbed by the balloon film is computed as follows:

$$\dot{Q}_{sky} = \varepsilon A_B \cdot \dot{q}_{sky} \left[1 + \frac{\tau_{IR}}{1 - \rho'_{IR}}\right] (1 - F_{BE}), \tag{3.27}$$

where the sky heat flux, $\dot{Q}_{sky}$, can be calculated as,

$$\dot{q}_{sky} = \sigma T_{sky}^4. \tag{3.28}$$

In addition, the balloon film absorbes infrared self-glow from inside due to the reflections in the inner environment:

$$\dot{Q}_B^{IR} = \varepsilon^2 \sigma A_B T_B^4 \left(\frac{1}{1 - \rho'_{IR}}\right). \tag{3.29}$$

The thermal radiation emitted by the balloon film (being at typical temperatures of some 210 to 270 K) from the outer and inner faces, can be obtained from:

$$\dot{Q}_{out}^{IR} = \varepsilon \sigma 2 A_B T_B^4 \left(1 + \frac{\tau_{IR}}{1 - \rho'_{IR}}\right). \tag{3.30}$$

The terms $\dot{Q}_S$, $\dot{Q}_A$, $\dot{Q}_E$, $\dot{Q}_{sky}$, can be computed based on analytical expressions that take into account global average values [68] or using local data from databases such as [75] to statistically treat the data and to obtain more representative profiles.

3.4.2.2 Convective thermal loads

The balloon film temperature is affected by the convective heat transfer at the inner and outer faces. The external one is generated by the atmospheric air whereas the inner one is produced by the lifting gas.

The convection heat transfer can be obtained in terms of the convection heat transfer coefficient, h_c, which is defined as a function of Nusselt number (Nu), the gas thermal conductivity, k_g, and the characteristic length (the balloon diameter, d):

External convection. Two mechanisms take place, the free convection and the forced convection between the air and the balloon film. The Nusselt number can be obtained from empirical correlations as a function of the Rayleigh (Ra) and the Reynolds (Re) numbers for free and forced convection, respectively [68].

- Free convection:

$$\mathrm{Nu}_{Free} = 2 + 0.45(\mathrm{Gr}_a \mathrm{Pr}_a)^{0.25}. \tag{3.31}$$

- Forced convection:

$$\mathrm{Nu}_{Forced} = 2 + 0.41\mathrm{Re}^{0.55}. \tag{3.32}$$

The external convective exchange can be obtained from [68]:

$$\dot{Q}_{cExt} = -h_{cExt} A_{B,C} \left(T_B - T_a\right), \tag{3.33}$$

where h_{cExt} is the greatest value of the free and forced convection heat transfer coefficient.

Free convection between the balloon film and the lifting gas can be obtained from:

$$\dot{Q}_{cIn} = -h_{cIn} A_{B,C} \left(T_g - T_B\right), \tag{3.34}$$

where the convective heat transfer coefficient h_{cIn} is defined by [68]:

$$h_{cIn} = 0.13 k_g \left(\frac{\rho_g^2 g \left|T_B - T_g\right| \mathrm{Pr}_g}{T_g \mu_g^2} \right)^{1/3}, \tag{3.35}$$

where k_g, ρ_g, Pr_g, and μ_g are the thermal conductivity, the density, the Prandtl number, and the dynamic viscosity of the lifting gas, respectively.

3.4.2.3 Thermal governing equations

Once the environment is defined, the rate of change of the film temperature, T_B, can be computed from the energy balance:

$$\frac{\mathrm{d}T_B}{\mathrm{d}t} = \frac{\dot{Q}_S + \dot{Q}_A + \dot{Q}_E + \dot{Q}_{sky} + \dot{Q}_B^{IR} + \dot{Q}_{cExt} - \dot{Q}_{cIn} - \dot{Q}_{out}^{IR}}{c_f m_B}, \tag{3.36}$$

where c_f is the balloon film specific heat and m_B is the balloon film mass. The thermal inputs contributions are defined in expressions (3.23) to (3.35).

Regarding the lifting gas, taking into account both the convective exchange and the adiabatic expansion of the lifting gas [68], one obtains,

$$\frac{\mathrm{d}T_\mathrm{g}}{\mathrm{d}t} = \frac{\dot{Q}_{cIn}}{m_g c_{vg} \gamma_g} - \frac{\gamma_g - 1}{\gamma_g} \frac{\rho_a g}{R_g \rho_g} \frac{\mathrm{d}z}{\mathrm{d}t}, \tag{3.37}$$

where m_g, c_{vg}, and γ_g are the mass, the specific heat at constant volume, and the adiabatic coefficient of the lifting gas, respectively.

Thus, the resulting equations system for the thermal problem consists on two ordinary differential equations where most of the involved parameters are functions of the altitude.

3.4.3 Geometrical model

During the ascent phase, there is a variation in the balloon volume because the air pressure decreases with the altitude. Thus, the variation in the diameter of the balloon and, therefore, in the aerodynamic cross section area, needs to be taken into account. Considering the balloon as a sphere, the diameter, d, is computed from [68]:

$$d = 2.23 \left(\frac{3}{4\pi} V \right)^{\frac{1}{3}}. \tag{3.38}$$

The surface area of the balloon, A_B, is given by:

$$A_B = \pi d^2. \tag{3.39}$$

The top view projected area of the balloon, A, is:

$$A = \frac{\pi d^2}{4}. \tag{3.40}$$

The effective area for convective calculations [68], $A_{B,C}$,:

$$A_{B,C} = 0.65 A_B + 0.35 A_{B'}, \tag{3.41}$$

with $A_{B'}$ defined by:

$$A_{B'} = 4.94 V_F^{\frac{2}{3}} \left(1 - \cos \left(\pi \frac{L_G}{L_G^F} \right) \right), \tag{3.42}$$

where L_G is the balloon gore length [68]:

$$L_G = 1.914 V^{\frac{1}{3}}. \tag{3.43}$$

3.4.4 System of differential equations

Then, the ascent phase motion of a balloon-borne system requires to solve a system of four differential equations:

$$\frac{\mathrm{d}\mathbf{r}}{\mathrm{d}t} = \dot{\mathbf{r}}, \tag{3.44}$$

$$\frac{\mathrm{d}^2\mathbf{r}}{\mathrm{d}t^2} = \frac{\mathrm{d}\dot{\mathbf{r}}}{\mathrm{d}t} = \frac{\mathbf{W}+\mathbf{I}+\mathbf{D}}{m_t}, \tag{3.45}$$

$$\frac{\mathrm{d}T_B}{\mathrm{d}t} = \frac{\dot{Q}_S + \dot{Q}_A + \dot{Q}_E + \dot{Q}_{sky} + \dot{Q}_B^{IR} + \dot{Q}_{cExt} - \dot{Q}_{cIn} - \dot{Q}_{out}^{IR}}{c_f m_B}, \tag{3.46}$$

$$\frac{\mathrm{d}T_\mathrm{g}}{\mathrm{d}t} = \frac{\dot{Q}_{cIn}}{m_g c_{vg} \gamma_g} - \frac{\gamma_g - 1}{\gamma_g} \frac{\rho_a g}{R_g \rho_g} \frac{\mathrm{d}z}{\mathrm{d}t}. \tag{3.47}$$

The equation system is solved numerically following a fourth-order Runge-Kutta method [105] programmed in Python. A time step of 1 second was considered for the numerical solution of the above system. In fact, with a time step of 10 seconds, it was already observed that the integration step had no influence on the integrated variables, but it was decided to reduce it even further by an order of magnitude due to the speed of solving the system (10 seconds of execution time with the time step of 1 second).

3.5 Tool validation

It should be pointed out that, to the author knowledge, there is not an established criteria in the literature for the drag coefficient model, as it has been mentioned in subsection 3.4.1. After some trials with different possibilities, a constant drag coefficient, $C_D = 0.45$, is used due to the good agreement between the model output ascent rate results and the data from BEXUS data flights. To support this point, the BEXUS flights data from 2014 to 2018 are compared in Figure 3.24 to the model ascent rate results. The thermal environment, for the comparison, has been defined based on the launch daytime data from CERES [75] and ECMWF [71], and the system masses have defined as the flight ones (see Appendix B for the explanation of the oscillations observed in the flight data).

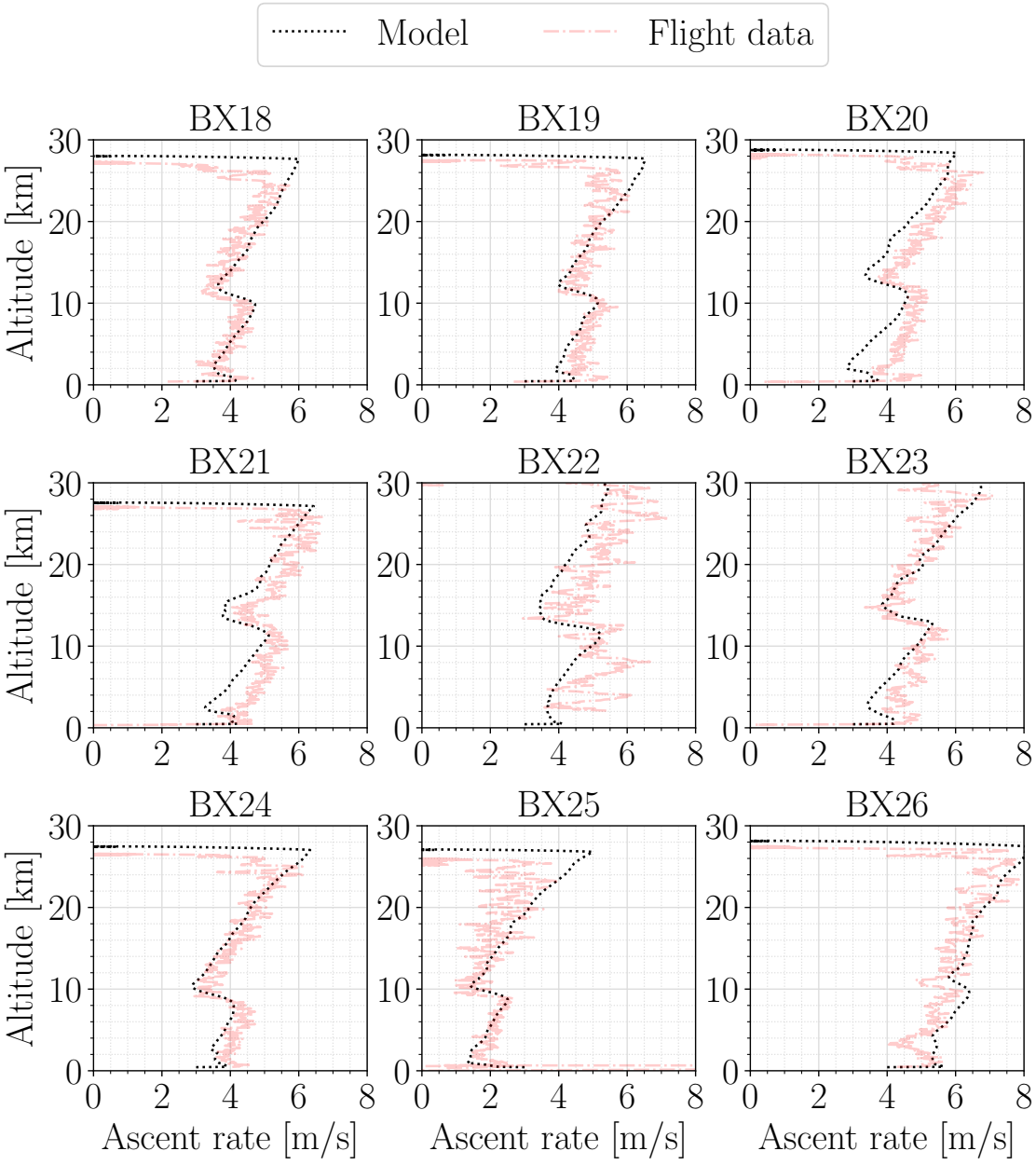

Figure 3.24: Ascent rate profile comparison between BEXUS flights GPS data and the presented model results. Flights BEXUS 18,19 (both launched in 2014); 20,21 (both launched on 2015); 22, 23 (both launched in 2016); 24, 25 (both launched in 2017); and 26 (launched in 2018), are considered.

3.6 Sensitivity analysis of the ascent rate

The specific influence on the ascent rate of each parameter involved is analysed in the following subsections. Only one parameter is modified at a time in order to understand the qualitative effect of the selected parameter on the ascent rate (the quantitative effect is studied in section 3.7).

Air temperature The air temperature vertical profile can be splitted into three stages, the first being from ground up to the tropopause, along which the temperature decreases, the second from the tropopause to the stratosphere, where the temperature remains constant or have a slightly negative slope, and finally, in the stratosphere where the temperature generally increases. Therefore, the slope (lapse rate, γ') of change in the troposphere, and the altitudes at which the tropopause and stratosphere begin, are the free parameters that can be modified to observe their effect on the rate of ascent.

First, the lapse rate in the troposphere is modified while keeping the altitude at which, the tropopause and stratosphere remain constant. The ISA atmosphere [44] is used as the nominal profile (lapse rate of $6.5\,\mathrm{K}\cdot\mathrm{km}^{-1}$) and is modified by increasing or decreasing the slope by 10 % around the nominal value. From the results of this study, shown in Figure 3.25, it is deduced that the higher the slope and, therefore, the lower the air temperature, the higher the ascent rate.

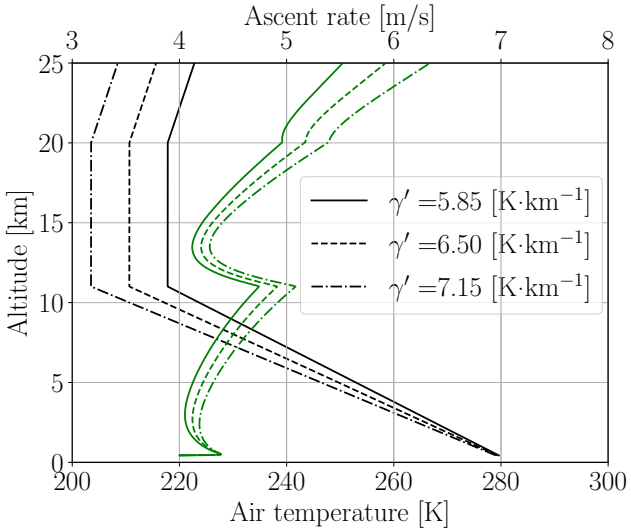

Figure 3.25: Influence on the ascent rate of the air temperature in terms of the lapse rate, γ', in the troposphere. Black lines (air temperature) are referred to bottom x-axis, green lines (ascent rate) refer to top x-axis. Solid lines: ISA profile after decreasing the lapse rate 10%; dashed lines: ISA profile; dot-dashed lines: ISA profile after increasing the lapse rate 10%.

The altitude at which the air temperature stops decreasing and remains constant (the altitude at which the tropopause starts) is modified 1 km up and down with regard to the ISA profile in Figure 3.26. It is shown that the higher the altitude at which the change in air temperature trend takes place, the higher the ascent rate.

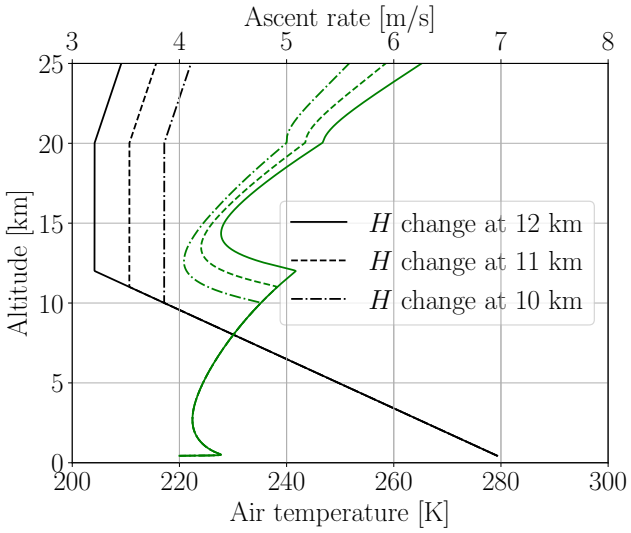

Figure 3.26: Influence on the ascent rate of the air temperature, in terms of the tropopause altitude. Black lines (air temperature) are referred to bottom x-axis, green lines (ascent rate) refer to top x-axis. Solid lines: ISA profile after increasing the tropopause altitude 1 km; dashed lines: ISA profile; dot-dashed lines: ISA profile after decreasing the tropopause altitude 1 km.

Finally, the effect of air temperature at the ground, keeping the same tropopause altitude and lapse rate in the troposphere, is analysed in Figure 3.27, where 10 K have been increased and decreased with regard to the ISA profile. It is shown that the lower the air temperature at the ground, the greater the ascent rate.

Therefore, the air temperature effect on the ascent rate can be summarized:

- The greater the air temperature lapse rate in the troposphere, the greater the ascent rate.
- The greater the tropopause altitude, the greater the ascent rate.
- The lower the air temperature at ground, the greater the ascent rate.

Solar irradiance As above mentioned, solar irradiance increases with altitude due to the absorption of the gases presented in the atmosphere. To analyse the impact of this parameter on the ascent rate, the analytical expression for the solar irradiance proposed by Ref. [68] is modified by

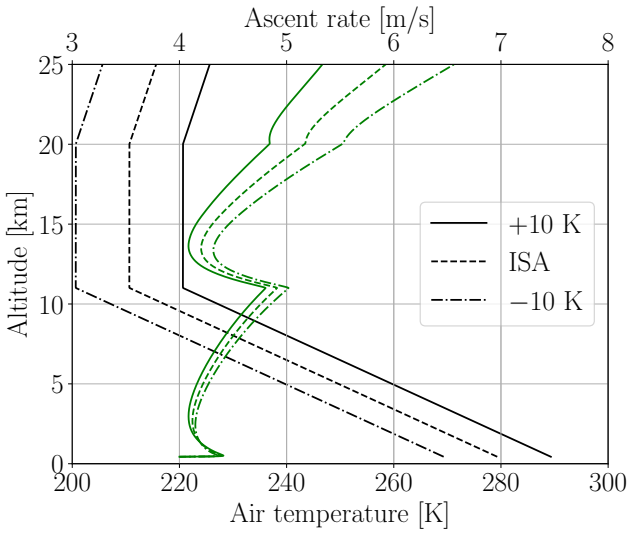

Figure 3.27: Influence on the ascent rate of the air temperature, in terms of the air temperature at the ground. Black lines (air temperature) are referred to bottom x-axis, green lines (ascent rate) refer to top x-axis. Solid lines: ISA profile after decreasing 10 K; dashed lines: ISA profile; dot-dashed lines: ISA profile after increasing 10 K.

increasing/decreasing its value a 10% at each altitude and then by decreasing each value another 10% at each altitude. The results of the calculations are compared in Figure 3.28 where it is shown that the increase of the solar irradiance slightly increases the ascent rate.

OLR The impact of the OLR on the ascent rate is shown in Figure 3.29, where the analytical expression for the OLR proposed by Ref. [68] is modified by increasing/decreasing its value by 65 $\mathrm{W} \cdot \mathrm{m}^{-2}$ at each altitude (see [35]). As in the solar irradiance, the greater the OLR, the greater the ascent rate.

Albedo Despite the albedo coefficient variability shown in Figure 3.8, the analytical models to estimate the ascent rate of the balloon-borne presented in section 3.4, consider it as a constant value. Then, to understand the influence of the albedo coefficient on the ascent rate, the ascent rate obtained is computed for different constant albedo coefficients (to represent different types of planet surface, see subsection 1.4.2). The results are shown in Figure 3.30. During the first stage of the ascent, that is, before reaching the tropopause, the albedo coefficient has no impact on the ascent rate. However, at greater altitudes, the greater the albedo, the greater the ascent rate.

Drag coefficient The drag force combined with the weight are the forces oppose to the lift force. Therefore, the higher the drag coefficient, the lower the ascent rate, as shown in Figure 3.31.

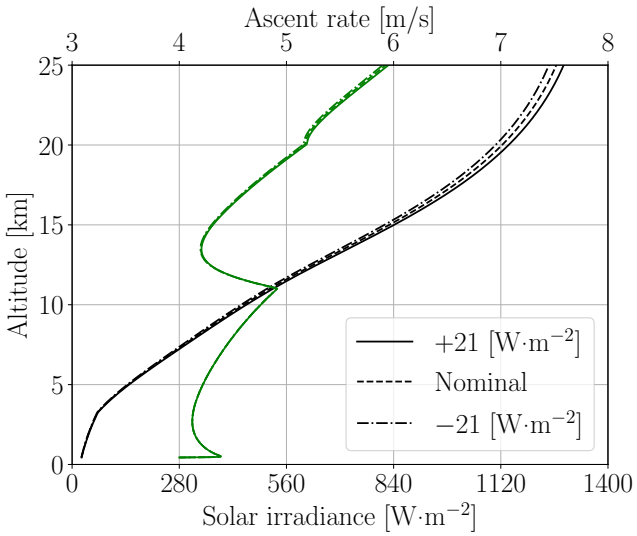

Figure 3.28: Influence on the ascent rate in terms of the solar irradiance. Black lines (solar irradiance) are referred to bottom x-axis , green lines (ascent rate) refer to top x-axis. Solid lines: analytical expression profile after decreasing its value at each altitude a 10%; dashed lines: analytical profile; dot-dashed lines: analytical expression profile after decreasing its value at each altitude a 10%.

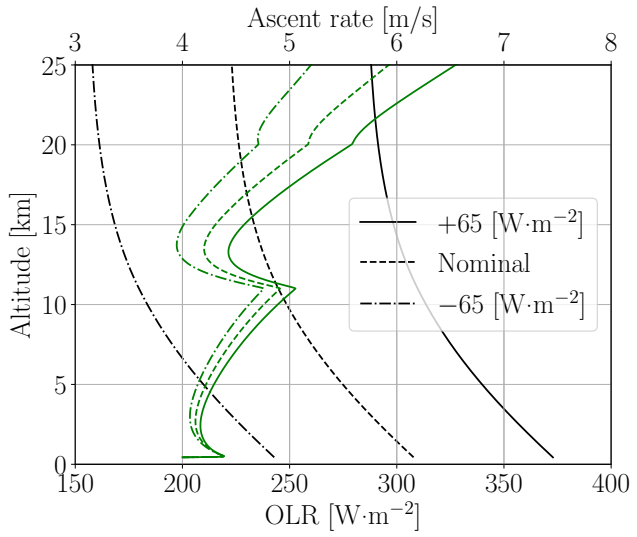

Figure 3.29: Influence on the ascent rate in terms of the OLR. Black lines (solar irradiance) are referred to bottom x-axis , green lines (ascent rate) refer to top x-axis. Solid lines: analytical expression profile after decreasing its value at each altitude 65 W $\cdot$ m^{-2}; dashed lines: analytical profile; dot-dashed lines: analytical expression profile after decreasing its value at each altitude 65 W $\cdot$ m^{-2}.

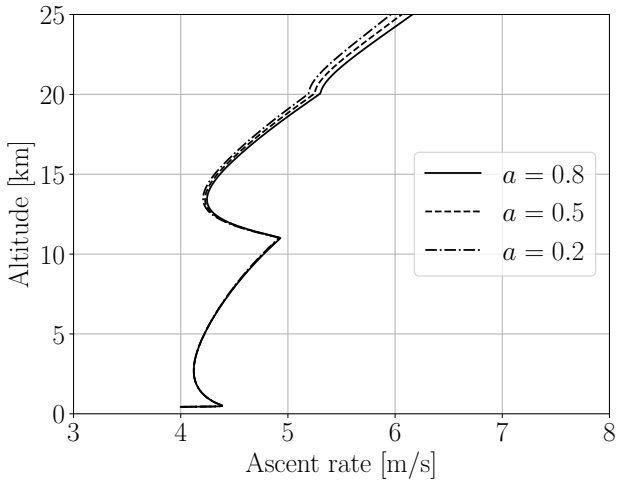

Figure 3.30: Influence on the ascent rate in terms of the albedo coefficient. Solid line: $a = 0.8$; dashed line: $a = 0.5$; dot-dashed line: $a = 0.2$.

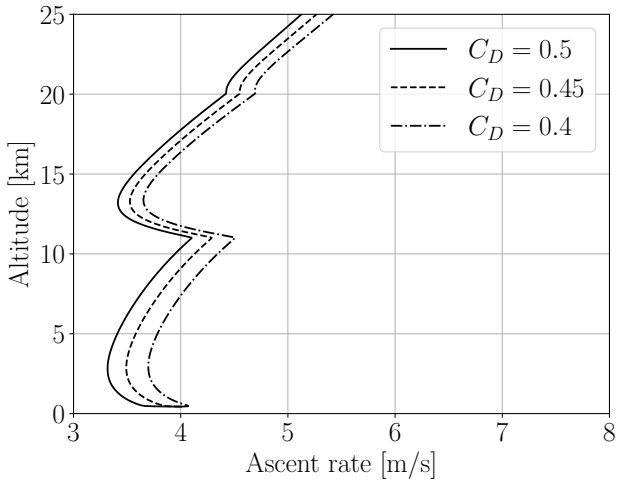

Figure 3.31: Influence on the ascent rate in terms of the drag coefficient, C_D. Solid line: $C_D = 0.5$; dashed line: $C_D = 0.45$; dot-dashed line: $C_D = 0.4$.

Balloon film thermo-optical properties The solar radiation (both direct and albedo) absorbed by the balloon film, and the infrared radiation absorbed and emitted by the balloon film depends on the thermo-optical properties of the film. The results obtained for the ascent rate for different solar absorptivities, α, following two approaches are shown in Figure 3.32. Firstly, the solar transmissivity, $\tau_S = 0.6$, remains constant, and three values of solar absorptivities, α, are compared, (while the solar reflectivity, ρ'_S is self-modified to fulfill (1.4)). Secondly, the same solar absorptivities values are compared but in this case, the solar reflectivity, $\rho'_S = 0.6$, remains constant, and the solar transmissivity, τ_S, is self-modified to fulfill (1.4).

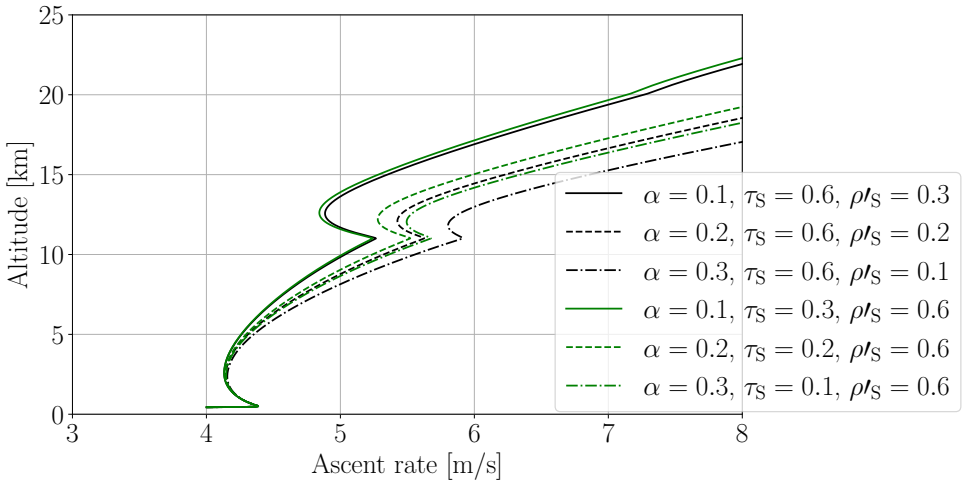

Figure 3.32: Influence on the ascent rate in terms of the solar band thermo-optical properties of the balloon film. Solid line: ascent rate obtained with $\alpha = 0.1$; dashed line: $\alpha = 0.3$; dot-dashed line $\alpha = 0.5$. Black lines: approach with given transmissivity, τ_S. Green lines: approach with given reflectivity, ρ'_S.

Then, the same approach is followed for the infrared band whose results are shown in Figure 3.33, where it is observed that the greater the emissivity, the greater the ascent rate. Besides, the impact on the ascent rate of the transmissivity change is greater than the reflectivity change.

Lifting gas mass The difference in densities between the lifting gas and the air is the origin of the buoyancy force and, therefore, of the lift, as it was described in subsection 3.4.1. Thus, the higher the helium mass, the higher both the buoyancy and the lift force, as shown in Figure 3.34.

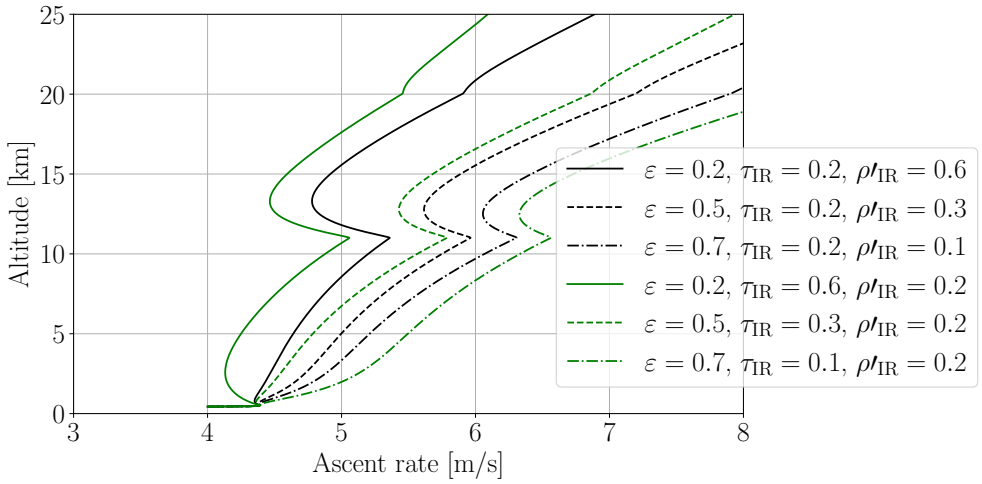

Figure 3.33: Influence on the ascent rate in terms of the infrared band thermo-optical properties of the balloon film. Solid line: ascent rate obtained with $\varepsilon = 0.2$; dashed line: $\varepsilon = 0.5$; dot-dashed line $\varepsilon = 0.7$. Black lines are referred to the approach where the transmissivity, τ_{IR}, remains constant. Green lines: the approach which sets the reflectivity, ρ'_{IR}.

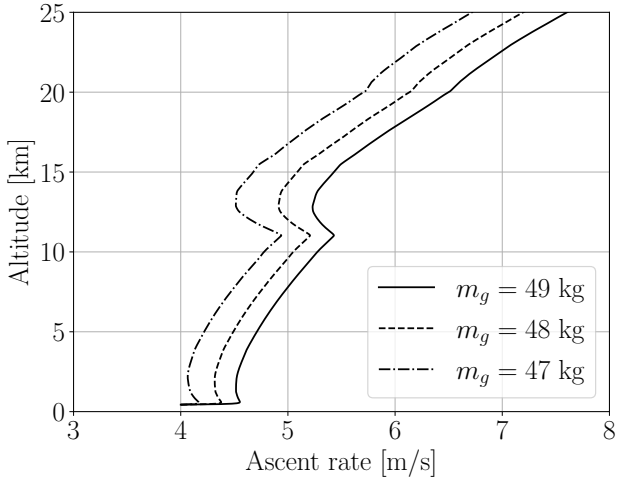

Figure 3.34: Influence on the ascent rate in terms of the lifting gas mass, m_g. Solid line: $m_g = 49$ kg; dashed line: $m_g = 48$ kg; dot-dashed line: $m_g = 47$ kg.

3.7 Influence on the ascent phase by stages

In section 3.6, parameter increments have been considered of the size appropriate performed to obtain appreciable changes in the ascent rate to determine their influence qualitatively. In this section, a study of the influence of every parameter on the ascent rate is carried out in a more formal way . Firstly, the effect of the parameter change on the time taken to reach a given altitude is assessed, and then, their effect is compared in a normalised form. To do so, first, a nominal case is executed with the parameters established in Table 3.1. Then, every parameter is modified one by one according to the increments given in Table 3.1 to obtain the variation of the ascent rate. In addition, the influence at the troposphere and the stratosphere is studied independently, as at the lower layers of the atmosphere the convection will dominate the balloon film temperature while at the upper layers, it will be dominated by the thermal radiation, (and then, the same parameter may have different impact on the ascent rate depending on the altitude). Thus:

- Along the troposphere. Every parameter is modified one by one with regard to its nominal value at ground.
- Along the stratosphere. Every parameter is modified one by one with regard to its nominal value at the tropopause lower limit.

Following the ECSS approach to determine the uncertainty of the thermal results [35] the variation of parameters considered in the sensitivity analysis is summarized in the column *Increment* of Table 3.1, where the subscript N represents the nominal parameter value.

The difference of the flight time required to reach the tropopause (11 km) varying every parameter with regard to the nominal case is plotted in Figure 3.35.

In this first approach, the parameters that show more relevance are the system masses (payload, film and helium) and the drag coefficient: the larger the helium mass, the greatest the lifting force, and the larger the system mass or the drag coefficient, the smaller the lifting force.

However, as the parameter relative variation has not been taken into account in this first comparison, to obtain a more general outcome for this sensitivity analysis, an ascent rate unit coefficient, called influence coefficient of parameter x, λ_x, [106] is defined as follows:

$$\lambda_x = \frac{\text{RMSE}_{v_x}}{\text{RMSE}_x}\delta x, \tag{3.48}$$

Table 3.1: Nominal values and increments values of the parameters considered.

Parameter	Nominal value	Increment
Air pressure, p_a, [Pa]	ISA [44]	$p_{a_N} \times 1.1$
Air temperature, T_a, [K]	ISA [44]	$T_{a_N} + 10$
Drag coefficient, C_D, [-]	0.45	$C_{D_N} \times 1.1$
Helium mass, m_g [kg]	48.0	$m_{g_N} \times 1.1$
Payload mass, m_p, [kg]	155.9	$m_{p_N} \times 1.01$
Balloon film mass, m_B, [kg]	108.2	$m_{B_N} \times 1.01$
Solar absorptance, α, [-]	0.024	$\alpha_N + 0.03$
Solar transmissivity, τ_{s_N}, [-]	0.916	$\tau_{s_N} \times 0.9$
Infrared emissivity, ε, [-]	0.1	$\varepsilon_N + 0.02$
Infrared transmissivity, τ_{IR}, [-]	0.86	$\tau_{IR_N} \times 0.9$
OLR [W · m^{-2}]	OLR$_N$ [68]	OLR$_N$ + 65
Albedo coefficient, a, [-]	a_N [68]	a_N + 0.1
Solar irradiance, G_S, [W · m^{-2}]	G_{S_N} [68]	G_{S_N} + 21
Launch site / date	Esrange / October	[-]
Volume at float altitude, V_F, [m^3]	12000	[-]
Wind speed, $\mathbf{v}_w$ [m · s^{-1}]	ECMWF data [71] at launch site and date	[-]

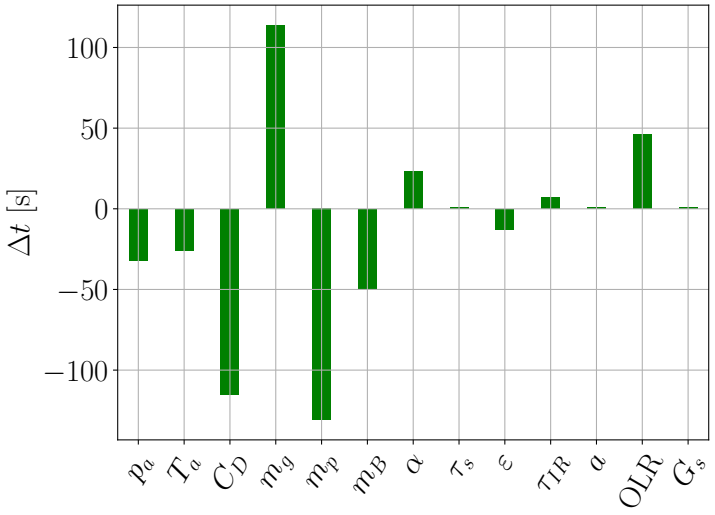

Figure 3.35: Variation of the time of flight to reach the tropopause, Δt, for the parameters in Table 3.1.

where RMSE_{v_x} is the distance between the nominal v_N and the perturbed v_x trajectory, in terms of the ascent rate, defined as the root mean square shift of the ascent rate v shift due to the parameter x increment, considering n points during the ascent phase stage considered (travel through the troposphere, travel through the stratosphere, or the whole ascent phase), as follows:

$$\text{RMSE}_{v_x} = \sqrt{\frac{\sum_{i=1}^{n} \left(v_{x_i} - v_{N_i}\right)^2}{n}}, \tag{3.49}$$

RMSE_x is defined as,

$$\text{RMSE}_x = \sqrt{\frac{\sum_{i=1}^{n} \left(x_i - x_{N_i}\right)^2}{n}}, \tag{3.50}$$

and δx,

$$\delta x = \Delta x \cdot \bar{x}_N, \tag{3.51}$$

where $\bar{x}_N$ is the mean value of the parameter during the ascent phase stage considered, and Δx is defined by:

$$\Delta x = \frac{\bar{x} - \bar{x}_N}{\bar{x}_N}. \tag{3.52}$$

Then, the normalized influence coefficient, $\bar{\lambda}_x$, for the m parameters, is defined as:

$$\bar{\lambda}_x = \frac{\lambda_x}{\left(\sum_{x_i}^{m} \lambda_{x_i}^2\right)^{1/2}}, \tag{3.53}$$

and is represented in Figure 3.36.

Several conclusions can be obtained from Figure 3.36:

- The helium mass (m_g), the payload mass (m_p), and the drag coefficient (C_D) dominates the ascent rate until the tropopause.
- The air temperature (T_a) is relevant during the whole ascent phase but it is more relevant once the troposphere has been exceeded.
- The OLR has a relevant impact during the whole ascent.
- The air pressure (p_a) has an impact until the troposphere is exceeded.
- The direct solar radiation (G_s) has relevance through the balloon film solar absorptance, α, specially once the tropopause has been exceeded.

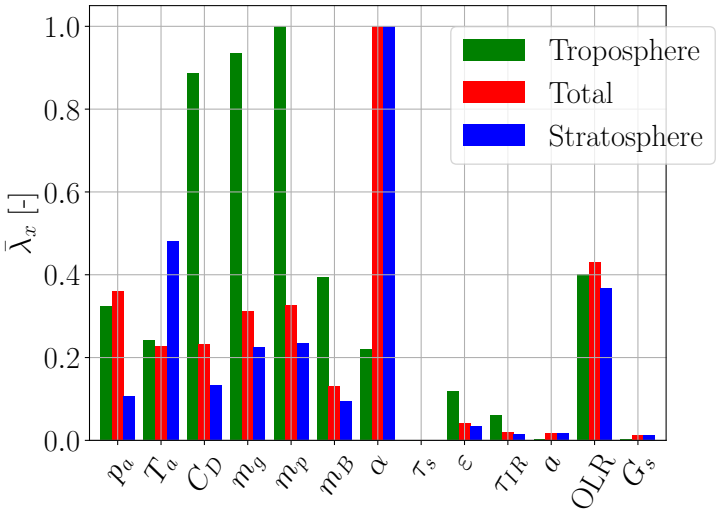

Figure 3.36: Normalized influence coefficient, $\bar{\lambda_x}$, for the parameters in Table 3.1. Green bars: the value of the parameter is incremented at ground, and $\bar{\lambda_x}$ is compared at $z = 11$ km (travel through the troposphere). Red bars: the value of the parameter is incremented at ground and, $\bar{\lambda_x}$ is compared at the float altitude. Blue bars: the value of the parameter is incremented at the tropopause, and $\bar{\lambda_x}$ is compared at the float altitude (travel through the stratosphere).

Hence, to obtain an envelope for the ascent rate values that allows robust thermal design of the payload based on worst-case analyses, the environmental parameters should be studied to define potential profiles with the altitude. The procedure followed is described in section 3.8.

Besides, the influence of the system masses will be evaluated throughout the free lift (see (3.20)). Regarding the balloon film solar absorptance, as this parameter depends on the balloon selected for the mission, it is decided to particularize the study with BEXUS program balloon. However, one should have in mind that the impact of the sun heat load on the ascent rate becomes more relevant as the solar absorptance of the balloon film increases (actually the ratio α/ε increases).

3.8 Thermal environment worst-case selection approach

To obtain representative ascent rate profiles from the thermal point of view, the effect of the most important parameters, the air temperature, the direct solar radiation, and the OLR (in con-

sequence also the albedo due to their relationship [16]), is considered.

The definition of thermal environment considered here is based on two different methods to obtain the vertical profile of these parameters. In the first method, the profiles of these parameters are obtained from the analytical expressions of [68], which considers global averaged values. In the second approach, the methodology presented in section 3.3 is followed to obtain the thermal environment profiles based on local data, which is obtained from databases (CERES [75] and ECMWF [71] for the radiative parameters, and the air temperature and wind speed respectively), and treated statistically to define three confidence levels, 10%, 90%, and mean values, as a function of both the altitude and the launch time.

3.8.1 Direct solar radiation.

The analytical expression of the direct solar radiation, $\dot{q}_{sun}$ is obtained from [68], taking into account the attenuation in the solar irradiance due to the presence of the atmosphere. The profiles of the direct solar radiation, $\dot{q}_{sun}$, obtained from the different approaches are represented in Figure 3.37, considering the launch time at 10:00 am.

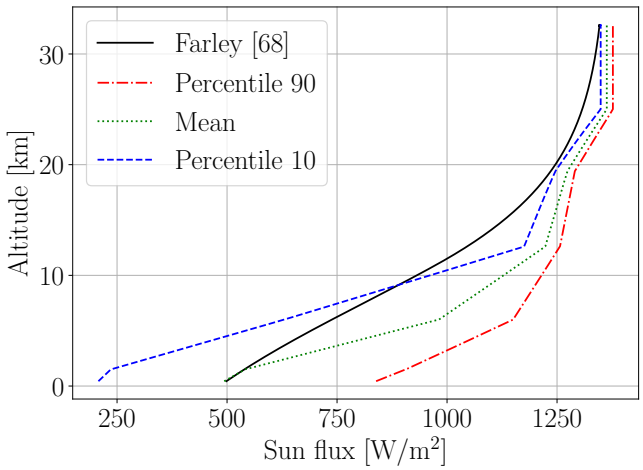

Figure 3.37: Direct solar radiation, G_S, vertical profiles. Analytical expression from [68], (solid black line). Data from [75]: 10% confidence level (dashed blue line); mean confidence level (dotted green line); 90% confidence level (dot-dashed red line).

3.8.2 Earth IR radiation.

As the solar irradiance, there is an attenuation in the OLR due to the presence of the atmosphere. The profiles of the Earth IR radiation, $\dot{q}_{Earth}$, obtained from the different approaches are represented in Figure 3.38, considering the launch time at 10:00 am.

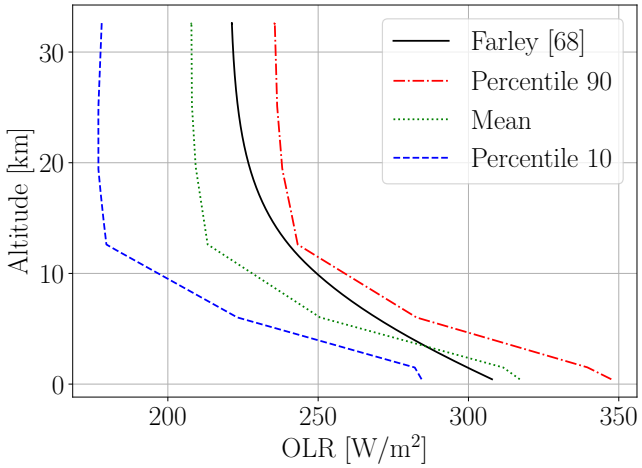

Figure 3.38: OLR vertical profiles. Analytical expression from [68], (solid black line). Data from [75]: 10% confidence level (dashed blue line); mean confidence level (dotted green line); 90% confidence level (dot-dashed red line).

3.8.3 Albedo heat flux.

The profiles of the albedo coefficient, a, obtained from the two approaches are represented in Figure 3.39, considering the launch time at 10:00 am.

3.8.4 Air temperature.

The International Standard Atmosphere (ISA) air temperature profile [44], which consider the global average values, is compared to the data obtained from [71] and statistically treated in Figure 3.40.

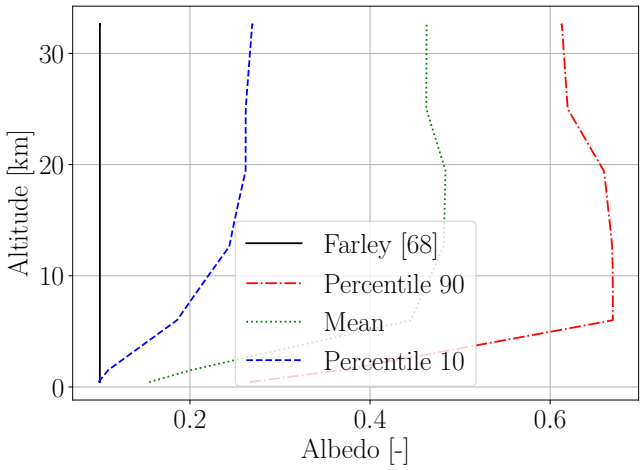

Figure 3.39: Albedo coefficient vertical profiles. Analytical expression from [68], (solid black line). Data from [75]: 10% confidence level (dashed blue line); mean confidence level (dotted green line); 90% confidence level (dot-dashed red line).

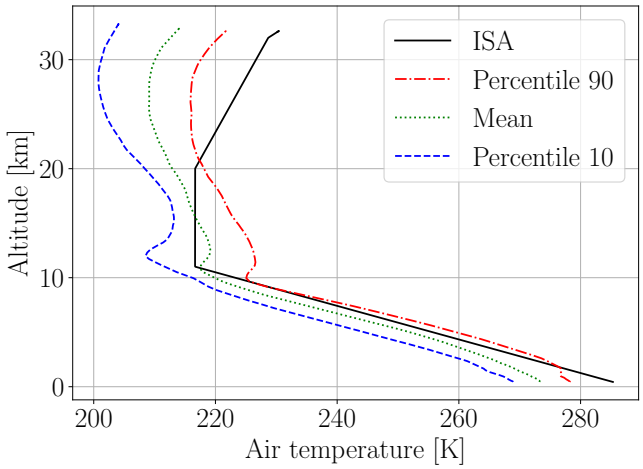

Figure 3.40: Comparison of air temperature profiles. ISA, (solid black line). Data from [71]: 10% confidence level (dashed blue line); mean confidence level (dotted green line); 90% confidence level (dot-dashed red line).

3.8.5 Wind speed.

The wind speed magnitude profiles, are obtained based on local data from [71]. Its statistically results are shown in Figure 3.41.

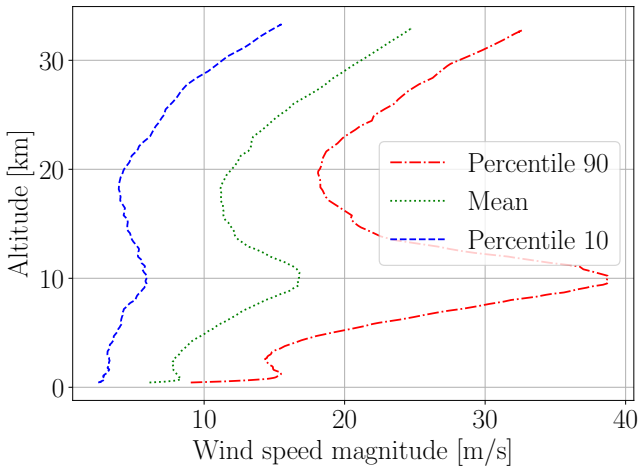

Figure 3.41: Comparison of wind speed vertical profiles. Data from [71]: 10% confidence level (dashed blue line); mean confidence level (dotted green line); 90% confidence level (dot-dashed red line).

3.9 Case study I. Flat plane

The analysis performed in section 3.7 shows that the masses of the balloon-borne system have a relevant impact on the ascent rate. Specially, the lifting gas mass. Then, two lifting gas mass are considered per thermal environment to take into account the uncertainty on this parameter. To do so, the free lift is set to 10% and 20%. In addition, due to specially the radiative profiles are strongly dependent on the SZA (launch time) [16], two hours are considered, at 7 am where the SZA is the greatest at light conditions, and at 10 am where the SZA is the lowest.

The profiles that defines the maximum relative velocity is the combination of the percentile 10% air temperature profile, the percentile 90% of the solar irradiance, the OLR, and the wind speed with $F_L = 0.2$ at 10:00 am UTC. This parameter combination maximise the buoyancy force (increase the lifting gas and air density difference). The profiles that defines the minimum ascent rate are the combination of the percentile 90% air temperature profile, the percentile 10% the solar irradiance, the OLR, and the wind speed with, with $F_L = 0.1$ at 7:00 am UTC. The

ascent rate envelope is shown in Figure 3.42, compared to the BEXUS flights envelope, from 2014 to 2018 campaigns (except for BEXUS 25 flight due to unusual slow ascent [22]), showing a good agreement. Hence, a potential envelope of ascent rate profile has been obtained for missions with a balloon volume of 12 000 m^3 taking into account the thermal environment (particularized for the launch site and launch epoch), the launch time, and the lifting gas mass typical uncertainties.

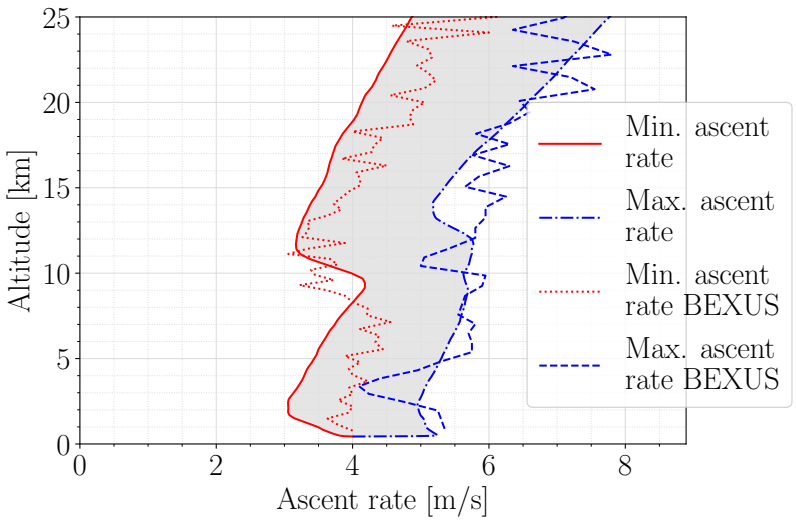

Figure 3.42: Ascent rate envelope. Results of the model: maximum ascent rate (dot-dashed blue line); and minimum ascent rate (solid black line). Flight data from BEXUS missions: maximum ascent rate, BEXUS 26 (dashed blue line); and minimum ascent rate, BEXUS 18 (dotted red line).

3.9.1 Impact of the ascent rate in the temperature payload

Once the envelope of the ascent rate has been defined, the impact on the temperature of a payload (simplified to a square flat plate) during the ascent phase is analysed. The thermal environment is defined according to the one used to obtain the relative velocity profiles. The characteristic length of the flat plate is set to 200 mm with a thickness of 3 mm. The material is assumed to be aluminum with a density $\rho = 2700\,kg/m^3$, and a specific heat capacity $c = 900\,J \cdot kg^{-1} \cdot K^{-1}$. Finally, the power dissipation of the plate is set to $\dot{Q}_{heat} = 5\,W$, and the thermo-optical properties to $\alpha = 0.2$ and $\varepsilon = 0.8$. With all this data, and using the model presented in subsection 3.2.2, the profiles of the payload temperature plate, which are represented in Figure 3.43, are obtained.

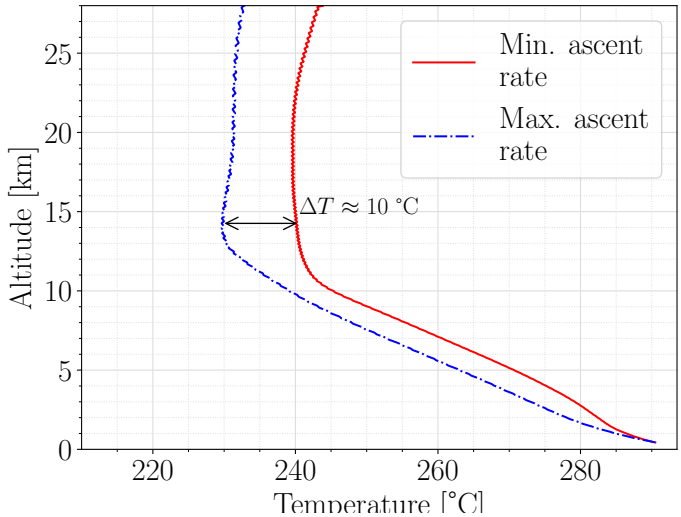

Figure 3.43: Influence of the ascent rare onthe payload temperature. Maximum ascent rate environment, (dot-dashed blue line); minimum ascent rate environment (solid red line).

There is a remarkable cooling of 10 °C, between 12-17 km in the case of maximum ascent rate. This fact is explained by the extra convective effects due to the combination of the lower air temperature and greater relative velocity. Once the troposphere is exceeded, as the convective losses effects decrease, and the variation of the radiative losses along the altitude is similar, (see Figure 3.45), the plate temperature difference remains almost constant.

Another interesting result comes from the comparison of the incoming radiative thermal loads ($\dot{Q}_{load} = \dot{Q}_S + \dot{Q}_A + \dot{Q}_E$), absorbed by the payload. In Figure 3.44 it is represented the relevance of each radiative thermal load in each case. The OLR ($\dot{Q}_E$) dominates the radiative thermal loads until the troposphere is exceeded, where the solar radiative load becomes more relevant.

Regarding the heat losses, ($\dot{Q}_{losses} = \dot{Q}_{conv} + \dot{Q}_{rad}$), it is also interesting the comparison between the heat convective, $\dot{Q}_{conv}$, and the infrared heat radiative losses, $\dot{Q}_{rad}$, during the ascent phase, defined as:

$$\dot{Q}_{conv} = -A_{PL} h \left(T - T_a\right), \tag{3.54}$$

$$\dot{Q}_{rad} = \dot{Q}^{IR}_{out} - \dot{Q}_{sky}, \tag{3.55}$$

The impact of the ascent rate in the relative contribution of the convective and radiative losses are shown in Figure 3.45. In the maximum relative velocity case, the relevance of the convective

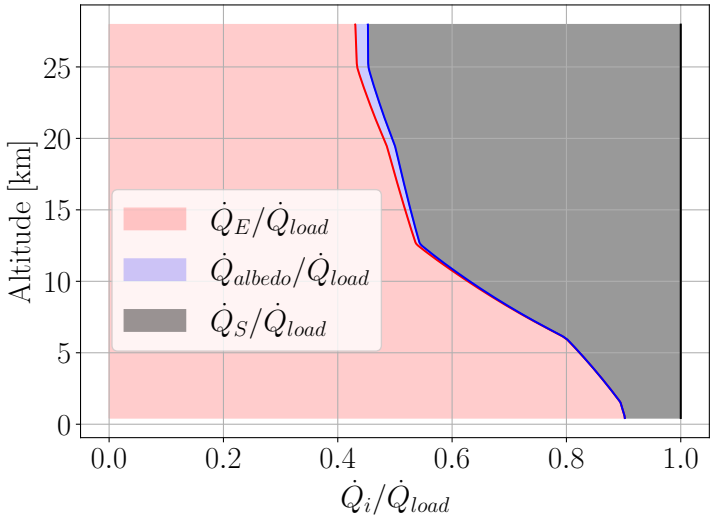

(a) Thermal environment of minimum ascent rate.

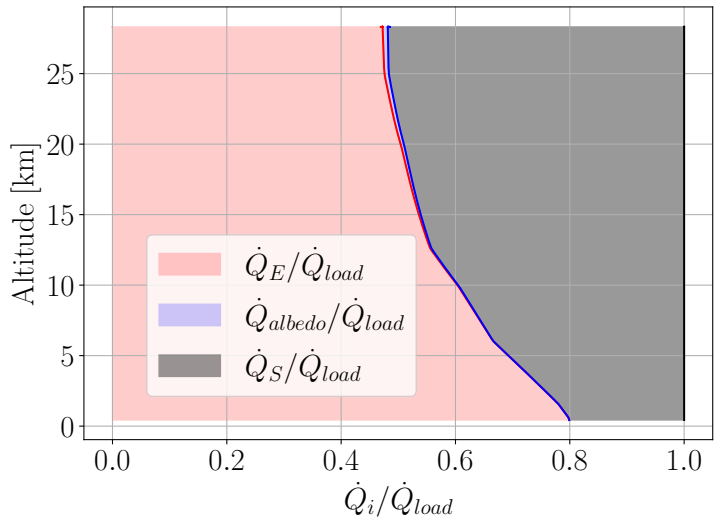

(b) Thermal environment of maximum ascent rate.

Figure 3.44: Comparison $\dot{Q}_i/\dot{Q}_{load}$, with $\dot{Q}_{load} = \dot{Q}_S + \dot{Q}_A + \dot{Q}_E$. $\dot{Q}_E/\dot{Q}_{load}$, (magenta region); $\dot{Q}_A/\dot{Q}_{load}$, (blue); $\dot{Q}_S/\dot{Q}_{load}$, (grey).

heat losses in the payload is even twice compared to the minimum relative velocity case below the tropopause. Once the tropopause is passed, in the both cases the radiative losses reach more relevance. In fact, once the float altitude is reached, as the relative wind speed is almost null and the air becomes thinner, the radiative heat losses virtually drive the thermal behaviour of the payload.

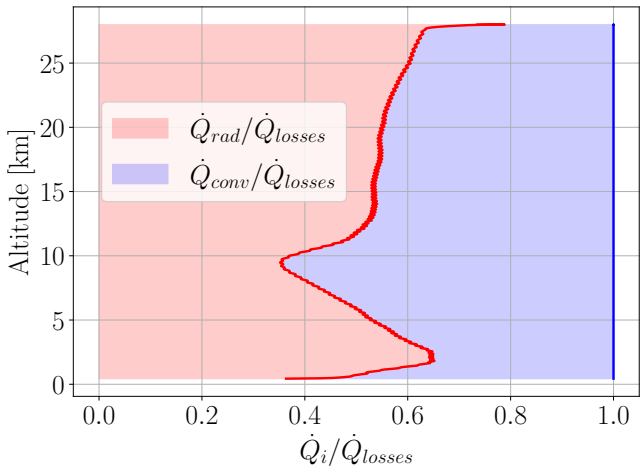

(a) Thermal environment of minimum ascent rate.

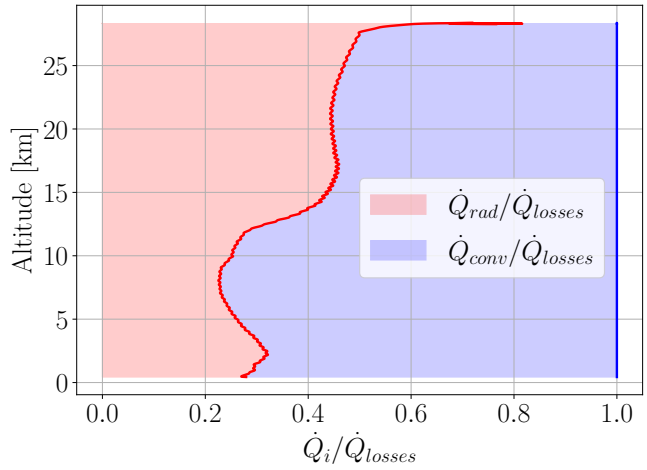

(b) Thermal environment of maximum ascent rate.

Figure 3.45: Comparison $\dot{Q}_i/\dot{Q}_{losses}$, with $\dot{Q}_{losses} = \dot{Q}_{conv} + \dot{Q}_{rad}$. $\dot{Q}_{rad}/\dot{Q}_{losses}$, (magenta region); $\dot{Q}_{conv}/\dot{Q}_{losses}$, (blue).

Chapter 4. Case study. TASEC-Lab

An experiment called TASEC-Lab (Thermal Analysis Support and Environment Characterization Laboratory), which has been designed, manufactured and flown in a stratospheric balloon mission. In this chapter, the ascent phase thermal behaviour of this experiment is presented, which has been predicted following the methodology described in chapter 3, and compared to the flight data.

4.1 TASEC-LAB

TASEC-LAB is an experiment composed of several instruments that aims at characterizing the convective heat transfer during a stratospheric flight [63] on a heated flat plate. To reach the mission objective, it is divided into three subsystems: the Attitude Determination Lab, the Environmental Lab, and the Heat Transfer Lab. The main objective of the Attitude Determination Lab is to gather the orientation, the acceleration, and the global position of the balloon-gondola system by using an Inertial Measurement Unit (IMU) and a Global Positioning System (GPS) sensor. The Environmental Lab is in charge of recording the air pressure and the horizontal relative wind speed during the mission through a pressure sensor and a cup anemometer, respectively [107]. The Heat Transfer Lab (HTL) holds an experiment where the temperature of a heated plate, its surrounding walls, and the surrounding air are measured in order to estimate the convective heat exchange.

4.1.1 TASEC-LAB structure.

The structure of TASEC-LAB follows the same philosophy as Cubesats [108], using COTS and with some differences with regard to the 3U standard. It is divided into three cavities by two non-equispaced aluminum trays, as shown in Figure 4.1. In the first cavity, the Electrical Power Subsystem (EPS) is located, consisting of the battery and the DC/DC converters [109], [110]. In the second cavity, the On-board Computer (OBC), all the electronics, the Attitude Determination Lab, and the MOSFETS for controlling the power dissipation of the heaters, are included. Finally, in the third cavity, the HTL is located. The total envelope of TASEC-LAB is 130 mm$\times$130 mm$\times$330 mm. The closure panels and the beams for stiffness are made up of aluminum.

4.1.2 Heat Transfer Laboratory

The HTL contains one heated horizontal aluminum plate with 25 mm $\times$ 50 mm $\times$ 1 mm dimensions. The heater employed is a silicon heater [111] with a power rating of 1.25 W. As the main objective of this experiment is to estimate the convective dissipation in the aluminum plate, it is required to decouple it radiatively and conductively as much as possible from the environment to reduce the thermal uncertainties. The radiative thermal exchange is minimized by covering both the heater and the plate faces with low a IR emissivity aluminum tape. As shown in Figure 4.2, the conductive heat transfer is also minimized using a Delrin mounting, which is a material with a low thermal conductivity.

To quantify the convection, the temperature of the plate, the surrounding walls, and the surrounding air should be measured. Five TC74s [112] (digital sensors) have been used to measure the surrounding walls temperature, and six PT1000s [113] (thermistors) have been used to measure the temperature of the plate and the surrounding air (see Appendix A). The selection criteria used for the temperature sensors positioning is based on considering the potential temperature gradients in the air inside the box. For this reason, the air temperature away from the plate, both vertically (above and below) and horizontally, is measured. The sensors have been mounted on ABS supports. In order to evaluate the influence of the flight dynamics on the thermal behaviour of the HTL, the air inside the experiment is coupled to the atmospheric air through 4 apertures of 10 mm $\times$ 1 mm located in the top closure panel, small enough to avoid a relevant radiative thermal load to the heated plate. This configuration allows a mass exchange between the inner air and the outer air of the cavity as a function of the ascent rate, as is explained in section 4.2.

Two operational modes for the heated plate was considered during the flight: ascent and float.

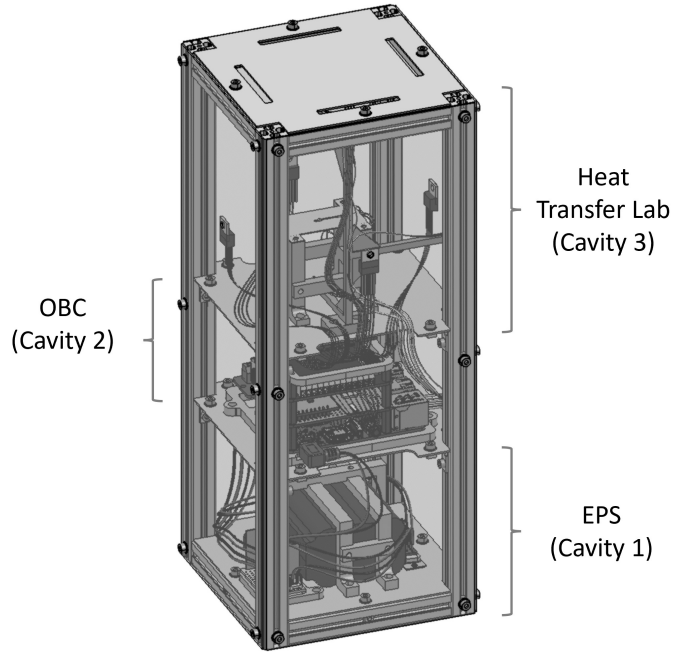

(a)

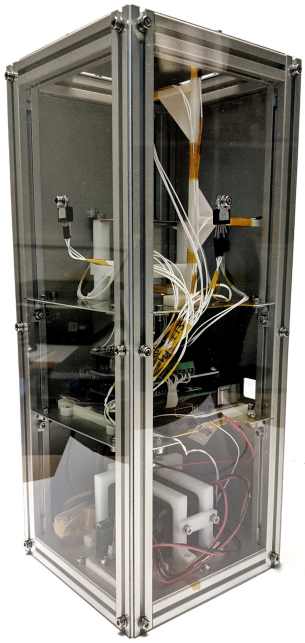

(b)

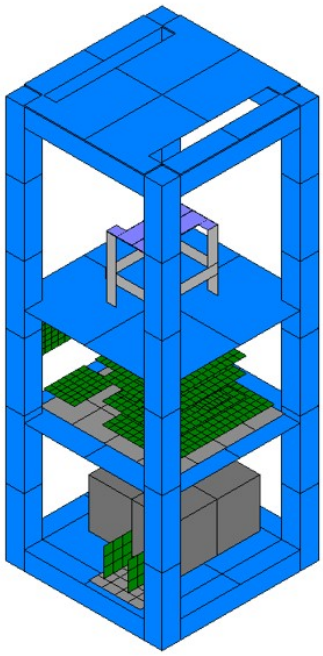

(c)

Figure 4.1: TASEC-LAB general overview. (a) CAD TASEC-LAB general overview (closure panels are removed), (b) TASEC-LAB general overview (aluminum closure panels are replaced by methacrylate), (c) ESATAN-TMS GMM (closure panels removed) (see section 4.2).

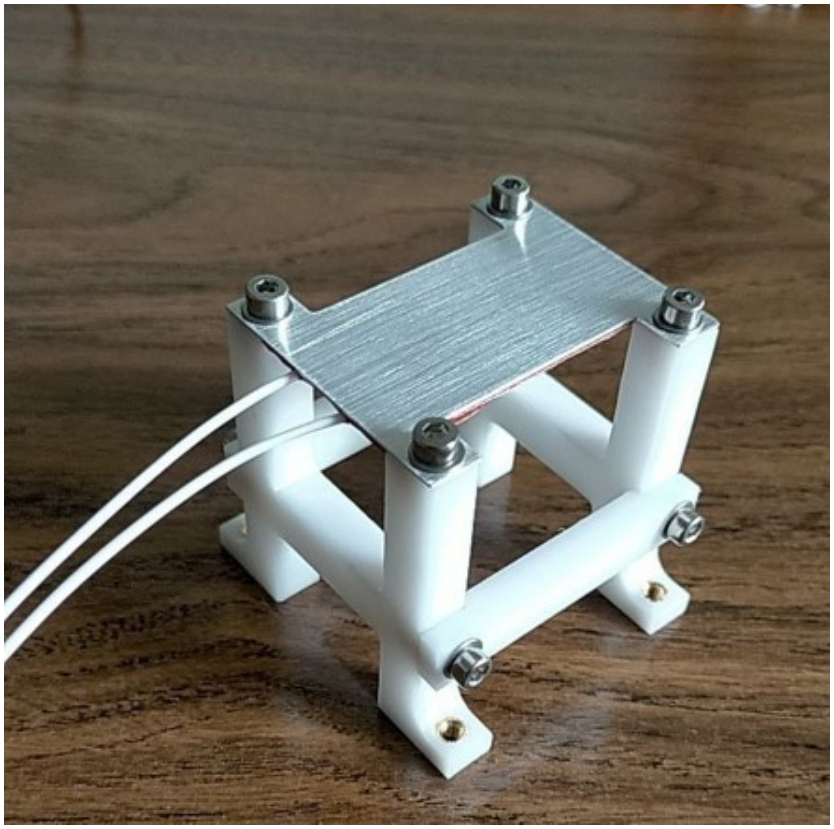

Figure 4.2: Delrin support of the heated plate.

During the ascent phase, a 0.8 W constant heat power is dissipated until the tropopause is reached, and once the tropopause is exceeded, the power dissipation at the plate is reduced to 0.6 W. At the float phase, two different power modes were also established, but unfortunately, due to military restrictions (see subsection 4.1.3), the float phase was not reached. Besides, a safe mode was considered in order to limit the power dissipation of the heated plate should the temperature difference between the plate and the surrounding air reach values above 75 °C (in order to reduce uncertainties during the model correlation).

4.1.3 Launch campaign

The launch took place from the military airport of León (Spain) on 16th July 2021 at 7.30 am LT (UTC+2). TASEC-Lab reached the stratosphere onboard a gondola supplied by the company B2Space [114], together with another experiment from Universidad Alfonso X el Sabio (Madrid, Spain), as shown in Figure 4.3.

The ascent phase lasted approximately one hour and the balloon reached an altitude of 17 km.

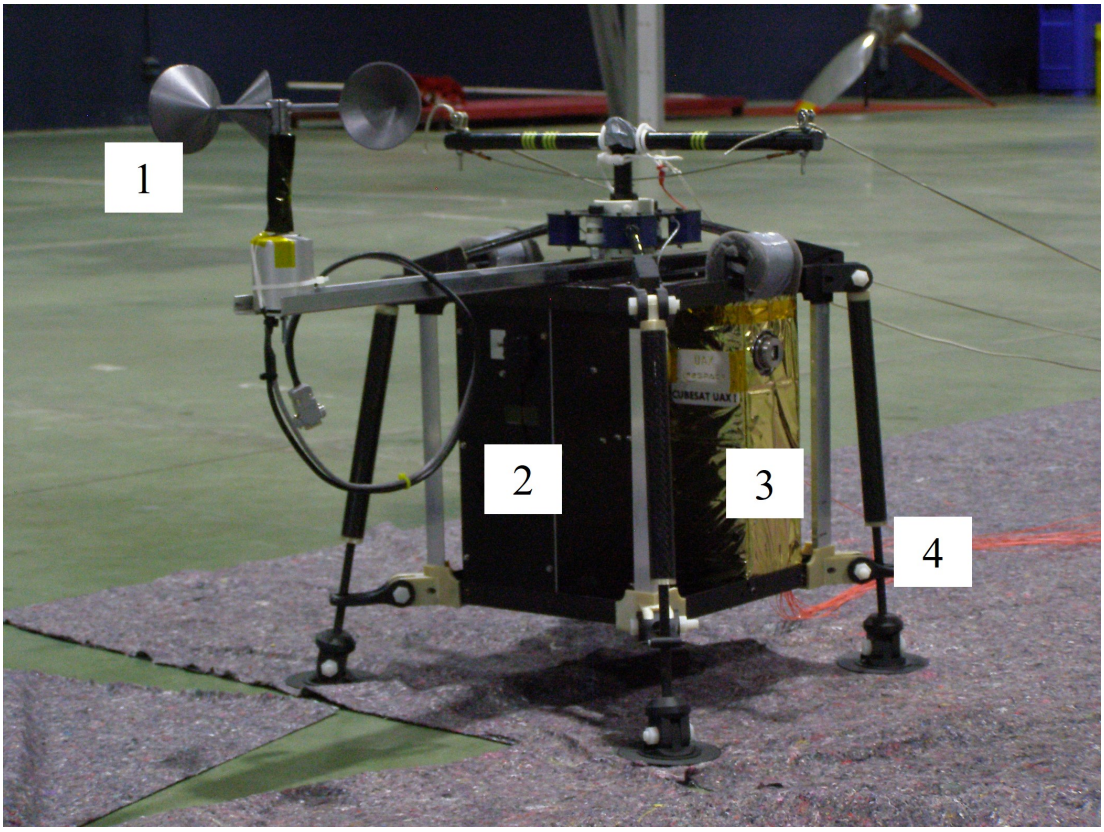

Figure 4.3: TASEC-Lab onboard the gondola minutes before the lift-off. Anemometer (1); TASEC-Lab (2); Alfonso X el Sabio (3) experiment; Gondola bars support (4).

However, due to the wind direction, the balloon entered an area that the launch day was restricted by Spanish authorities (military manoeuvres) so the balloon film was pricked and the parachute was deployed, preventing the experiment from reaching the float phase. During the descent phase, the signal was lost but data up to 5 km of altitude was recorded. Despite the typical altitude of Long Duration Balloon (LDB) was not reached (around 40 km), relevant information was obtained and it is analysed here. The most relevant temperature measurements during both the ascent and the descent phases, together with the altitude and the power of the HTL heated plate, are shown in Figure 4.4a. In addition, the ascent rate, the horizontal relative wind speed measured by the anemometer [107] and the air pressure, are also shown in Figure 4.4b.

Regarding the velocities shown, due to the gondola was not perfectly balanced, there might be a swinging motion, and therefore, the raw output data of the anemometer, which is the frequency of the pulses generated by the cup's rotation (which can be visualized in Ref. [107]), took into account both, the contribution of this swinging motion and the horizontal relative wind speed. Before the tropopause region, it is smaller than the ascent rate, however, from the tropopause, it reaches up to twice or even more the magnitude of the ascent rate, due to the combination of the

jet streams at this altitude and the swinging motion. This assumption could have been validated with IMU data flight, but unfortunately, the recording data was corrupted.

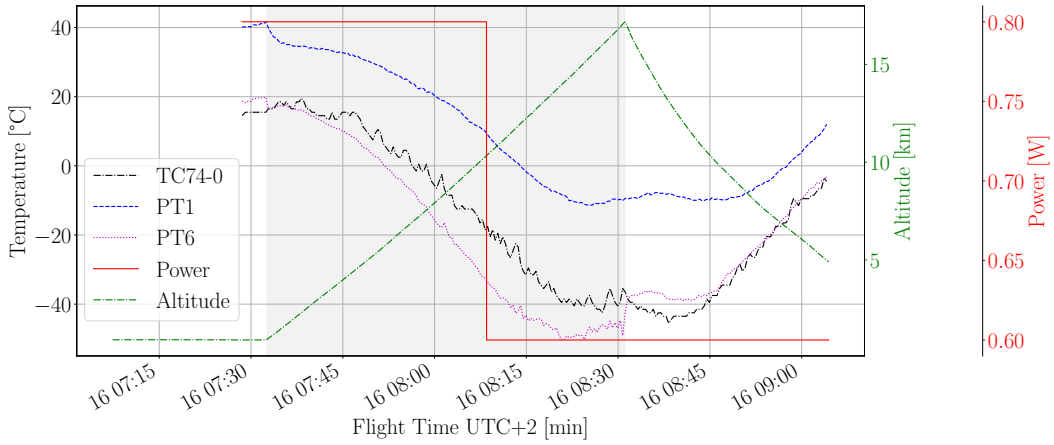

(a)

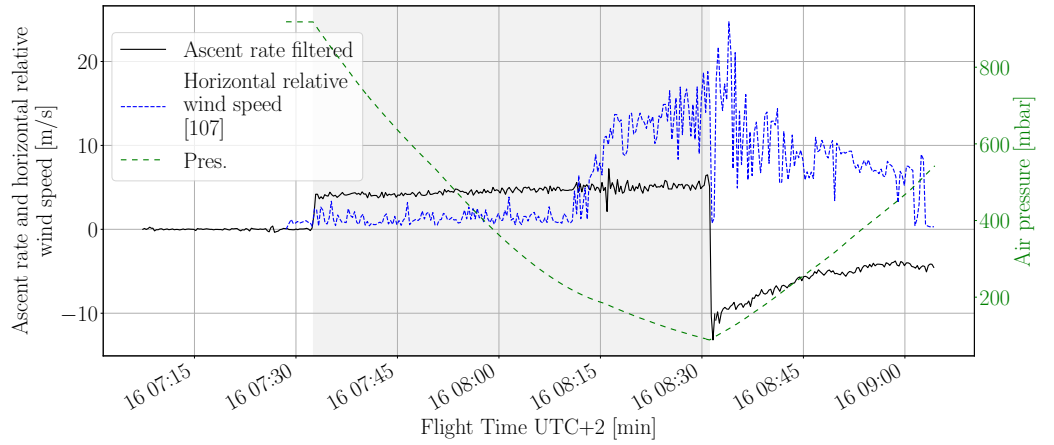

(b)

Figure 4.4: TASEC mission flight measurements (ascent phase is shown in a grey background), as a function of time during the flight. (a) Temperature measurements TC74-0 (dot-dashed black line); PT1, heated plate (dashed blue line); PT6, HTL cavity inner air, (dotted magenta line); HTL heated plate power dissipation (solid red line); altitude (dot-dashed green line).
(b) Filtered ascent rate (solid black line); horizontal relative wind speed (dashed blue line) [107]; atmospheric air pressure (dot-dashed green line).

Regarding the temperature measurements, there is a decreasing tendency until the balloon film was pricked and the parachute deployed due to the combination of the relative wind speed and the low air temperature. During the descent phase, as the experiment was shielded by the bottom of the gondola, and the air temperature was increasing, the temperature measurements show

an increasing tendency. It is also remarkable that due to the spin motion of the gondola, the incoming solar radiation at the HTL closure panels varied, causing the oscillations of the HTL inner wall temperature measurements (TC74-0 sensor).

4.2 Thermal modelling

To predict, compare and correlate the convective heat exchange with the flight data (subsection 4.3.3), a Geometrical and Thermal Mathematical Model of TASEC-Lab has been built in ESATAN-TMS [115].

The GMM developed, together with the CAD model, is shown in Figure 4.1. Only relevant geometries in terms of radiative exchanges have been represented. The GMM of the heated aluminum plate consists of four thermal nodes on the top face, whereas the heater underneath is also modeled with another four thermal nodes. These nodes are conductively coupled between them and with the supporting tray through the Delrin support structure.

The free convective heat transfer is modeled using semi-empirical correlations (see chapter 2) to define a linear conductance coupling, G_L, between each element and the corresponding air thermal node (one per cavity). Therefore, in each cavity, the air thermal node is linearly connected with every element in the cavity.

In order to obtain the transient temperature response during the ascent phase it is also necessary to correctly define the thermal capacity of each air thermal node. To do so, its value has been parameterised considering the volume of each cavity and the air pressure as a function of the altitude.

In addition to that, the outer elements are thermally coupled to the free air due to the forced convection that appears during the ascent phase, following the Newtons' law of cooling:

$$\dot{Q}_{conv} = -h_F A(T - T_{amb}), \tag{4.1}$$

where h_F is the average forced convection heat transfer coefficient, which depends on the element, and the free air temperatures, the geometry of the surface element and the free air relative velocity (for the outer elements), as has been described in chapter 2.

Then, the coefficient h_F is obtained from the Nusselt number, Nu, based on forced convection thermal correlations [39], which are defined as a function of the Reynolds, Re, and Prandtl, Pr,

dimensionless numbers, $\mathrm{Nu} = f(\mathrm{Re}_{l_c}, \mathrm{Pr})$. The Reynolds number is computed following (2.15), based on the air properties evaluated at the film temperature as described in section 2.5.

Once the Reynolds and the Prandtl numbers are calculated, the Nusselt number and then the forced average convection heat transfer coefficient can be evaluated. For the plates parallel to the flow, the correlation used according to [39] is:

$$\mathrm{Nu}_F = 0.68 \cdot \mathrm{Re}_{l_c}^{1/2} \cdot \mathrm{Pr}^{1/3}, \qquad \text{for } \mathrm{Pr} > 0.6. \tag{4.2}$$

For the plates perpendicular to the flow, the correlation used, according to [39], are:

$$\mathrm{Nu}_F = 0.228 \cdot \mathrm{Re}_{l_c}^{0.731} \cdot \mathrm{Pr}^{1/3}, \qquad \text{for } \mathrm{Pr} = 0.7 \text{ and } 4 \cdot 10^3 < \mathrm{Re} < 1.5 \cdot 10^4. \tag{4.3}$$

Furthermore, there is a mass exchange between the inner air of the HTL cavity and the outer air through the four apertures in the top closure panel. This exchange is introduced in the thermal model as a linear conductive coupling as follows:

$$G_L = \dot{m} \cdot c_p, \tag{4.4}$$

where c_p is the specific thermal capacity of the air, and $\dot{m}$ is the mass flow rate, defined as

$$\dot{m} = \rho \cdot A \cdot u, \tag{4.5}$$

where ρ is the air density, A is the aperture area, and u is the velocity of the air.

It is possible to obtain the value of c_p from:

$$c_p = \mathrm{Pr} \cdot \frac{k}{\mu}, \tag{4.6}$$

As above mentioned, the thermal conductivity, k, the Prandtl number, Pr, and the dynamic viscosity, μ, are obtained in terms of the film temperature, T_{m}. In this case, T_{m} is defined as the average of the inner air thermal node temperature and the diffusive node temperature, in Kelvin).

In the pressure range where scientific ballooning [11] takes place, the dependence of the thermal conductivity, the Prandtl number, and the dynamic viscosity, with regard to the air pressure can be considered negligible.

4.3 Thermal analysis

With the objective of developing an accurate thermal design, it is first necessary to define the thermal cases to be analysed. Three thermal cases are defined during the ascent phase, the Hot Operational Case (HOC), the Cold Operational Case (COC) and the Launch Operational Case (LOC). It is expected that the temperature measurements during the flight will be located inside a temperature envelope defined by the Hot and Cold Operational Cases, since they use the hottest and coldest worst-case thermal environmental conditions based on real-data observations. In contrast, the Launch Operational Case, as is used to compare the thermal model results with the flight data, is obtained after the flight, taking into account real environmental data of the launch date and location.

The launch window offered by B2Space was defined as the first twenty days of July 2021 at day times ensuring sunlight at the launch base. Hence, a study of local data in the neighbourhood of the launch area (N43°35′19′′ W05°39′22′′) during the launch windows of the previous two years was performed to define the HOC and COC environmental conditions, not only for the radiative but also for the convective parameters, following the methodology described in section 3.3. Once this data was statistically processed, profiles of each parameter as a function of the altitude were obtained taking into account the thermal characteristics of the TASEC-Lab experiment (black painted in the external surfaces).

4.3.1 Radiative thermal environment

The Hot Operational Case for the ascent phase is defined considering the 90^{th} percentile of the environmental conditions as well as the minimum SZA evolution. In other words, the ascent phase would take place when the Sun reaches the upper culmination. This occurs at 14:00 (UTC+2) as shown in Figure 4.5. The Cold Operational Case for the ascent phase is defined considering the 10^{th} percentiles of the environmental conditions as well as the maximum SZA ensuring sunlight. This occurs defining the launch time at 7:30 am (UTC+2).

As was explained in subsection 4.1.3, TASEC-Lab launch started at 7:30 am. Therefore, an additional case (Launch Operational Case) has been considered after the flight also using CERES data retrieved for the same location and time where and when the flight took place. As the launch took place at the same time of the day that defines the coldest conditions, it is expected to obtain a closer behavior to this one rather than to the hottest profile.

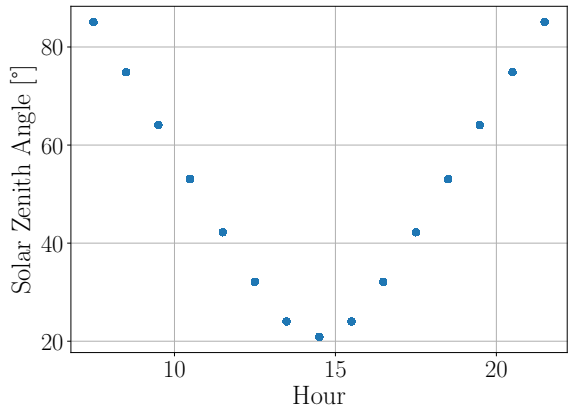

Figure 4.5: Variation of the SZA along the daytime (UTC+2) [75].

The parameter profiles for Hot, Cold and Launch Operational Cases are shown in Figure 4.6. The albedo coefficient correlation with the OLR [16] can be observed in Figure 4.6c and Figure 4.6d, where it is clearly shown that the greater the albedo, the lower the OLR.

4.3.2 Convective thermal environment

Regarding the convective parameters, the air temperature and the air pressure are considered, and therefore the air density, as well as the ascent rate and the horizontal relative speed with the wind. The air temperature has been obtained from the ECMWF data [71], where local temperature data is available at different pressure levels for a grid in latitude and longitude, where the pressure levels can be converted into altitude using Ref. [88], as described in section 3.3. Values that define the Hot, Cold and Launch Operational Cases are obtained by performing a statistical study. The air temperature profiles are shown in Figure 4.6a.

Regarding the ascent rate, considering the evolution of the radiative and convective parameters, the geometrical-thermal-dynamic model described in section 3.4 has been used to predict the evolution in the ascent phase. In addition, the horizontal relative wind speed for the Hot Operational Case has been considered null whereas for the Cold Operational Case, data from ECMWF has been used together with the dynamic model. As pointed out in [107], the characteristics of this dataset, where hourly average values are used, induce to underestimate the relative wind speed during the last part of the TASEC-Lab ascent phase. After the flight, it was decided to include the flight measurements obtained in [107] for this component in the Launch Operational Case. Both, the ascent rate and the horizontal relative wind speed defined for the Hot, Cold and Launch Operational Cases are shown in Figure 4.7.

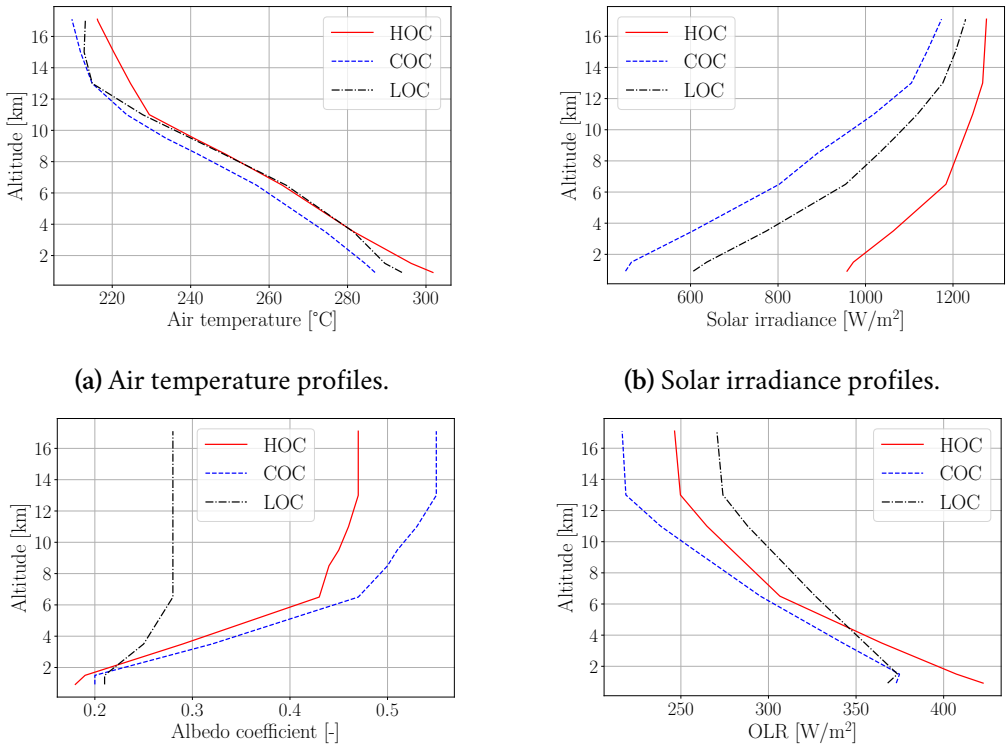

(a) Air temperature profiles.

(b) Solar irradiance profiles.

(c) Albedo coefficient profiles.

(d) OLR profiles.

Figure 4.6: Comparison between thermal parameter vertical profiles in several operational cases: Hot Operational Case, HOC (solid red line); Cold Operational Case, COC (dashed blue line); and Launch Operational Case, LOC (dot-dashed black line).

4.3.3 Flight correlation

Once the conductive, radiative and free convective losses have been estimated and validated with the thermal model, the Hot and Cold Operational Cases are analysed in order to define an envelope of temperatures which the flight measurements should be inside. To consider the shadow effect generated by the gondola and the other experiments onboard during the flight, the GMM of the gondola and the geometrical envelope of the other experiments are also included, as shown in Figure 4.8.

After the flight, local data for the time and the area where the flight took place is used to correlate the air mass exchange and the forced convection in the HTL cavity. The air mass exchange is computed as a function of the relative air velocity, as was explained in section 4.2. This value was adjusted as a function of the ascent rate in order to correlate the heated plate temperature with the flight data. The air velocity obtained in the cavity corresponds to the 15% of the ascent rate during the whole ascent phase.

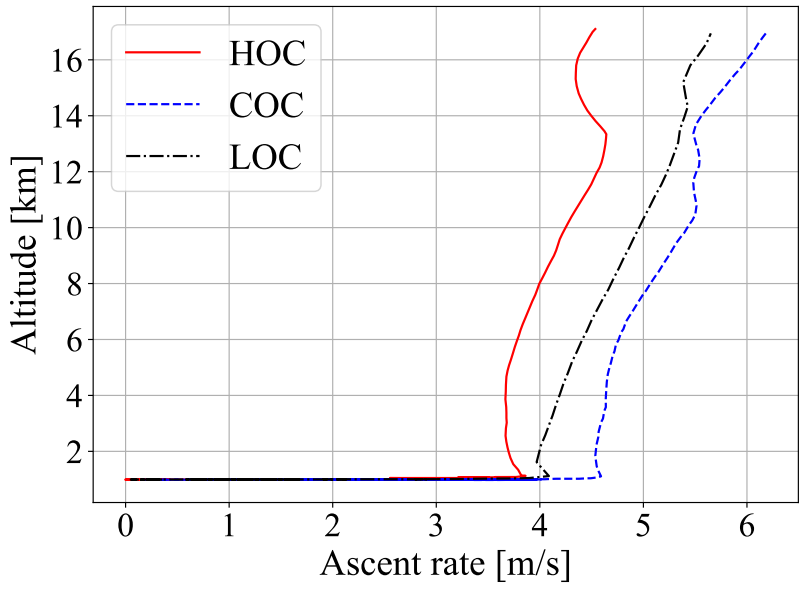

(a) Ascent rate profiles

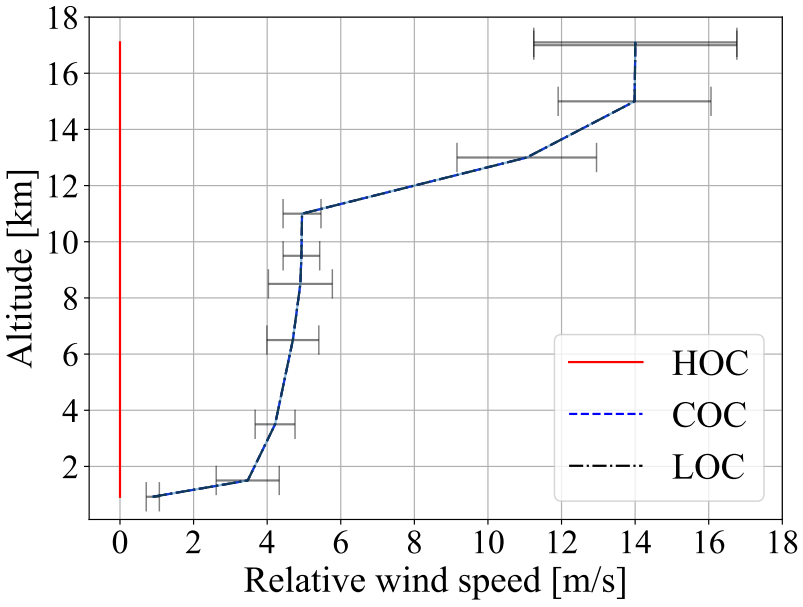

(b) Average horizontal relative wind speed together with the standard deviation [107] profiles.

Figure 4.7: TASEC mission. Comparison between the thermal parameter vertical profiles in several operational cases: Hot Operational Case, HOC (solid red line); Cold Operational Case, COC (dashed blue line); same as Launch Operational Case, LOC (dot-dashed black line).

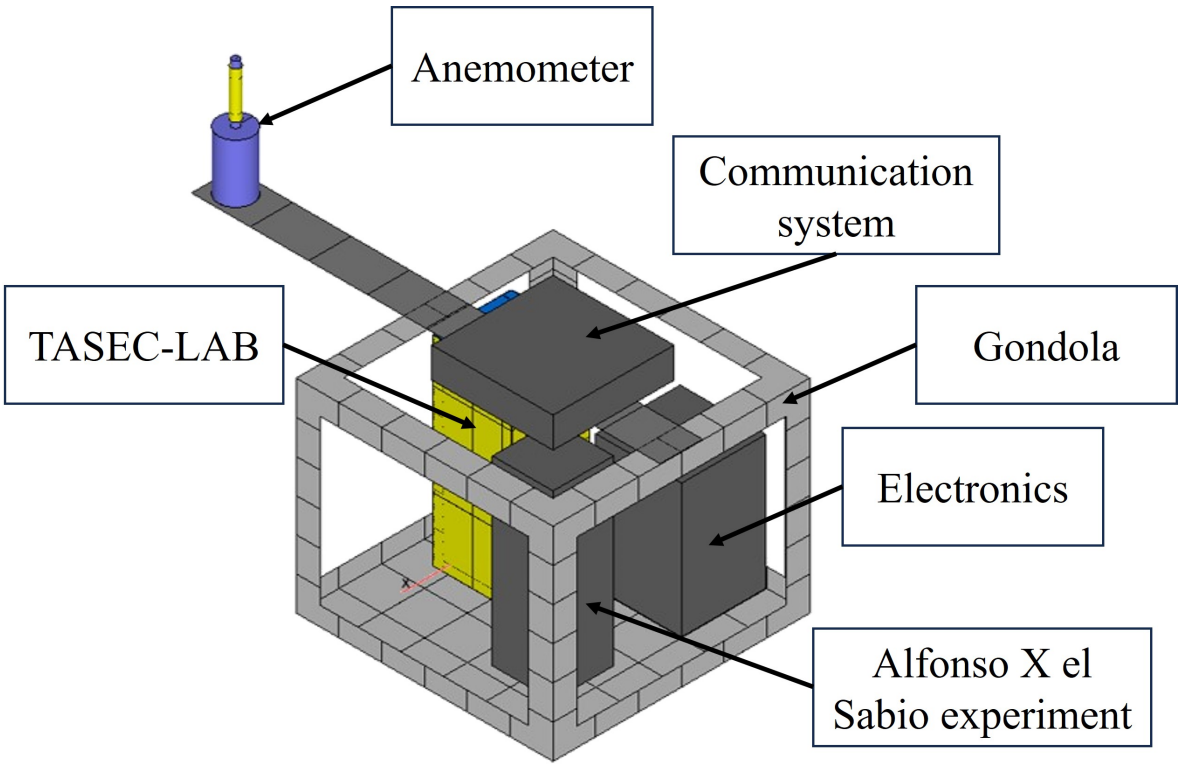

Figure 4.8: GMM of the gondola and the experiments onboard during the flight.

The variation of the temperature of the heated plate as a function of the altitude during the ascent phase is shown in Figure 4.9a. It is remarkable that the measurements are located inside the calculated envelope, and that the flight case is in quite good agreement with the flight data. Another interesting result is the one obtained for the outer HTL wall temperatures. They are exposed to both the outer forced convection and to the radiative thermal loads.

In addition, the temperature of the HTL closure panel Y— is shown in Figure 4.9b. The measured temperatures oscillate along the altitude due to the gondola spin. In the thermal analysis, a fast enough spin is assumed so that average thermal fluxes can be considered in the thermal mathematical model. Hence, the temperatures predicted by the model cannot show these oscillations.

The convective heat transfer coefficient between the HTL heated plate and the air inside the cavity, obtained at LOC is shown in Figure 4.10, where the results for both the free and the forced convective heat transfer coefficient, are shown together with the heat transfer coefficient computed from (2.27) and (2.19), assuming the exponent $n = 3.5$ [39].

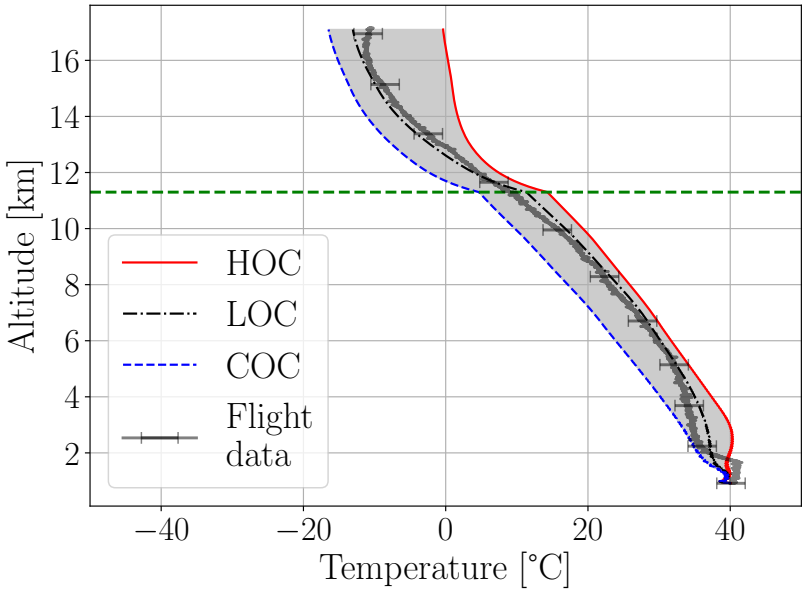

(a) HTL heated plate temperature comparison.

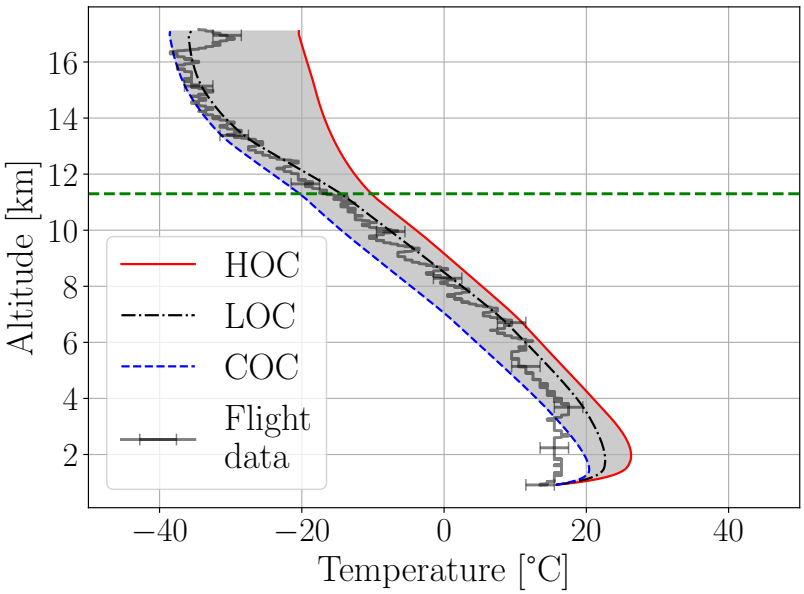

(b) HTL closure panel Y+ temperature comparison.

Figure 4.9: Temperature comparison among simulations and real flight data. Solid red line, Hot Operational Case; dashed blue line, Cold Operational Case; and dot-dashed black line, Launch Operational Case. Dotted grey line, flight data with sensor error bars. Horizontal green dashed line: altitude where the power dissipation of the plate was reduced from 0.8 W to 0.6 W.

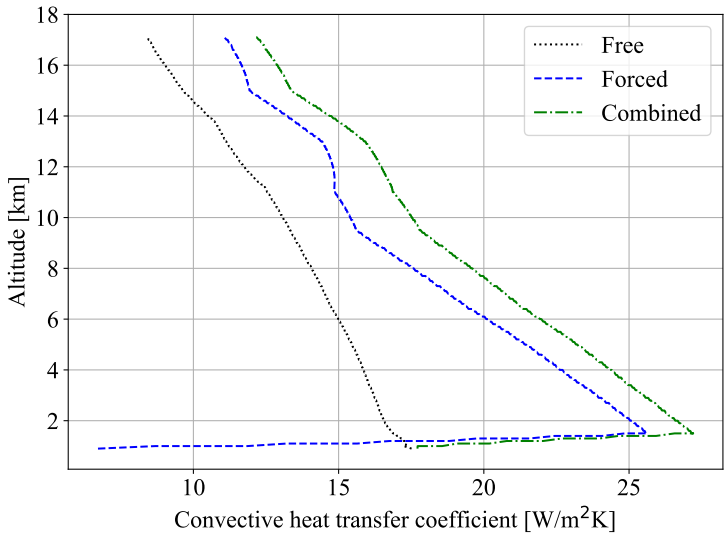

Figure 4.10: TASEC mission. Vertical profile of the convective heat transfer coefficient between the HTL heated plate and the air inside the cavity obtained at LOC. Free convective heat transfer (dotted black line); forced convective heat transfer (dashed blue line); combined convective heat transfer (dot-dashed green line).

Chapter 5. Case study. SUNRISE III

5.1 SUNRISE mission

SUNRISE mission is an international project lead by the Max-Planck-Institut für Sonnensystemforschung (MPS, Göttingen, Germany) with the participation of other European institutes such as Kiepenheuer-Institut für Sonnenphysik (KIS, Freiburg, Germany), Instituto de Astrofísica de Canarias, (IAC, Tenerife, Spain), Instituto de Astrofísica de Andalucía (IAA-CSIC, Granada, Spain), Instituto Nacional de Técnica Aerospacial (INTA, Madrid, Spain), Grupo de Astronomía y Ciencias del Espacio (GACE, Valencia, Spain) and Instituto Universitario de Microgravedad "Ignacio Da Riva" (IDR), Universidad Politécnica de Madrid, (IDR-UPM, Madrid, Spain), and international institutes such as National Astronomical Observatory of Japan (NAOJ, Japan) and The Johns Hopkins Applied Physics Laboratory (APL, Laurel, MD) of USA.

SUNRISE is a balloon-borne telescope whose main scientific objective is the study of the structure and dynamics of the magnetic field in the Sun's atmosphere. It consists of a solar telescope on board a zero-pressure balloon, as other Long Duration Balloon (LDB) scientific missions. Two successful flights took place in 2009 and 2013, both launched in June from the European Space Centre in Esrange, Sweden, because during this time of the year, at high latitudes (summer north pole), in addition to the existence of constant daylight, the trajectory of the balloon can be predicted due to the stable winds. The ascent phase lasted almost 4 hours to lift the balloon to the altitude of the stratosphere (about 37 km). The cruise phase, which begins once the balloon has reached the altitude of the stratosphere, lasts up to 5 days, with the balloon-borne telescope landing in northern Atlantic on both flights, as it is shown in Figure 5.1.

SUNRISE III was launched in the early morning of 10^{th} July 2022. However, due to a mechanical

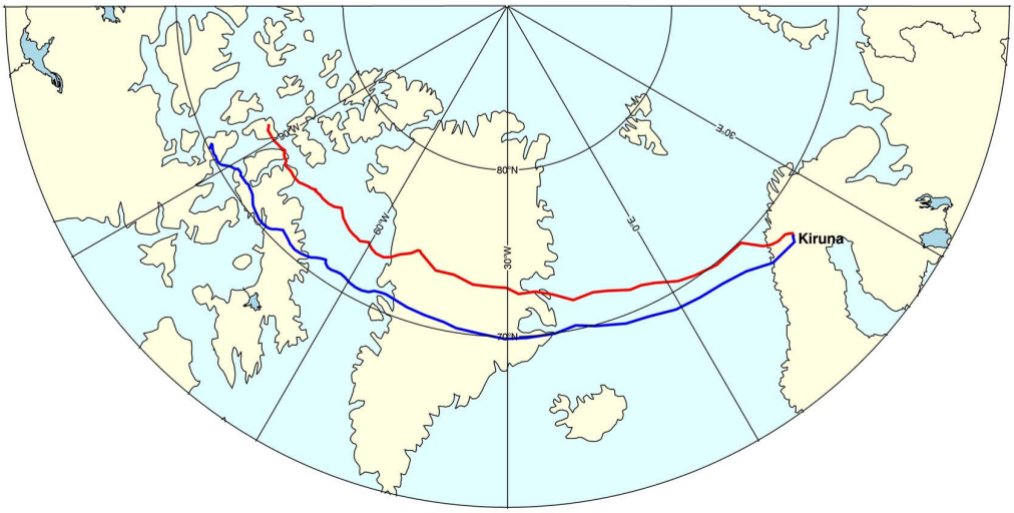

Figure 5.1: The flight trajectory of the 2009 (red curve) and 2013 (blue curve) SUNRISE science flights superimposed on a map of the North Atlantic. The semicircles mark latitudes of 60°, 70°, and 80° [20]. The first flight was launched from Kiruna, June 8, and landed in Somerset Island, June 14. The second flight was launched from Kiruna, June 12, and landed in Boothia Peninsula, June 17.

problem, the telescope was unable to point at the Sun as planned after reaching an altitude of 30 km, making it impossible to obtain scientific data, and the mission was aborted. A re-flight of the observatory is planned for June 2024. In Figure 5.2, it is presented SUNRISE III telescope with its instruments and electronics mounted in the gondola suspended from the launch crane at the balloon launch site.

Although the scientific mission could not be carried out, temperature measurements were taken during the ascent phase, allowing the flight data obtained to be compared with the hot and cold case ascent predictions of the G/TMM developed in ESATAN-TMS, which is shown in Figure 5.3.

5.2 SUNRISE III flight

SUNRISE III lifted off at 1.42 am UTC (3.42 am LT) on 10th July from Esrange, Sweden. The flight ended at 7.05 am UTC (9:05 am LT) of the same day and landed a few minutes later. Hence, the flight lasted less than six hours, with an ascent phase of 3.5 hours, and a cruise phase of less than 3 hours. As already mentioned, the short cruise phase was due to a mechanical failure in the gondola, which prevented the telescope from pointing at the Sun, and thus from obtaining scientific data. The flight trajectory profile followed by the observatory is shown in Figure 5.4.

Figure 5.2: SUNRISE III during the communication test before launching [116].

From an attitude point of view, the ascent phase of SUNRISE III can be divided into two phases. First, the observatory rotates variably at up to about 1 rpm. Second, the observatory stabilizes at an altitude of 30 km. Due to the failure of the break, the telescope was stuck for the whole flight and had a constant elevation of about 60.4° with regard to the horizontal plane. This fact meant that the telescope orientation was not the expected one (it should have been perfectly horizontal until 30 km, when it should have started pointing at the Sun).

To visualise the temperature trends measured by the in-flight temperature sensors, data from the front ring of the telescope, is shown in Figure 5.5. The strong influence of convection until the balloon-borne system overtakes the tropopause can be observed as the temperatures decrease up to about 10 km. Once the tropopause is exceeded, the thermal radiative loads dominate and compensate for the convective heat loss. At about 31 km, the temperature profiles show a trend change. This effect is due to the change in attitude (spinning has stopped). The front ring receives a constant solar heat load and consequently the temperature increases.

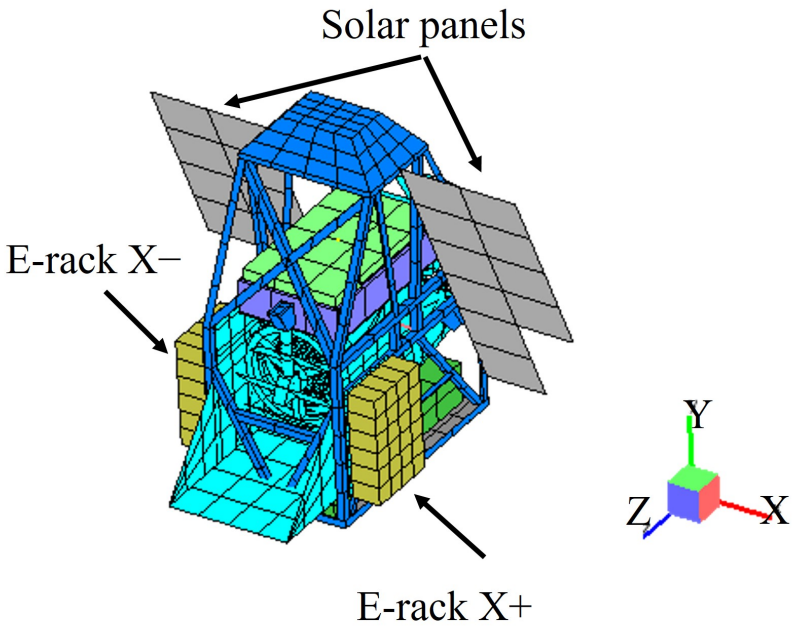

(a)

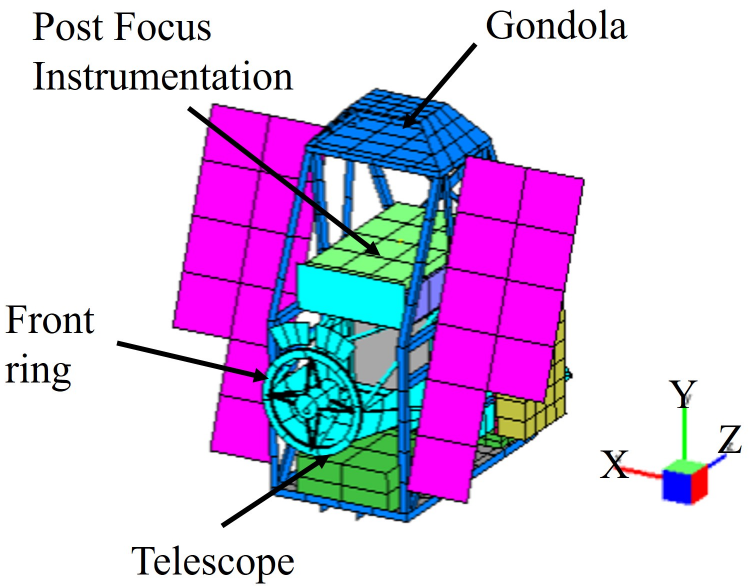

(b)

Figure 5.3: Geometrical Mathematical Model of SUNRISE III. Solar panels, gondola, E-racks, telescope and Post Focus Instrumentation are highlighted. (a) Front view; (b) Rear view.

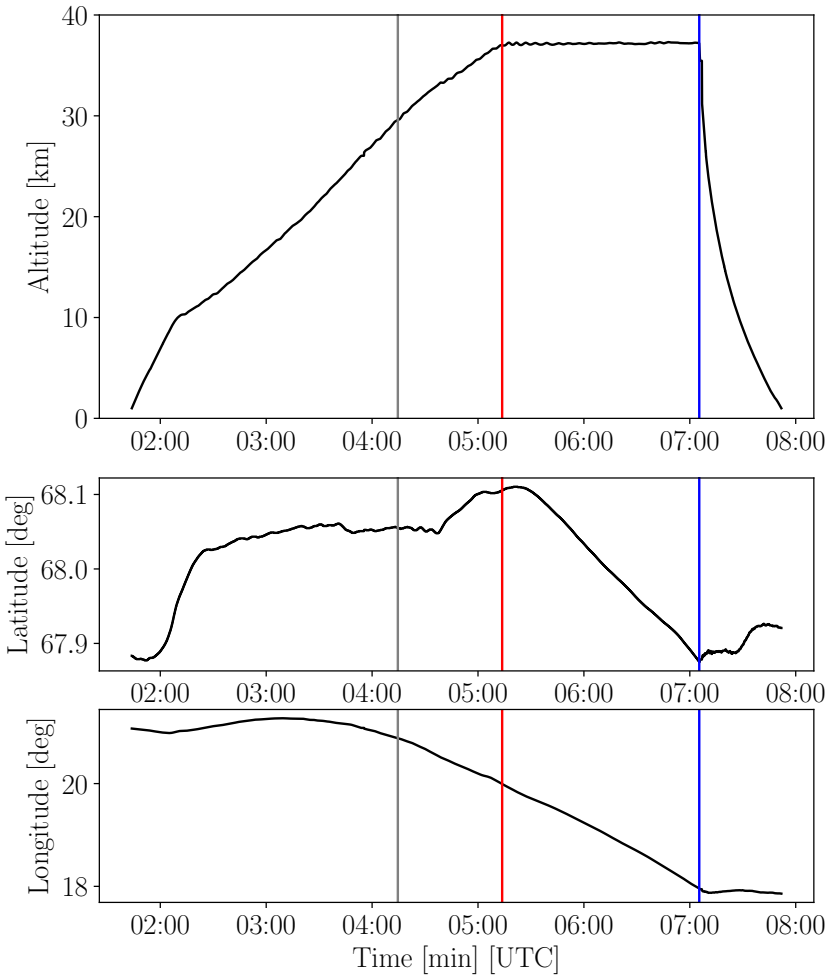

Figure 5.4: SUNRISE III flight trayectory. Vertical grey line, end of the spinning. Vertical red line, end of the ascent phase. Vertical blue line, end of the cruise phase.

5.3 SUNRISE III flight data comparison

Following the methodology described in chapter 3, two cases have been analysed in ESATAN-TMS during the SUNRISE III ascent phase, a hot case (HOC) and a cold case (COC). The hot case thermal environment profiles have been defined based on a minimum SZA (at 10 am UTC), and the cold case thermal environment profiles have been defined based on a maximum SZA (at 21 pm UTC).

From the attitude point of view, the ascent phase can be divided into two stages. Hence, each thermal case uses two radiative cases enchained. The first, with spin around the vertical, where it has been set ten equally spaced orientations to compute an average flux at each orbital position.

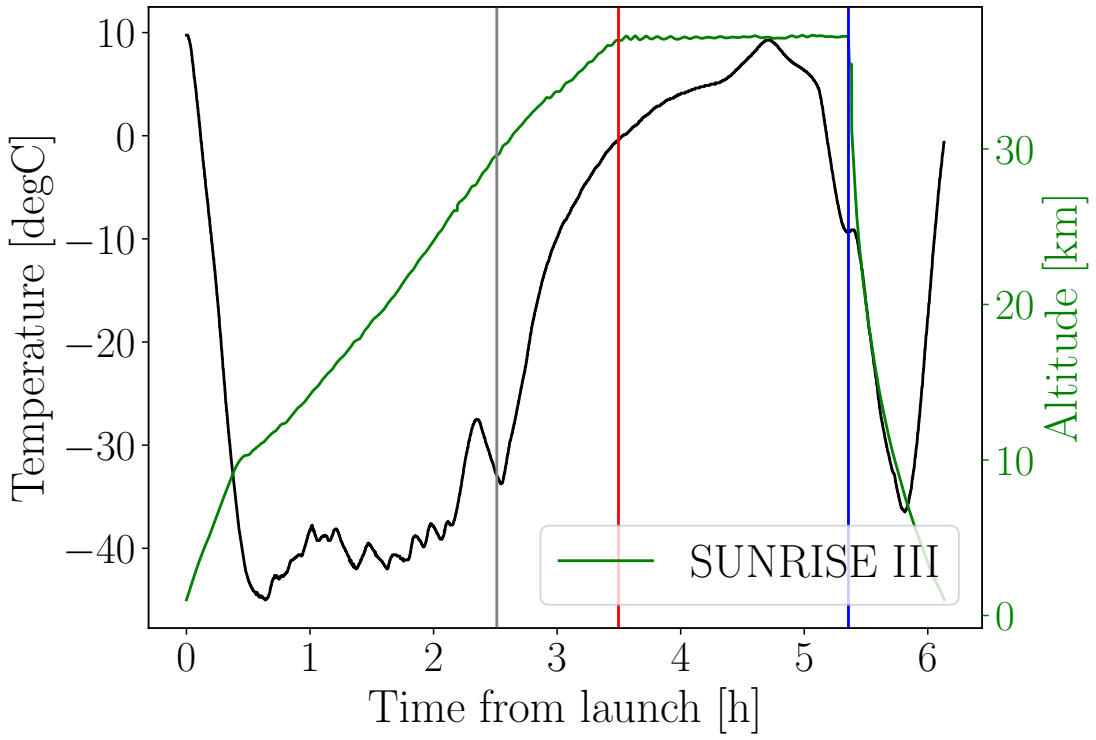

Figure 5.5: SUNRISE III mission. Front ring of the telescope: temperature measured during the flight (black line). Altitude: green line, scale on the right. Vertical grey line: end of the spinning. Vertical red line: end of the ascent phase. Vertical blue line: end of the cruise phase.

The second radiative case, where the spinning is stopped and the $Y+$ axis points to the zenithal direction, and the $Z-$ axis is parallel to the Solar rays (the axes are referred to ESATAN-TMS reference frame shown in Figure 5.3).

The temperature profiles obtained for E-rack+ and E-rack− are compared to those measured during the flight in Figure 5.6. In both subsystems, the flight data is located within the hot and cold case envelopes. Furthermore, the trend of the simulated curves follows the flight data, not only once the spinning stops but also up to an altitude of about 12 km, where convection dominates the thermal behaviour and the temperature decreases. In both E-racks, when spinning stops at about 2.5 h, both simulated and flight temperatures show a change in trend and start to decrease. Note that once spinning is stopped, the E-racks are partially shadowed, reducing the solar thermal loads and, therefore, the temperatures should decrease. Regarding the oscillations showed by the temperature flight data, it is explained as the radiative heat loads change while the gondola is spinning. Since the simulations calculate the heat fluxes at each trajectory position as the average of ten equally spaced orientations, it is not possible to reproduce such oscillatory behaviour.

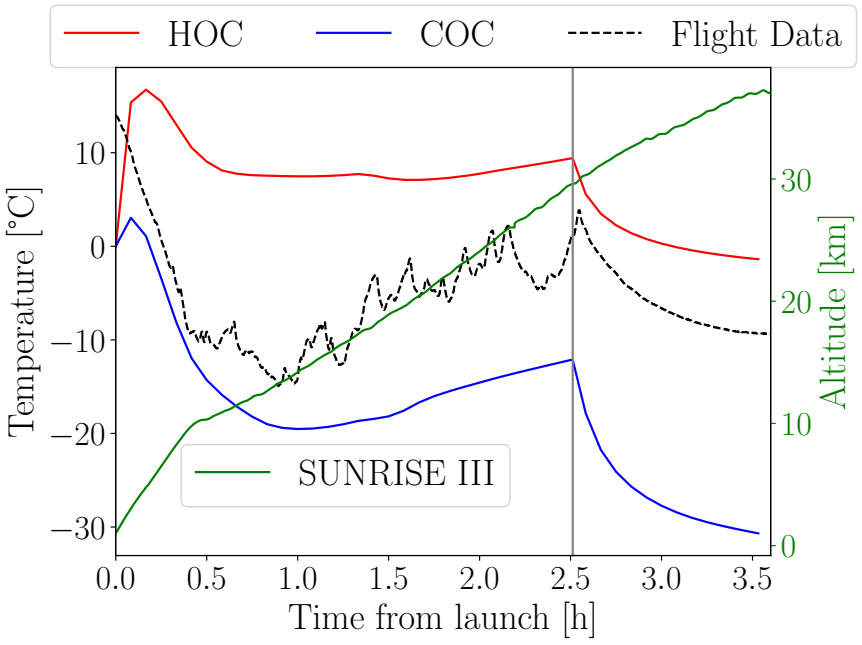

(a)

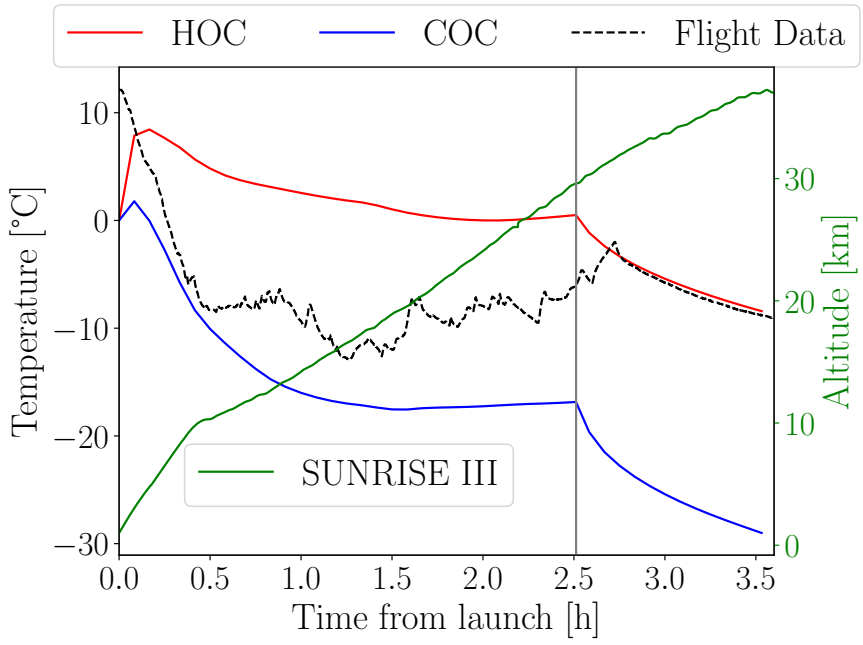

(b)

Figure 5.6: SUNRISE III flight temperature measurements in the E-rack+ (a) and E-rack− (b). Left scale: temperature; right scale: altitude. Vertical grey line: time at which the attitude change takes place; Red line: maximum temperature of the subsystem analyzed at the hot case; blue line: minimum temperature at the cold case. Dashed black line: temperature measured during the flight.

In order to show the relevance of the launch time and site, the maximum and minimum temperatures and the thermal radiative loads on SUSI-O unit [117] radiator (located in the PFI) are shown in Figure 5.7a and Figure 5.7b, respectively.

Due to the high SZA at the cold case (COC), the direct solar load is almost null. This fact explains the temperature difference between the two thermal cases. Regarding the tendency observed after the change of the attitude, at the hot case (HOC) the temperatures increase or remain constant.

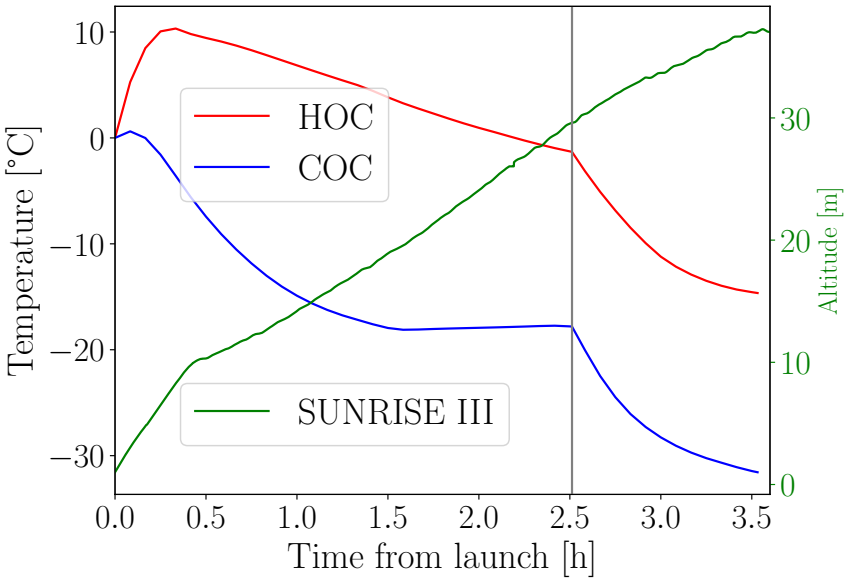

(a)

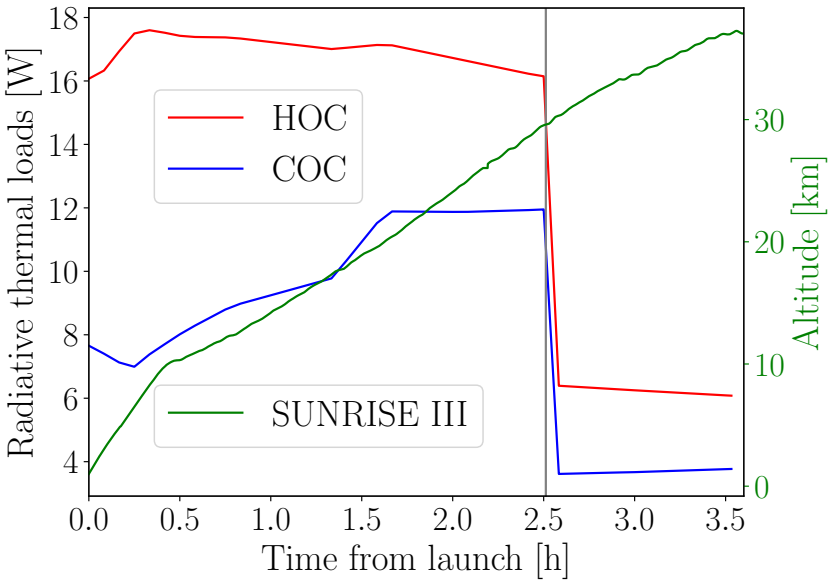

(b)

Figure 5.7: SUNRISE III mission. SUSI-O radiator temperature, and radiative thermal loads absorbed, obtained by simulation. Left scale: temperature; right scale: altitude. Vertical grey line: time at which the attitude change takes place; Red line: the hot case; blue line: cold case. (a) Maximum and minimum temperature. (b) Direct solar, albedo and IR Earth flow absorbed.

Chapter 6. Conclusions and future work

6.1 Conclusions

The main idea presented in this Doctoral Dissertation is that the thermal analysis of a stratospheric balloon- borne payloads should not only account for the uncertainty related to the thermal environment [67] but also consider the uncertainty associated with the ascent rate. Additionally, the crucial parameters for calculating the ascent rate are the system masses and the thermal environment, which include factors such as OLR, albedo, solar irradiance, air temperature, and wind speed. Therefore, it is necessary to perform a transient thermal analysis tailored to each mission, taking into account the specific system masses, balloon type, and characterization of the thermal environment based on the launch site and launch epoch. To do that, this work is based on the use of databases to obtain representative parameters (that define the thermal environment) profiles with altitude, referred to the launch site and the launch window of the mission. In this way, a more realistic assessment of the dynamics of the ascent phase can be performed, and thus, of its impact on the payload temperature. Besides, it is possible to determine the thermal environment conditions that cause the worst case from a thermal point of view. The results obtained from the methodology developed have been applied in real space applications, with a quite good agreement.

Interestingly, the analysis of the thermal behaviour of balloon-borne payloads during the ascent phase is usually a complicated task where many variables should be considered. On the one hand, the relevance of considering the free convective heat transfer in specific situations where conduction and radiation are minimized, even at low pressure, has been pointed out in this work. On the other hand, forced convection during this phase has also a large impact, since the minimum temperatures of the mission may appear while passing through the tropopause. Therefore, to clarify

the contribution of the several mechanisms, an analytical dynamic model of the ascent phase is introduced, the assessment of the influence of the main parameters on the ascent rate is performed, and the relevance of the worst-case selection to achieve a robust thermal analysis is discussed. Also, an experimental validation of the methodology described is provided. This methodology allowed the use of the criteria established in order to develop a complete thermal analysis of a balloon-borne payload flight, considerably reducing the uncertainties associated to the thermal environment definition. However, as the accuracy of the results obtained are strongly dependent on the convective effect implementation in the thermal model, this, implementation has carefully been studied.

In order to improve the existing convective heat transfer models, experimental tests have been performed, obtaining a new empirical correlation, valid in the range $10^{-2} < \mathrm{Ra} < 10^{3}$. Besides the results have been applied to TASEC-Lab mission. In the thermal model developed for the experiment (using the lumped parameters method) the air mass flow between the inner cavity and the environment is also taken into account. By doing so, a good agreement between the thermal model predictions and the flight data measurements is achieved, for instance, the RMSE (Root Mean Square Error) of HTL heated plate temperature is 4.6 °C.

In this work, the complexity of a stratospheric balloon-borne payload thermal analysis during the ascent phase, due to the number and variability of the parameters that affect its thermal behaviour, has been analysed in detail considering worst-case environmental conditions particularized for the launch site and the launch date window. The ESATAN-TMS numerical results have been compared with TASEC-Lab, and SUNRISE III flight data, showing a good agreement. During the most part of the ascent phase, flight data remain inside the temperature envelope defined by the worst-cases calculated using the proposed methodology.

Besides, the influence of the balloon flight dynamics on the thermal behaviour of a generic stratospheric payload has been studied. To do so, a dynamic model has been combined with a geometrical model of the balloon film, the definition of the thermal environment, and the equations that governs the thermal behaviour of payload. An analysis was conducted to examine the impact on the relative velocity of the thermal environment parameters. This analysis aimed to establish an envelope bounded by the maximum and minimum relative velocity profiles. The resulting profiles, along with the corresponding thermal environment values that lead to those limits, are used as input to compute the payload temperature during the ascent phase. This analysis has been applied to the BEXUS programme, and the ascent rate envelope is compared with the real envelope obtained from flight data, showing a good agreement.

As expected, the payload convective losses during the ascent phase were not negligible at all, especially at the troposphere and the tropopause. The simulations performed show a temperature

difference in the payload of 10 °C for the limits of the envelope previously defined.

Therefore, the work developed in this Doctoral Dissertation proposes a new approach to develop the complex thermal analyses of stratospheric balloon-borne payloads during the ascent phase. Amongst the most relevant contributions, recommendations are proposed to define a worst-case conditions tailored to each mission taking into account all the parameters that affect the temperature of the payload, reducing the uncertainties related to the thermal environment and the ascent rate, and therefore, improving the thermal design.

6.2 Future work

The work carried out in the context of this doctoral thesis has made it possible to identify a number of aspects that still need to be studied in a greater depth.

Regarding the aerodynamic model:

- **Determination of the the balloon drag coefficient, C_D.** The drag coefficient has a great impact on the relative speed especially in the first stage (up to the tropopause). In the literature there is no established criterion for its use, and there are several models that fit well to real flight data but with different values of C_D, depending on the balloon size and shape. A detailed wind tunnel study with the different shapes that the balloon takes along its way up to this altitude may provide a new determination of C_D that better fits data. Another option is to use a large database of stratospheric balloon launch data (environment conditions, payload masses, lifting gas mass, trajectory, etc) to obtain a best-fit C_D function.
- **Extend the use of the developed model for flight trajectory prediction and use the tool for mission analysis.** The model developed allows the worst case selection of relative velocity to be investigated for subsequent inclusion in the thermal model. With not a great effort, the model can be adapted for use as a mission analysis tool to simulate the expected trajectory of the balloon, if the thermal environment is defined based on meteorological forecasts, for instance, using the Integrated Forecasting System (IFS) model by ECMWF for use by license holders [118].

Regarding the convection implementation on the thermal modelling:

- **Development of new environmental test for other geometries.** It has been started with the basic geometry of a horizontal flat plate. It is necessary to extrapolate this study to other

geometries such as a vertical plate, a cylinder or several flat plates. In addition, for further generalisation, the effect of the proximity of the cavity walls to the heated plate should be studied, obtaining correlations that take into account the distance from the plate to the wall. This work has been partially started with the project HERCCULES, which was successfully flown onboard the BEXUS 32 mission in September 2023. Data flight will be analysed to define new correlations.

Regarding the whole ascent phase thermal study on stratospheric-borne payloads:

- **Extend the methodology for other stratospheric platforms.** In recent times, there has been a resurgence in the popularity of airships now denoted as High Altitude Pseudo-Satellites (HAPS) [119]–[122]. By carefully adapting the equations defining thermal interactions, the whole study can be transferred to other types of platforms.

Acknowledgements

The author wish to thank ECMWF and AEMET for providing a specific license for the MARS catalogue, specially to Mr Raúl Corredor Asenjo from AEMET.

The author also wish to thank MORABA, DLR, SSC for the BEXUS mission data supplied, specially to Armelle Frenea-Schmidt from SSC.

The author is also very grateful to the entire TASEC-Lab and HERCCULES team for the great work carried out, which has allowed the author to implement the proposed methodology and compare it with real flight missions.

The author wish to thank the whole SUNRISE team, the successful missions have allowed the author to implement the thermal modelling and compare the thermal simulations with real data flight.

Finally, the author wish to thank "Programa Propio de Investigación 2023" from Universidad Politécnica de Madrid for the finnancial support (research stay at INAF-OAS Bologne, publication costs of a paper [123]).

Funding

This work has been supported by the Spanish "Ministerio de Ciencia e Innovación", Projects PID2021-125627OB-C23, PID2021-125325OB-C53, and by Comunidad de Madrid by Project OAPES Y2020/NMT-6427.

Appendix A. TASEC-LAB temperature sensors location and measurements

The location and function of the PT1000 and TC74 type sensors employed for the temperature measurements of the HTL during flight is summarized in Figure A.1 and in Table A.1.

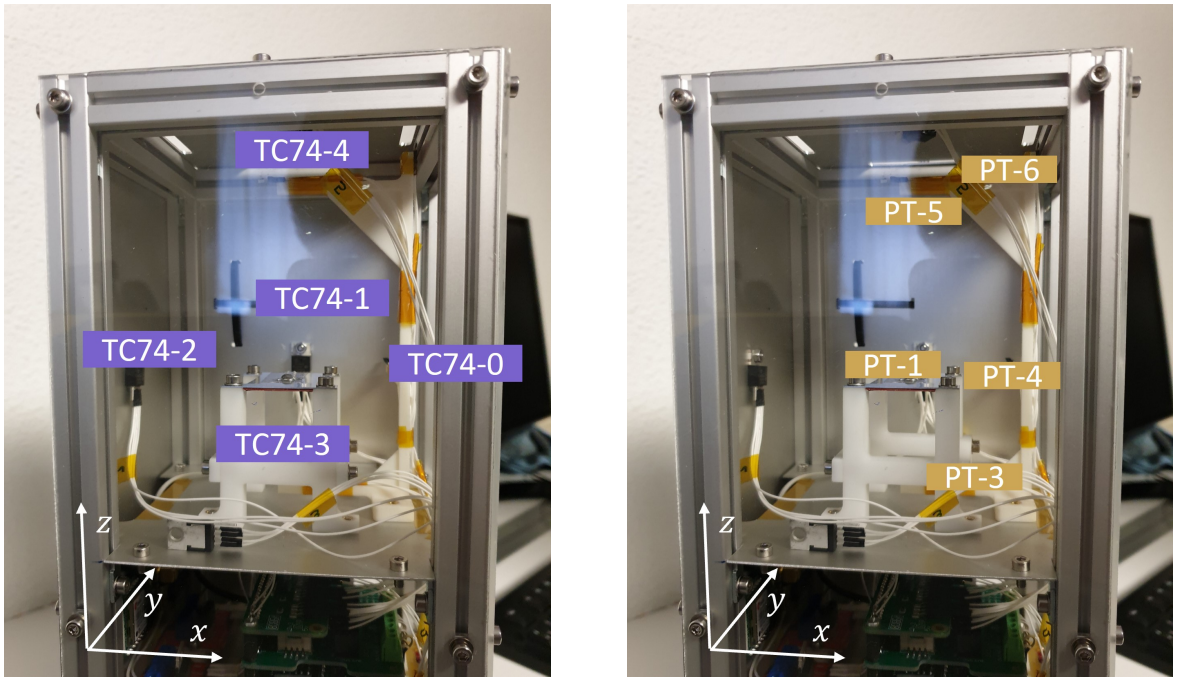

(a) (b)

Figure A.1: Temperature sensors location in HTL. (a) TC74 and (b) PT1000. Key for labels in Table A.1.

Table A.1: Location and function of the PT1000 and TC74 type sensors employed for the temperature measurements of the HTL during flight (see Figure A.1).

Sensor Type	ID	Location	Comment
PT1000	PT1	Centre of the heated plate.	Measurement of the experiment plate temperature.
	PT2	Centre of the heater.	Measurement of the experiment plate temperature at the heater face.
	PT3	30 mm underneath the heated plate.	Measurement of the air temperature at this specific location.
	PT4	On the same plane as the experiment plate and near the corner of the structure.	Measurement of the air temperature of unperturbed flow, T_{inf}.
	PT5	70 mm above the heated plate.	Measurement of the air temperature at this specific location.
	PT6	Near the slots on the satellite's closure panel.	Measurement of the air temperature at this specific location, where flow is expected to appear due to the motion of the payload during flight.
TC74	TC74-0	At the centre of the inner wallof the X+ panel[1].	[2]
	TC74-1	At the centre of the inner wallof the Y+ panel[1].	[2]
	TC74-2	At the centre of the inner wallof the X- panel[1].	[2]
	TC74-3	At the centre of the inner wallof the Y- panel[1].	[2]
	TC74-4	At the centre of the inner wallof the satellite's top closure panel.	[2]

[1] 50 mm above the HTL structural tray in cavity 3 (Figure A.1b).

[2] Measurement of the structural panel temperature (Figure A.1b).

The temperature sensors location during the vacuum test is summarized in Table A.2.

Table A.2: Location of the thermocouples during the vacuum test.

ID	Location
01	Baseplate under the experiment.
02	Heated plate.
03	Tray inner face (Z—).
04	Closure panel (X—).
05	Closure panel (Y+).
06	Closure panel (Y—).
07	Air inside the cavity (corner).
08	Closure panel (Z+).
09	Closure panel (X+).
10	Air inside the cavity (above the plate).
11	Air outside the cavity (above the upper tray).

Appendix B. Väisälä-Brunt Frequency

During the development and validation of the balloon-borne experiment ascent phase simulation tool, it has been observed an oscillatory behaviour of the vertical speed around the mean ascent rate, especially once the tropopause has been exceeded [124], in most of the real data flight analysed to validate the tool. From the outset, these oscillations could be explained by some of the following reasons:

- Once a ballast mass is dropped, the reduction on the weight provokes an increase in the buoyancy force (and in consequent in the lift force). Depending on the method to drop the ballast (depending on how the release is made, whether instantaneously or continuously, it may cause an oscillation).
- Venting the lifting gas before reaching float altitude could also cause oscillations.
- Consequence of a wind gust that leads to a sudden change in the drag coefficient (by changing from subcritical to supercritical Reynolds regime or vice-versa).
- The natural frequency of the balloon-borne system itself may be similar to the natural frequency of atmospheric waves, exciting the resonance of the system.

Some research concerning the atmospheric waves, which are identified by the Väisälä-Brunt frequency can be found in [124]–[127]. This frequency can be similar to the natural frequency of the balloon-borne system as a buoyant system leading to a resonance. Thus, in Ref. [124] an expression is proposed to compute the balloon oscillation frequency, f_b, as:

$$f_b = \frac{1}{2\pi}\sqrt{\frac{k_b}{m_t}}, \tag{B.1}$$

where m_t is the system total mass (see Equation 3.18), and k_b is the effective spring rate of the buoyancy, defined by the change in lift associated to the change in altitude (from z_1 to z_2, $\Delta z = z_2 - z_1$), which is computed using [124]:

$$k_b = -\frac{\Delta L}{\Delta z}, \tag{B.2}$$

where ΔL is the lift increment under a small perturbation of altitude [124], and approximated by:

$$\Delta L = L_{z=z_2} - L_{z=z_1} = g\left(\rho_a - \rho_g\right) V\Big|_{z=z_2} - g\left(\rho_a - \rho_g\right) V\Big|_{z=z_1}, \tag{B.3}$$

which can be rewritten (neglecting second order terms) as follows:

$$\Delta L = g\left(\rho_a - \rho_g\right)_{z=z_2} \Delta V + g\left(\Delta\rho_a - \Delta\rho_g\right) V_{z=z_2}, \tag{B.4}$$

where $\Delta\rho_a$, and $\Delta\rho_g$ are the air and lifting gas density gradient respectively.

Concerning the atmospheric waves, according to Ref. [125], the Väisälä-Brunt frequency, f_v at z_2 is given by:

$$f_v = \frac{1}{2\pi}\sqrt{\frac{-g\frac{\partial\rho_a}{\partial z}}{\rho} - \frac{-g^2\rho_a}{\gamma_a p_a}}, \tag{B.5}$$

where the $\frac{\partial\rho_a}{\partial z}$ is the gradient of air density with regard to altitude.

The expected Väisälä-Brunt atmospheric wave periods, flight observations (only four points), and expected balloon-borne system natural period, are shown in Figure B.1 [124]. It is clearly shown that both, the expected balloon natural period and the Väisälä-Brunt atmospheric wave period, are very close to each other for an altitude higher than 12 km.

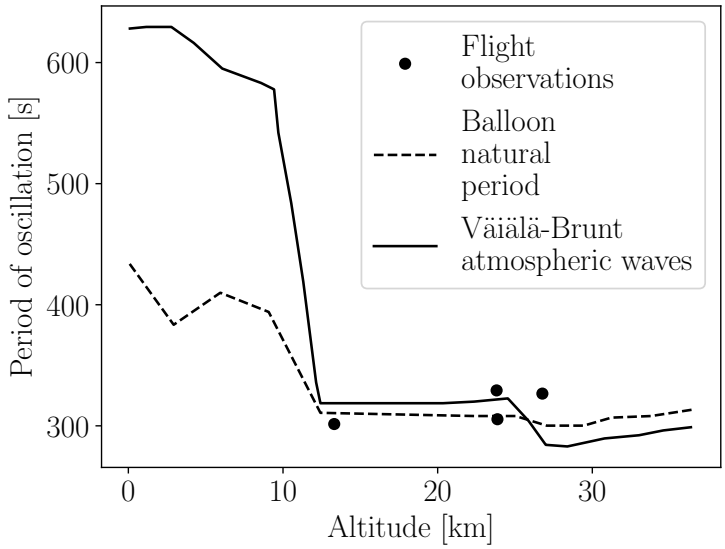

Figure B.1: Comparison of the balloon-borne system natural period, and Väisälä-Brunt atmospheric wave periods (adapted from [124]).

From the two analytical equations for both frequencies (B.4) and (B.5), two main conclusions are obtained [124]:

- The balloon natural period is independent to the balloon size, as the displaced volume is proportional to the balloon-borne system masses.
- The air pressure, and air temperature (as the air density, by the perfect gas law approach, depends only on both parameters), and density gradient determine the Väisälä-Brunt atmospheric wave frequency.

Then, two different studies are performed to check whether both frequencies are overlapped in some stages during the ascent phase. In section B.1, from the data flight of different balloon-borne missions, the period observed peak-to-peak on the ascent rate profile is analysed. In section B.2, the tool developed is used to obtain the balloon-borne system natural period using (B.1), from two different air temperature profiles, and then the same atmospheres are used to estimate the Väisälä-Brunt atmospheric wave frequency using (B.5).

B.1 Data flight analysis

GPS flight data from BEXUS 26 is analysed to obtain the dominant ascent rate oscillation period

once the tropopause has been exceeded.

The ascent rate profile available from the BEXUS 26 flight has been obtained from [22] (under request). It is shown in Figure B.2, where the profile has been divided into two stages. The sample interval is 20 s.

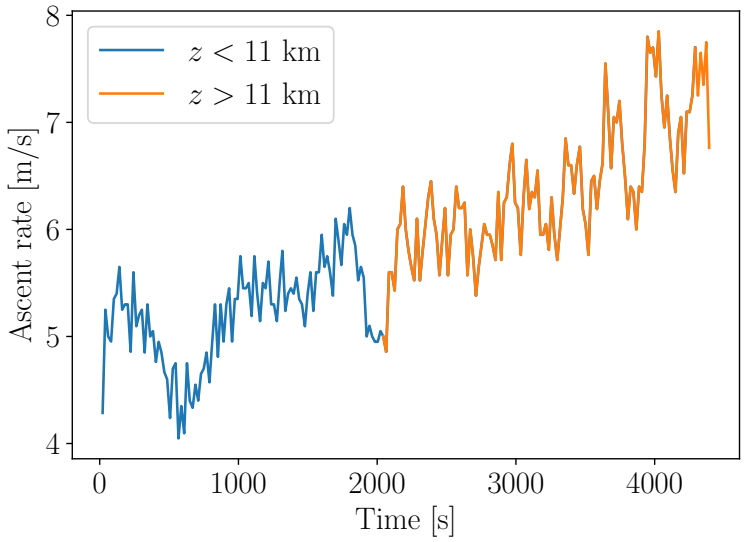

Figure B.2: BEXUS 26 flight ascent rate profile. The blue line represents the stage $z < 11$ km; the orange line stands for the stage $z > 11$ km.

To identify the spectral content, the one-dimensional discrete Fourier Transform [128], [129] is applied to the second stage ($z > 11$ km) of the ascent rate. Previously, the mean value and the linear trend of the signal are subtracted to remove the peak on the null frequency, and the frequency with the largest period. The signal spectrum is presented in Figure B.3, where it has been highlighted the frequency region corresponding to periods between 200 s and 400 s (which are the values expected for the Väisälä-Brunt atmospheric wave frequency). Although there is no only one dominant frequency, some of the strongest frequencies are found within the band, supporting the hypothesis that the balloon dynamics can be excited by the atmospheric wave.

B.2 Simulation comparison

After studying the flight data, the tool developed is used to compute the Väisälä-Brunt frequency for different air temperature profiles, and then compare the balloon-borne system natural period computed with the tool using these air temperature profiles, following (B.1) and (B.5). The en-

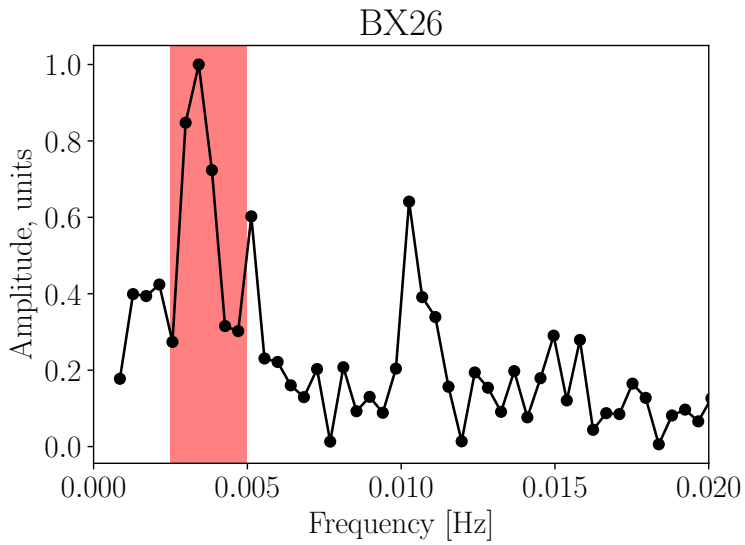

Figure B.3: BEXUS 26 flight ascent rate in the frequency domain. The highlighted region corresponds to the band defined by the periods between 200 s and 400 s.

velope obtained for both periods is shown in Figure B.4. Once the tropopause is exceeded, both periods reduce their values, and the envelopes overlapped, which confirms the assumption that the balloon dynamics can be excited by the atmospheric waves.

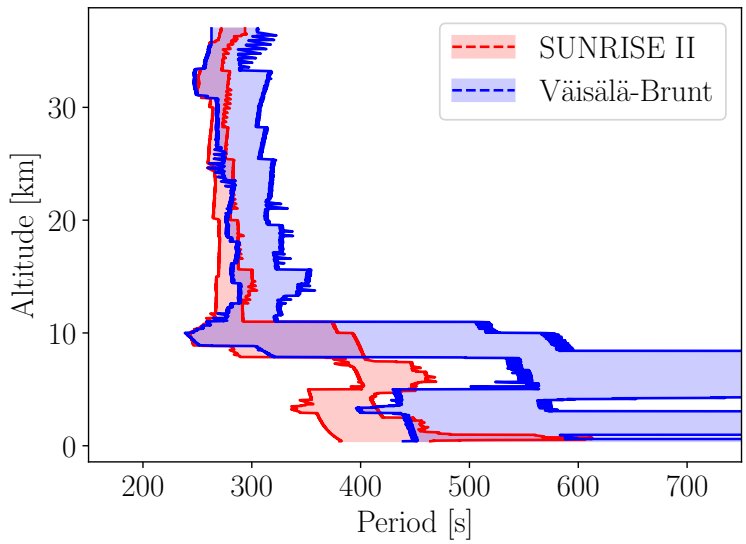

Figure B.4: Comparison of the simulated balloon-borne system natural period envelope expected during the ascent, and the simulated Väisälä-Brunt atmospheric wave periods envelope expected during the ascent.

Appendix C. Literature contributions

Concerning thermal problemas related to this Doctoral Dissertation, eight papers have been published in relevant aerospace journals:

- D. González-Bárcena, A. Fernández-Soler, I. Pérez-Grande, and Á. Sanz-Andrés, "Real data-based thermal environment definition for the ascent phase of Polar-Summer Long Duration Balloon missions from Esrange (Sweden)," *Acta Astronautica*, vol. 170, pp. 235–250, 2020.

- D. González-Bárcena, A. Fernández-Soler, A. González-Llana, J. Díez-González, R. Álvarez, I. Pérez-Grande, and Á. Sanz-Andrés, "Ascent phase thermal analysis of Long Duration Balloons," *Acta Astronautica*, vol. 195, pp. 416–429, 2022.

- D. Alfonso-Corcuera, M. Ogueta-Gutiérrez, A. Fernández-Soler, D. González-Bárcena, and S. Pindado, "Measuring Relative Wind Speeds in Stratospheric Balloons with Cup Anemometers: The TASEC-Lab Mission," *Sensors*, vol. 22, no. 15, 2022, ISSN: 1424-8220. DOI: 10.3390/s22155575.

- D. González-Bárcena, L. Peinado-Pérez, A. Fernández-Soler, Á. G. Pérez-Muñoz, J. M. Álvarez-Romero, F. Ayape, J. Martín, J. Bermejo-Ballesteros, Á. L. Porras-Hermoso, D. Alfonso-Corcuera, *et al.*, "TASEC-Lab: A COTS-based CubeSat-like university experiment for characterizing the convective heat transfer in stratospheric balloon missions," *Acta Astronautica*, vol. 196, pp. 244–258, 2022.

- A. Fernández-Soler, I. Torralbo, I. Pérez-Grande, R. T. Pardavila, and T. Anzai, "Study of pyrolitic graphite sheet potential as thermal passive element in CubeSats," *Advances in Space Research*, vol. 71, no. 11, pp. 4431–4442, 2023.

- A. Fernández-Soler, D. González-Bárcena, I. Torralbo-Gimeno, and I. Pérez-Grande, "Ascent phase convective heat transfer of a stratospheric-balloon-borne payload," *Advances in Space Research*, vol. 72, no. 2, pp. 503–517, 2023.
- D. González-Bárcena, N. Martínez-Figueira, A. Fernández-Soler, I. Torralbo, M. Bayón, J. Piqueras, and I. Pérez-Grande, "Experimental correlation of natural convection in low Rayleigh atmospheres for vertical plates and comparison between CFD and lumped parameter analysis," *International Journal of Heat and Mass Transfer*, vol. 222, p. 125 140, 2024.
- A. Fernández-Soler, D. González-Bárcena, I. Torralbo-Gimeno, and I. Pérez-Grande "Stratospheric balloon dynamics predictions for robust ascent phase payload thermal analysis." *Advances in Space Research*, **Under review 24-01-2024.**

Besides, several presentations have been performed at relevant space sector congresses as presenter:

- A. Fernández-Soler. "Long Duration Balloon ascent tool. Combination of dynamical and thermal model during the balloon ascent phase". *III Congreso de Ingeniería Espacial, El espacio, la última frontera*. 2020.
- A. Fernández-Soler, G. Fernández-Rico, A. Feller, I. Torralbo-Gimeno, and I. Perez-Gránde, "Thermal Analysis of SUSI-O on SUNRISE III," 2020 International Conference on Environmental Systems, 2020
- A. Fernández-Soler, D. González-Bárcena, I. Pérez-Grande, and Á. Sanz-Andrés, "Thermal Analysis of SUNRISE III ascent phase," 2021 International Conference on Environmental Systems, 2021
- A. Fernández-Soler, D. González-Bárcena, and I. Pérez Grande, "Characterization of the convective heat transfer in stratospheric balloon missions based on flight-data," *44th COSPAR Scientific Assembly. Held 16-24 July*, vol. 44, p. 3373, 2022
- A. Fernández-Soler, G. Morgante, A. García-Pérez, and J. Pérez-Álvarez. "Preliminar Ariel Decontamination thermal analysis". *European Space Thermal Engineering Workshop*. 2023.

And contributed to the following presentations:

- L. Peinado, F. Ayape Alonso, A. Fernández-Soler, J. Martin, D. González-Bárcena, V. Muntean, and I. Grande, "Experiments of the Prototype for a Stratospheric Balloon- borne

Heat Transfer Laboratory," 50th International Conference on Environmental Systems, 7 2021

- J. Bermejo Ballesteros, J. M. Vergara Pérez, A. Fernández Soler, and J. Cubas Cano, "Mubody, an astrodynamics open-source Python library focused on libration points," in *4th Symposium on Space Educational Activities*, Universitat Politècnica de Catalunya, 2022

REFERENCES

[1] N. Yajima, N. Izutsu, T. Imamura, and T. Abe, "Scientific Ballooning: Technology and Applications of Exploration Balloons Floating in the Stratosphere and the Atmospheres of Other Planets," Jan. 2009.

[2] Gillispie, Charles Coulston, *The Montgolfier brothers and the invention of aviation 1783-1784: with a word on the importance of ballooning for the science of heat and the art of building railroads*. Princeton University Press, 2014, vol. 684.

[3] E. Frankel, "JB Biot and the mathematization of experimental physics in Napoleonic France," *Historical studies in the physical sciences*, vol. 8, pp. 33–72, 1977.

[4] J. L. Du Bois, R. P. Multhauf, R. P. Multhauf, and C. A. Ziegler, *The invention and development of the radiosonde: Smithsonian studies in history and technology*, 2002.

[5] M. Walter and A. W. Wolfendale, "Early history of cosmic particle physics," *The European Physical Journal H*, vol. 37, no. 3, pp. 323–358, 2012.

[6] R. E. Danielson, "Project STRATOSCOPE," *American Scientist*, vol. 49, no. 3, pp. 370–398, 1961, ISSN: 00030996. [Online]. Available: http://www.jstor.org/stable/27827856 (visited on 08/28/2023).

[7] R. E. Danielson, "The first flight STRATOSCOPE II," *American Scientist*, vol. 51, no. 4, pp. 375–399, 1963, ISSN: 00030996. [Online]. Available: http://www.jstor.org/stable/27838842 (visited on 08/28/2023).

[8] H. P. Stahl, "50 Years to NASA Mirror Technology Development: From Hubble to JWST and Beyond," in *6th Internaional Symposium on Advanced Optical Manufacturing and Testing Technologies (AOMATT 2012)*, 2012.

[9] B. M. Malaya Kumar and R. N. Annavarapu, "Conceptual Design of Mars Sample Return Mission Using Solar Montgolfieres," in *2021 IEEE Aerospace Conference (50100)*, 2021, pp. 1–10. DOI: 10.1109/AERO50100.2021.9438529.

[10] L. E. Pacheco, *Stratospheric Balloons: Chronological lists of launches worldwide since 1947*, http://stratocat.com.ar/globos/indexe.html, Oct. 2018.

[11] Morris, Alvin L, *Scientific ballooning handbook*. Atmospheric Technology Division, National Center for Atmospheric Research, 1975.

[12] I. Pérez-Grande, A. Sanz-Andrés, N. Bezdenejnykh, and P. Barthol, "Transient thermal analysis during the ascent phase of a balloon-borne payload. Comparison with SUNRISE test flight measurements," *Applied Thermal Engineering*, vol. 29, no. 8-9, pp. 1507–1513, 2009.

[13] A. González-Llana, D. González-Bárcena, I. Pérez-Grande, and Á. Sanz-Andrés, "Selection of extreme environmental conditions, albedo coefficient and Earth infrared radiation, for polar summer Long Duration Balloon missions," *Acta Astronautica*, vol. 148, pp. 276–284, 2018.

[14] A. Porras-Hermoso, D. Alfonso-Corcuera, J. Piqueras, E. Roibás-Millán, J. Cubas, J. Pérez-Álvarez, and S. Pindado, "Design, ground testing and on-orbit performance of a Sun sensor based on COTS photodiodes for the UPMSat-2 satellite," *Sensors*, vol. 21, no. 14, p. 4905, 2021.

[15] D. González-Bárcena, A. Fernández-Soler, I. Pérez-Grande, and Á. Sanz-Andrés, "Real data-based thermal environment definition for the ascent phase of Polar-Summer Long Duration Balloon missions from Esrange (Sweden)," *Acta Astronautica*, vol. 170, pp. 235–250, 2020.

[16] D. González-Bárcena, A. Fernández-Soler, A. González-Llana, J. Díez-González, R. Álvarez, I. Pérez-Grande, and Á. Sanz-Andrés, "Ascent phase thermal analysis of Long Duration Balloons," *Acta Astronautica*, vol. 195, pp. 416–429, 2022.

[17] P. P. Almazan, "Accuracy control in Monte Carlo radiative calculations," in *NASA. Lewis Research Center, The Fifth Annual Thermal and Fluids Analysis Workshop*, 1993.

[18] J. Meseguer, I. Pérez-Grande, and A. Sanz-Andrés, *Spacecraft thermal control*. Elsevier, 2012.

[19] P. Barthol, A. Gandorfer, S. K. Solanki, M. Schüssler, B. Chares, W. Curdt, W. Deutsch, A. Feller, D. Germerott, B. Grauf, *et al.*, "The Sunrise Mission," *Solar Physics*, vol. 268, no. 1, pp. 1–34, 2011.

[20] S. Solanki, T. Riethmüller, P. Barthol, S. Danilovic, W. Deutsch, H.-P. Doerr, A. Feller, A. Gandorfer, D. Germerott, L. Gizon, *et al.*, "The second flight of the SUNRISE balloon-borne solar observatory: overview of instrument updates, the flight, the data, and first results," *The Astrophysical Journal Supplement Series*, vol. 229, no. 1, p. 2, 2017.

[21] HERCCULES, *HERCCULES*, https://blogs.upm.es/herccules/, Acceded 07-11-2023.

[22] *REXUS/BEXUS programme*, https://rexusbexus.net/, Jul. 2022.

[23] J. Adkins, *Types of balloons*, https://www.nasa.gov/scientific-balloons/types-of-balloons, Jul. 2015.

[24] J. Adkins, *Scientific balloons*, https://www.nasa.gov/scientificballoons, Jul. 2015.

[25] P. Baldemar, "Long Duration Balloon Flights from Esrange," in *AIAA 5th ATIO and16th Lighter-Than-Air Sys Tech. and Balloon Systems Conferences*. DOI: 10.2514/6.2005-7365.

[26] *Swedish Space Corporation, Stratospheric Balloon Launch*, https://sscspace.com/services/science-and-launch-services/stratospheric-balloons/.

[27] I. Smith Jr, "The NASA balloon program: an overview," *Advances in Space Research*, vol. 30, no. 5, pp. 1087–1094, 2002.

[28] W. V. Jones, "The US long duration balloon facility at McMurdo Station," *Proceedings of the International Astronomical Union*, vol. 8, no. S288, pp. 169–177, 2012.

[29] J. Pommereau, L. Denis, and F. Goutail, "Study of the Arctic Vortex Using Long Duration Balloons," in *European Rocket and Balloon Programmes and Related Research, Proceedings of the 13th ESA Symposium held 26-29 May, 1997 in Öland, Sweden. Edited by Brigitte Kaldeich-Schürmann. ESA SP-397. Paris: European Space Agency, 1997., p. 197*, vol. 397, 1997, p. 197.

[30] Y. Cengel, *Heat and mass transfer: fundamentals and applications*. McGraw-Hill Higher Education, 2014.

[31] F. P. Incropera, D. P. DeWitt, T. L. Bergman, and A. S. Lavine, "Fundamentals of heat and mass transfer, John Wiley & Sons," *Inc., Hoboken, NJ., 981p*, 2002.

[32] J. P. Holman, *Heat transfer*. McGraw-Hill, 1989.

[33] I. Martínez, http://webserver.dmt.upm.es/~isidoro/, Acceded 02-05-2019.

[34] P. Fortescue, G. Swinerd, and J. Stark, *Spacecraft systems engineering*. John Wiley & Sons, 2011.

[35] Secretariat, ECSS, "ECSS thermal analysis handbook," Technical Report ECSS-E-HB-31-03A15, ESA, Tech. Rep., 2015.

[36] D. G. Gilmore and M. Bello, *Satellite thermal control handbook*. Aerospace Corporation Press EI Segundo, CA, 1994, vol. 1.

[37] Secretariat, ECSS, "ECSS space engineering-space environment," Technical Report ECSS-E-ST-10-04C, ESA, Tech. Rep., 2008.

[38] I. E. U. Ltd., *ESATAN-TMS Thermal Engineering Manual*, 2015.

[39] T. L. Bergman, T. L. Bergman, F. P. Incropera, D. P. Dewitt, and A. S. Lavine, *Fundamentals of heat and mass transfer*. John Wiley & Sons, 2011.

[40] J. Boussinesq, *Theorie Analytique de la Chaleur*. Gauthier-Villars, 1903, vol. 2.

[41] G. S. Springer, "Heat transfer in rarefied gases," in *Advances in heat transfer*, vol. 7, Elsevier, 1971, pp. 163–218.

[42] P. A. Chambre and S. A. Schaaf, *Flow of rarefied gases*. Princeton University Press, 2017, vol. 4971.

[43] G. F. Hewitt and J. Barbosa, *Heat exchanger design handbook*. Begell house New York, 2008, vol. 98.

[44] Cavcar, Mustafa, "The international standard atmosphere (ISA)," *Anadolu University, Turkey*, vol. 30, no. 9, 1–6, 2000.

[45] T. R. A. Society, *Properties of a standard atmosphere ESDU 7702*, 2004.

[46] G. Bird, "Definition of mean free path for real gases," *The Physics of fluids*, vol. 26, no. 11, pp. 3222–3223, 1983.

[47] H.-S. Tsien, "Superaerodynamics, mechanics of rarefied gases," *Journal of the Aeronautical Sciences*, vol. 13, no. 12, pp. 653–664, 1946.

[48] A.-J. N. Khalifa, "Natural convective heat transfer coefficient – a review: I. Isolated vertical and horizontal surfaces," *Energy Conversion and Management*, vol. 42, no. 4, pp. 491–504, 2001, ISSN: 0196-8904. DOI: https://doi.org/10.1016/S0196-8904(00)00042-X. [Online]. Available: https://www.sciencedirect.com/science/article/pii/S019689040000042X.

[49] F. J. Suriano and Y. Kwang-Tzu, "Laminar free convection about vertical and horizontal plates at small and moderate Grashof numbers," *International Journal of Heat and Mass Transfer*, vol. 11, no. 3, pp. 473–490, 1968.

[50] V. Buznik and K. Bezlomtsev, "A generalized equation for the heat exchange of natural and forced convection during external flow about bodies," *Izv. Uyssh. Ucheb. Zaved.*, vol. 2, pp. 68–74, 1960.

[51] R. J. Goldstein and K.-S. Lau, "Laminar natural convection from a horizontal plate and the influence of plate-edge extensions," *Journal of Fluid Mechanics*, vol. 129, pp. 55–75, 1983. DOI: 10.1017/S0022112083000646.

[52] M. Miyamoto, Y. Katoh, J. Kurima, S. Kurihara, and K. Yamashita, "Free convection heat transfer from vertical and horizontal short plates," *International journal of heat and mass transfer*, vol. 28, no. 9, pp. 1733–1745, 1985.

[53] B. Chambers and T.-Y. T. Lee, "A Numerical Study of Local and Average Natural Convection Nusselt Numbers for Simultaneous Convection Above and Below a Uniformly Heated Horizontal Thin Plate," *Journal of Heat Transfer*, vol. 119, no. 1, pp. 102–108, Feb. 1997, ISSN: 0022-1481. DOI: 10.1115/1.2824074. eprint: https://asmedigitalcollection.asme.org/heattransfer/article-pdf/119/1/102/5507576/102_1.pdf.

[54] W. Liu, J. Wang, Y. Li, Z. Zhu, D. Qie, and L. Ding, "Natural convection heat transfer at reduced pressures," *Experimental Heat Transfer*, vol. 32, no. 1, pp. 14–24, 2019.

[55] J. Lloyd and W. Moran, "Natural convection adjacent to horizontal surface of various planforms," 1974.

[56] L. Peinado, F. Ayape Alonso, A. Fernández-Soler, J. Martin, D. González-Bárcena, V. Muntean, and I. Grande, "Experiments of the Prototype for a Stratospheric Balloon- borne Heat Transfer Laboratory," 50th International Conference on Environmental Systems, 7 2021.

[57] RS Pro, *3M Aluminum tape 425*, https://docs.rs-online.com/53eb/0900766b8108af44.pdf, Acceded 07-06-2022, 2022.

[58] HUB Digital de Innovación, *Cámara de vacío térmica TVAC archivos - HUB Digital de Innovación*, https://www.upm.es/recursosidi/infraestructura/camara-de-vacio-termica-tvac/, Acceded 21-11-2023, HUB Digital de Innovación.

[59] R. Siegel, *Thermal radiation heat transfer*. CRC press, 2001.

[60] T. G. Beckwith, N. L. Buck, and R. D. Marangoni, *Mechanical measurements*. Addison-Wesley Reading, MA, 1969, vol. 5.

[61] L. Peinado, V. Muntean, and I. Pérez-Grande, "A free convection heat transfer correlation for very thin horizontal wires in rarefied atmospheres," *Experimental Thermal and Fluid Science*, vol. 122, p. 110 295, 2021, ISSN: 0894-1777. DOI: https://doi.org/10.1016/j.expthermflusci.2020.110295.

[62] N. Yajima, N. Izutsu, T. Imamura, and T. Abe, *Scientific ballooning: Technology and applications of exploration balloons floating in the stratosphere and the atmospheres of other planets*. Springer New York, 2009, pp. 1–213, ISBN: 9780387097251. DOI: 10.1007/978-0-387-09727-5.

[63] D. González-Bárcena, L. Peinado-Pérez, A. Fernández-Soler, Á. G. Pérez-Muñoz, J. M. Álvarez-Romero, F. Ayape, J. Martín, J. Bermejo-Ballesteros, Á. L. Porras-Hermoso, D. Alfonso-Corcuera, *et al.*, "TASEC-Lab: A COTS-based CubeSat-like university experiment for characterizing the convective heat transfer in stratospheric balloon missions," *Acta Astronautica*, vol. 196, pp. 244–258, 2022.

[64] C. B. Kjellstrand, G. Jones, C. Geach, B. P. Williams, D. C. Fritts, A. Miller, S. Hanany, M. Limon, and J. Reimuller, "The PMC Turbo balloon mission to measure gravity waves and turbulence in Polar Mesospheric Clouds: Camera, telemetry, and software performance," *Earth and Space Science*, vol. 7, no. 8, e2020EA001238, 2020.

[65] Q. Wu, D. Knipp, J. Liu, W. Wang, I. Häggström, G. Jee, Y.-S. Kwak, and P. J. Erickson, "What Do the New 2018 HIWIND Thermospheric Wind Observations Tell Us About High-Latitude Ion-Neutral Coupling During Daytime?" *Journal of Geophysical Research: Space Physics*, vol. 124, no. 7, pp. 6173–6181, 2019.

[66] A. González-Llana, D. González-Bárcena, I. Pérez-Grande, and Á. Sanz-Andrés, "Selection of extreme environmental conditions, albedo coefficient and Earth infrared radiation, for polar summer Long Duration Balloon missions," *Acta Astronautica*, vol. 148, pp. 276–284, 2018, ISSN: 0094-5765. DOI: https://doi.org/10.1016/j.actaastro.2018.05.016. [Online]. Available: https://www.sciencedirect.com/science/article/pii/S0094576518304132.

[67] D. González-Bárcena, A. Fernández-Soler, I. Pérez-Grande, and Á. Sanz-Andrés, "Real data-based thermal environment definition for the ascent phase of Polar-Summer Long Duration Balloon missions from Esrange (Sweden)," *Acta Astronautica*, vol. 170, pp. 235–250, 2020, ISSN: 0094-5765. DOI: https://doi.org/10.1016/j.actaastro.2020.01.024.

[68] R. Farley, "BalloonAscent: 3-D simulation tool for the ascent and float of high-altitude balloons," in *AIAA 5th ATIO and 16th Lighter-Than-Air Sys Tech. and Balloon Systems Conferences*, 2005, p. 7412.

[69] R. Palumbo, M. Russo, E. Filippone, F. Corraro, and S. Cira, "Achab: Analysis code for high-altitude balloons," 2007, ISSN: 2007-6642.

[70] P. Tans and R. Keeling, "NOAA," *ESRL (www. esrl. noaa. gov/gmd/ccgg/trends/)*, 2010.

[71] H. Hersbach, "The ERA5 Atmospheric Reanalysis.," in *AGU fall meeting abstracts*, vol. 2016, 2016, NG33D–01.

[72] S. G. Ungar, J. S. Pearlman, J. A. Mendenhall, and D. Reuter, "Overview of the earth observing one (EO-1) mission," *IEEE Transactions on Geoscience and Remote Sensing*, vol. 41, no. 6, pp. 1149–1159, 2003.

[73] M. D. King, "Overview of Terra," in *Remote Sensing of the Earth"s Environment from Terra*, 2002.

[74] C. L. Parkinson, "Aqua: An Earth-observing satellite mission to examine water and other climate variables," *IEEE Transactions on Geoscience and Remote Sensing*, vol. 41, no. 2, pp. 173–183, 2003.

[75] J. Cooper, "Clouds and the earths radiant energy system (CERES): an Earth observing system experiment," *Bull Am Meteorol Soc*, vol. 77, no. 5, 853868Ziebart, 1996.

[76] R. C. Scott, F. G. Rose, P. W. Stackhouse Jr, N. G. Loeb, S. Kato, D. R. Doelling, D. A. Rutan, P. C. Taylor, and W. L. Smith Jr, "Clouds and the Earth's Radiant Energy System (CERES) Cloud Radiative Swath (CRS) Edition 4 Data Product," *Journal of Atmospheric and Oceanic Technology*, vol. 39, no. 11, pp. 1781–1797, 2022.

[77] D. R. Doelling, M. Sun, L. T. Nguyen, M. L. Nordeen, C. O. Haney, D. F. Keyes, and P. E. Mlynczak, "Advances in geostationary-derived longwave fluxes for the CERES synoptic (SYN1deg) product," *Journal of Atmospheric and Oceanic Technology*, vol. 33, no. 3, pp. 503–521, 2016.

[78] Unidata, *Unidata | netcdf*, https://www.unidata.ucar.edu/software/netcdf/, [Accessed 30-01-2024].

[79] NASA, *CERES SYN1degEd4.1 Subsetting and Browsing — ceres-tool.larc.nasa.gov*, https://ceres-tool.larc.nasa.gov/ord-tool/jsp/SYN1degEd41Selection.jsp, [Accessed 21-01-2022].

[80] ECMWF, *ECMWF — ecmwf.int*, https://www.ecmwf.int, [Accessed 21-01-2022].

[81] ECMWF, *About Copernicus | Copernicus — copernicus.eu*, https://www.copernicus.eu/en/about-copernicus, [Accessed 21-01-2022].

[82] *Copernicus Climate Data Store | Copernicus Climate Data Store — cds.climate.copernicus.eu*, https://cds.climate.copernicus.eu/cdsapp#!/dataset/10.24381/cds.bd0915c6?tab=overview, [Accessed 21-01-2022].

[83] *Access ECMWF Public Datasets - ECMWF Web API - ECMWF Confluence Wiki — confluence.ecmwf.int*, https://confluence.ecmwf.int/display/WEBAPI/Access+ECMWF+Public+Datasets, [Accessed 21-01-2022].

[84] ECMWF, *MARS content - User Documentation - ECMWF Confluence Wiki*, https://confluence.ecmwf.int/display/UDOC/MARS+content, [Accessed 21-01-2022].

[85] ECMWF, *MARS example requests - User Documentation - ECMWF Confluence Wiki*, https://confluence.ecmwf.int/display/UDOC/MARS+example+requests, [Accessed 21-01-2022].

[86] World Meteorological Organization (WMO), *WWW Technical report No. 17 WMO/TD-No. 611*, http://www.wmo.int/pages/prog/www/WMOCodes/Guides//GRIB/GRIB1-Contents.html, 1994.

[87] N. G. Loeb, S. Kato, K. Loukachine, and N. Manalo-Smith, "Angular distribution models for top-of-atmosphere radiative flux estimation from the Clouds and the Earth's Radiant Energy System instrument on the Terra satellite. Part I: Methodology," *Journal of Atmospheric and Oceanic Technology*, vol. 22, no. 4, pp. 338–351, 2005.

[88] ECMWF, "IFS Documentation CY41R2 - Part III: Dynamics and Numerical Procedures," eng, in 3. ECMWF, 2016. DOI: {10.21957/83wouv80}.

[89] Koeck, C., Coffinier, P., Auberger, X., and Rebis, J.-J., "Kernel Algorithms document - ESARAD," ESA ESTEC; MATRA/ERC, Tech. Rep., 1994.

[90] Anderson, BJ and Justus, CG and Batts, GW, "Guidelines for the selection of near-earth thermal environment parameters for spacecraft design," No. NASA/TM-2001-211221, Tech. Rep., 2001.

[91] M. L. Waskom, "Seaborn: statistical data visualization," *Journal of Open Source Software*, vol. 6, no. 60, p. 3021, 2021.

[92] Kreider, JF and Kreith, F, "Numerical prediction of high altitude zero-pressure balloon vertical motion," 1975.

[93] L. A. Carlson and W. J. Horn, "New thermal and trajectory model for high-altitude balloons," *Journal of Aircraft*, vol. 20, pp. 500–507, 6 1983, ISSN: 00218669. DOI: 10.2514/3.44900.

[94] S. Runnels, M. Smith, and D. Fairbrother, "High-altitude balloon thermal trajectory analysis database system," in *AIAA's 3rd Annual Aviation Technology, Integration, and Operations (ATIO) Forum*, 2003, p. 6821.

[95] A. Pankine, R. S. Schlaifer, and M. Heun, "Advanced balloon performance simulation and analysis tool," in *AIAA's 3rd Annual Aviation Technology, Integration, and Operations (ATIO) Forum*, 2003, p. 6741.

[96] I. Musso, A. Cardillo, O. Cosentino, and A. Memmo, "A balloon trajectory prediction system," *Advances in Space Research*, vol. 33, pp. 1722–1726, 10 2004, ISSN: 02731177. DOI: 10.1016/j.asr.2003.07.044.

[97] Q. Liu, M. Zhu, W. Xu, and L. Liang, "Advanced thermaldynamic model of a stratospheric balloon with impact of wind shear," 2012, ISBN: 9781624101830. DOI: 10.2514/6.2012-5054.

[98] G. Morani, R. Palumbo, G. Cuciniello, F. Corraro, and M. Russo, "Method for prediction and optimization of a stratospheric balloon ascent trajectory," vol. 46, American Institute of Aeronautics and Astronautics Inc., 2009, pp. 126–133. DOI: 10.2514/1.39469.

[99] R. Palumbo, G. Morani, and F. Corraro, "Effective approach to characterization of prediction errors for balloon ascent trajectories," *Journal of Aircraft*, vol. 47, pp. 1331–1337, 4 2010, ISSN: 15333868. DOI: 10.2514/1.47005.

[100] A. Sobester, H. Czerski, N. Zapponi, and I. Castro, "High-altitude gas balloon trajectory prediction: A Monte Carlo model," *AIAA Journal*, vol. 52, 832–842, 4 2014, ISSN: 00011452. DOI: {10.2514/1.J052900}.

[101] Y. Zhang and D. Liu, "Influences of initial launch conditions on flight performance of high altitude balloon ascending process," *Advances in Space Research*, vol. 56, pp. 605–618, 4 Aug. 2015, ISSN: 18791948. DOI: 10.1016/j.asr.2015.04.031.

[102] Sherif Saleh and Weiliang He, "Ascending performance analysis for high altitude zero pressure balloon," *Advances in Space Research*, vol. 59, pp. 2158–2172, 8 Apr. 2017, ISSN: 18791948. DOI: 10.1016/j.asr.2017.01.040.

[103] Y. Lee and K. Yee, "Numerical prediction of scientific balloon trajectories while considering various uncertainties," *Journal of Aircraft*, vol. 54, pp. 768–782, 2 2017, ISSN: 15333868. DOI: 10.2514/1.C033998.

[104] George Conrad and Edward Robbins, "Determination of balloon drag," American Institute of Aeronautics and Astronautics (AIAA), Oct. 1991. DOI: 10.2514/6.1991-3666.

[105] W. Press, B. Flannery, S. Teukolsky, and W. Vetterling, "Runge-Kutta method," *Numerical recipes in Fortran: The art of scientific computing*, pp. 704–716, 1992.

[106] I. Torralbo, I. Perez-Grande, A. Sanz-Andres, and J. Piqueras, "Correlation of spacecraft thermal mathematical models to reference data," *Acta Astronautica*, vol. 144, pp. 305–319, 2018.

[107] D. Alfonso-Corcuera, M. Ogueta-Gutiérrez, A. Fernández-Soler, D. González-Bárcena, and S. Pindado, "Measuring Relative Wind Speeds in Stratospheric Balloons with Cup Anemometers: The TASEC-Lab Mission," *Sensors*, vol. 22, no. 15, 2022, ISSN: 1424-8220. DOI: 10.3390/s22155575.

[108] P. J. Puig-Suari, *The CubeSat Program*, http://www.cubesat.org/about, Acceded 14-04-2019, 2019.

[109] S. Marín-Coca, D. González-Bárcena, E. Roibás-Millán, and S. Pindado, "On the modeling and simulation of a stratospheric experiment power subsystem," *Acta Astronautica*, vol. 198, pp. 421–430, 2022.

[110] S. Marín-Coca, D. González-Bárcena, S. Pindado, and E. Roibás-Millán, "Design and first simulations of the TASEC-Lab power subsystem," in *Journal of Physics: Conference Series*, IOP Publishing, vol. 2090, 2021, p. 012 111.

[111] R. Pro, *RS PRO Silicone Heater Mat, 1.25 W, 25 x 50mm, 12 V dc*, https://docs.rs-online.com/a2e1/0900766b8157efbb.pdf, Acceded 02-05-2019, 2019.

[112] Microchip Technology Inc., *TC74. Tiny Serial Digital Thermal Sensor datasheet*, https://pdf1.alldatasheet.com/datasheet-pdf/download/75085/MICROCHIP/TC74.html, Acceded 07-11-2023.

[113] Sensor Solutions, *PT Temperature sensor – PTF family datasheet*, https://docs.rs-online.com/9215/0900766b81554042.pdf, Acceded 07-11-2023.

[114] B2Space, *Fly your CubeSat International University Programme*, https://b2-space.com/blue-jay-programme/, 2016.

[115] J. Loughhead, G. Miles, and J. Turner, "The ESATAN Thermal Network Analysis Computer Program," SAE Technical Paper, Tech. Rep., 1984.

[116] Max Planck Institute for Solar System Research, *Sunrise Gallery*, https://www.mps.mpg.de/solar-physics/sunrise-gallery, Acceded 07-11-2023.

[117] A. Fernández-Soler, G. Fernández-Rico, A. Feller, I. Torralbo-Gimeno, and I. Perez-Gránde, "Thermal Analysis of SUSI-O on SUNRISE III," 2020 International Conference on Environmental Systems, 2020.

[118] *Integrated Forecasting System — ecmwf.int*, https://www.ecmwf.int/en/forecasts/documentation-and-support/changes-ecmwf-model, [Accessed 21-01-2022], European Centre for Medium-Range Weather Forecasts.

[119] C. Engineering., *Case studies - ecosat.* https://capgemini-engineering.com/es/en/case_study/ecosat/, Acceded 21-11-2023.

[120] SCEYE, *SCEYE. Stratospheric platforms to improve life on our planet.* https://www.sceye.com/, Acceded 21-11-2023.

[121] A. Boscaleri, F. Castagnoli, P. Rissone, and M. Corti, "Stratobus: a multiuser platform system for making access to LDB flight easier and cheaper," *European Space Agency,(Special Publication) ESA SP*, vol. 671, pp. 209–213, 2008.

[122] J. Gonzalo, D. López, D. Domínguez, A. García, and A. Escapa, "On the capabilities and limitations of high altitude pseudo-satellites," *Progress in Aerospace Sciences*, vol. 98, pp. 37–56, 2018, ISSN: 0376-0421. DOI: https://doi.org/10.1016/j.paerosci.2018.03.006. [Online]. Available: https://www.sciencedirect.com/science/article/pii/S0376042117301926.

[123] A. Fernández-Soler, D. González-Bárcena, I. Torralbo-Gimeno, and I. Pérez-Grande, "Ascent phase convective heat transfer of a stratospheric-balloon-borne payload," *Advances in Space Research*, vol. 72, no. 2, pp. 503–517, 2023.

[124] W. J. Anderson and I. Taback, "Oscillation of high-altitude balloons," *Journal of Aircraft*, vol. 28, no. 9, pp. 606–608, 1991.

[125] J. Lighthill, *Waves in fluids*. Cambridge university press, 2001.

[126] T. Tsuda, T. E. VanZandt, M. Mizumoto, S. Kato, and S. Fukao, "Spectral analysis of temperature and Brunt-Väisälä frequency fluctuations observed by radiosondes," *Journal of Geophysical Research: Atmospheres*, vol. 96, no. D9, pp. 17 265–17 278, 1991.

[127] Durran, Dale R and Klemp, Joseph B, "On the effects of moisture on the Brunt-Väisälä frequency," *Journal of Atmospheric Sciences*, vol. 39, no. 10, pp. 2152–2158, 1982.

[128] S. Winograd, "On computing the discrete Fourier transform," *Mathematics of computation*, vol. 32, no. 141, pp. 175–199, 1978.

[129] J. W. Cooley and J. W. Tukey, "An algorithm for the machine calculation of complex Fourier series," *Mathematics of computation*, vol. 19, no. 90, pp. 297–301, 1965.

[130] A. Fernández-Soler, I. Torralbo, I. Pérez-Grande, R. T. Pardavila, and T. Anzai, "Study of pyrolitic graphite sheet potential as thermal passive element in CubeSats," *Advances in Space Research*, vol. 71, no. 11, pp. 4431–4442, 2023.

[131] D. González-Bárcena, N. Martínez-Figueira, A. Fernández-Soler, I. Torralbo, M. Bayón, J. Piqueras, and I. Pérez-Grande, "Experimental correlation of natural convection in low Rayleigh atmospheres for vertical plates and comparison between CFD and lumped parameter analysis," *International Journal of Heat and Mass Transfer*, vol. 222, p. 125 140, 2024.

[132] A. Fernández-Soler, D. González-Bárcena, I. Pérez-Grande, and Á. Sanz-Andrés, "Thermal Analysis of SUNRISE III ascent phase," 2021 International Conference on Environmental Systems, 2021.

[133] A. Fernández-Soler, D. González-Bárcena, and I. Pérez Grande, "Characterization of the convective heat transfer in stratospheric balloon missions based on flight-data," *44th COSPAR Scientific Assembly. Held 16-24 July*, vol. 44, p. 3373, 2022.

[134] J. Bermejo Ballesteros, J. M. Vergara Pérez, A. Fernández Soler, and J. Cubas Cano, "Mubody, an astrodynamics open-source Python library focused on libration points," in *4th Symposium on Space Educational Activities*, Universitat Politècnica de Catalunya, 2022.